Low Altitude Unmanned Aerial Vehicles in Wireless Networks

Nilupuli Senadhira

November, 2024

A thesis submitted for the degree of Doctor of Philosophy
of The Australian National University

School of Engineering
College of Engineering, Computing and, Cybernetics
The Australian National University

Declaration

The contents of this thesis are the results of original research and have not been submitted for a higher degree to any other university or institution.

The work in this thesis has been published or has been submitted for publication as journal papers or conference proceedings.

The research work presented in this thesis has been performed jointly with Prof. Salman Durrani (The Australian National University), Assoc. Prof. Nan Yang (The Australian National University), Assoc. Prof. Xiangyun Zhou, Dr. Ming Ding (Data61, CSIRO, Australia), Dr. Sheeraz A. Alvi (The Australian National University), and Assoc. Prof. Jing Guo (Beijing Institute of Technology, China). The substantial majority of this work was my own.

Nilupuli Senadhira
School of Engineering,
The Australian National University,
Canberra, ACT 2601,
AUSTRALIA

Acknowledgements

Many of my colleagues, friends and family have their quality, sacrifices and kindness reflected in this work.

Among them is my supervisor Prof Salman Durrani. His support, advice and nurturing were key to my entire PhD. It extends well beyond the work itself and he continues to provide an excellent role model in all aspects of professional and academic life. He provided sound, empathetic advice that helped me overcome the challenges along the way.

An extension of my supervisory team were my associate supervisors Assoc. Prof. Nan Yang and Assoc. Prof. Xiangyun Zhou who provided me with invaluable suggestions to improve my academic skills. They have also both been excellent people and professionals.

I would like to extend many thanks to my collaborators Dr. Sheeraz Alvi, Dr. Ming Ding, and Assoc. Prof. Jing Guo, it was a pleasure working with you and I am happy we made some inroads into our goals.

The wider university community also deserves thanks, and there are so many to list. People who I shared office spaces with before COVID, to the administration and leadership of the university who have accommodated me well and made me feel safe. There are truly so many people on campus over the last couple of years who have gone on this journey with me.

I thank my parents Susila and Neil, and sister Amanda. They emigrated to Australia with me to start at ANU during my undergraduate studies, have never wavered in their love and support. One of the biggest achievements of my collective studies is that we have been able to do it together. My parents and sister may not have made scientific contributions, but they kept me fed, safe, loved and did the little things. They have often forgone their own goals and needs for mine and I am

eternally grateful.

The rest of my family, both my own, my husband Andrew and his family, have re-enforced all of that. I am blessed to have so many supports and as I come to the end of this endeavour I recognise that nothing is done in isolation or without sacrifice. From the start of this PhD I have lived with my partner, and for much of it with my two puppy dogs Beemo and Button. All of my family mean so much to me and the opportunity to put forward this thesis and thank them means so much to me as well.

Abstract

In the realm of 5G wireless communications, UAVs present an intriguing prospect owing to their inherent attributes, such as mobility, flexible deployment, autonomy, line-of-sight establishment, and adjustable altitude. The rapid evolution of 5G and beyond 5G networks, alongside advancements in miniaturization, control, computerization, and cost reduction in UAV manufacturing, has propelled UAVs into pivotal roles across industrial, commercial, and civilian domains. Within this context, this thesis focuses on three distinct UAV applications: firstly, the utilization of cellular-connected UAVs as aerial users; secondly, the deployment of a UAV as an aggregator to increase communication range and increase reliability of a Internet of Things networks with high reliability and low latency requirements; and thirdly, their integration into maritime-satellite networks to enable communication between maritime users and satellites, in the absence of onshore base stations.

First, we explore a novel cellular-connected UAV architecture tailored for surveillance or monitoring applications. We investigate a specific scenario wherein a cellular-connected aerial user equipment (AUE) periodically transmits data in the uplink, adhering to a predetermined data rate requirement while traversing a predefined trajectory. For efficient spectrum utilization, we introduce power-domain aerial-terrestrial non-orthogonal multiple access (NOMA), allowing simultaneous uplink transmission of both the AUE and a terrestrial user equipment (TUE) while considering the AUE's known trajectory. To evaluate system performance, we establish an analytical framework for computing the rate coverage probability, which signifies the likelihood of achieving the target data rates for both the AUE and TUE. Leveraging these analytical findings, we conduct numerical analysis to determine the minimum altitude required for the AUE at each transmission point along its trajectory to satisfy specified quality of service (QoS) constraints across

various AUE target data rates and diverse built-up environments. Notably, our results emphasize the pivotal role of incorporating AUE trajectory modeling in the design of cellular-connected UAV systems.

Next, we present an adaptive system design tailored for an Internet of Things (IoT) monitoring network characterized by stringent latency and reliability prerequisites. In this network paradigm, IoT devices generate bursty, time-critical, and event-triggered traffic, while a UAV is deployed for aggregating and relaying sensed data to the base station. Conventional transmission schemes, predicated on overall average traffic rates, tend to overburden network resources during periods of smooth traffic flow and are susceptible to packet collisions during bursts of activity, such as events of interest. To mitigate these challenges, we propose an adaptive transmission scheme leveraging multiuser shared access (MUSA) through grant-free non-orthogonal multiple access, alongside employing short packet communication to ensure low-latency IoT-to-UAV communication. Specifically, to adeptly handle bursty traffic patterns, we develop an analytical framework and formulate an optimization problem aimed at maximizing performance by determining the optimal number of transmission time slots, while adhering to stringent reliability and latency constraints. Through comparative analysis with a non-adaptive power-diversity-based scheme featuring a fixed number of time slots, we demonstrate the superior reliability and stability of our proposed scheme, particularly under moderate to high average traffic rates, while meeting demanding latency requirements.

Finally, we investigate a UAV-assisted maritime-satellite communication network, wherein low-end maritime users (MUs) dispersed across a finite oceanic area establish communication with Low Earth Orbit (LEO) satellites via a swarm of UAV relays positioned within a finite aerial domain. We introduce a two-phase communication approach, wherein a reference UAV situated at an arbitrary location is served by its nearest MU in the MU-to-UAV communication phase, followed by relaying the received data to the closest satellite in the UAV-to-satellite communication phase. To analyze performance, we develop a location-dependent UAV-centric analytical framework, employing finite area stochastic geometry and success probability as the primary performance metric. Our analysis reveals a delicate balance between path loss and interference, influenced by the parameters of the satellite constellation, which directly impact the success probability. These

results provide theoretical insights for the deployment and planning of integrated maritime-aerial-satellite networks to extend coverage for low-end MUs in remote ocean regions.

List of Publications

The work in this thesis has been published or under preparation for publication as journal and conference papers. These papers are:

Journal papers:

J1: N. Senadhira, S. Durrani, X. Zhou, N. Yang and M. Ding, "Uplink NOMA for Cellular-Connected UAV: Impact of UAV Trajectories and Altitude," IEEE Trans. Commun., vol. 68, no. 8, pp. 5242-5258, Aug. 2020.

J2: N. Senadhira, S. Durrani, S. A. Alvi, N. Yang and X. Zhou " UAV-assisted IoT Monitoring Network: Adaptive Multiuser Access for Low-Latency and High-Reliability Under Bursty Traffic," (submitted to) IEEE Trans. Commun., May 2024, [Online], Available: https://arxiv.org/abs/2304.12684.

J3: N. Senadhira, S. Durrani, J. Guo, N. Yang and X. Zhou, " Design and Performance Analysis of UAV-Assisted Maritime-LEO Satellite Communication Networks", (submitted to) IEEE Open J. Commun. Soc., Oct. 2024.

Conference papers:

C1: N. Senadhira, S. Durrani, X. Zhou, N. Yang and M. Ding, "Impact of UAV Trajectory on NOMA-Assisted Cellular-Connected UAV Networks," Proc. IEEE ICC, Dublin, Ireland, 2020.

C2: N. Senadhira, S. A. Alvi, N. Yang, X. Zhou and S. Durrani, "Adaptive Multiuser Access for UAV-Assisted IoT Monitoring Networks Under Bursty Traffic," Proc. IEEE ICC Workshops, Rome, Italy, 2023.

List of Acronyms

UAV	Unmanned aerial vehicle
SINR	Signal-to-interference-noise ratio
XG	X-th generation
GSM	Global systems for mobile communications
SMS	Short message services
LTE	Long-term evolution
eMBB	Enhanced mobile broadband
mMTC	Massive machine-type communication
URLLC	Ultra-reliable low latency communication
3GPP	Third generation partnership project
IEEE	Institute of electronic engineers
ITU	International telecommunication union
ETSI	European telecommunications standards institute
FAA	Federation aviation authority
EASA	European aviation safety agency
HAPs	High altitude platforms
LAPs	Low altitude platform
GDP	Gross domestic product
RW1	Research work 1
RW2	Research work 2
RW3	Research work 3
BSs	Base stations
UEs	User equipments
LoS	Line-of-sight
NLoS	Non-line-of-sight
CoMP	Co-ordinate multi-point
NOMA	Non-orthogonal multiple access
OMA	Orthogonal multiple access
GB	Grant-based
GF	Grant-free
IoT	Internet of Things
MUSA	Multiuser shared access
SIC	Successive interference cancellation

AUVs	Autonomous underwater vehicles
MUs	Maritime users
LEO	Low Earth orbit
QoS	Quality of service
SSs	Surface stations
OSs	Onshore stations
TBs	Tethered balloons
SATs	Satellites
PPP	Poisson point process
HPPP	Homogeneous Poisson point process
BPP	Binomial point process
AUE	Aerial user equipment
TUE	Terrestrial user equipment
MUD	Multiuser decoding
NAS	Non-adaptive scheme
TPDS	Transmit power diversity scheme
PDF	Probability density function
CDF	Cumulative distributive function
A2C	Air-to-cellular
EoI	Event-of-interest
MSL	Mean sea level

List of Notations

R	Radius of a disk
$\mathcal{C}$	Disk region
h	Height
x	x-coordinate
y	y-coordinate
z	z-coordinate
$\mathcal{T}$	Trajectory
T	Time period
r	Horizontal distance
d	Euclidean distance
H	Small-scale fading gain
$\mathbb{P}_{\mathrm{LoS}}$	Probability of line-of-sight
ζ	Path loss
η	Path loss coefficient
α	Path loss exponent
m	Nakagami-m fading parameter
P_{T}	Transmit power
G	Antenna gain
σ^2	Noise Power
γ	SINR
θ	SINR threshold
$\mathbf{G}$	Equivalent channel
$\mathbf{S}$	MUSA sequence vector
$\mathbf{I}$	Identity matrix

I	Interference
B	Bandwidth
V	Channel dispersion
φ	Earth-centred zenith angle
ψ	Beamwidth
k	Rician fading parameter
$\beth$	Euler's constant
$\Gamma(x)$	Complete Gamma function
$\gamma(x, y)$	Lower incomplete Gamma function
$\mathbb{E}_X[\cdot]$	Expectation operator with respect to X
$F_X(\cdot)$	CDF of a random variable X
$f_X(\cdot)$	PDF of a random variable
$\mathfrak{L}_X(s)$	Laplace transform of the distribution of a random variable X
$\mathcal{M}_X(s)$	MGF of the distribution of a random variable X
$\mathbb{P}(\cdot)$	Probability measure
$\mathbb{Q}[\cdot]$	Q-function
$\mathbb{G}[\cdot]$	Barnes-G function
$\mathbb{H}[\cdot]$	Harmonic function
$\lfloor \cdot \rfloor$	Floor function

Contents

List of Figures

List of Tables

Chapter 1

Introduction

1.1 Background

Mobile communication networks have been undergoing exponential growth every decade as a results of rapid development of communication technologies, ongoing traffic explosion due to rapid growth in communication devices, and emerging applications demanding higher data rates and frequencies, broader bandwidths, lower latency, and higher reliability than the previous communication generations. The first generation (1G) cellular communication which was based on analogue transmissions was introduced in 1980s to support voice calls. Then in 1990s, 2G was developed to address the low capacity and reliability, and lack of security of 1G. 2G was based on the global systems for mobile communications (GSM) and supported short message services (SMS) in addition to voice calls compared to 1G [1,2]. Then, in 2000, 3G communication networks was introduced to support multi-data services such as internet surfing and video calls. Shortly after in 2009, 4G communication networks which is the long-term evolution (LTE) network was developed for fast mobile broadband to support mobile apps and streaming [2]. In 2019, 5G network was introduced to enable enhanced Mobile Broadband (eMBB) which require higher data rates, massive Machine-Type Communications (mMTC) which require massive connectivity, and Ultra-Reliable and Low Latency communications (URLLC) which demand stringent reliability and latency requirements [2]. Unlike previous communication generations which solely prioritized the network improve-

ments, 5G focuses on inter-connectivity among humans, machines and things, and also from consumer to vertical industries. This has lead to emergence of novel use cases such as autonomous cars, smart cities, virtual reality, unmanned aerial vehicles (UAVs), factory automation, remote surgery, etc. In this thesis, we focus on one of the aforementioned interesting use cases which is UAVs in 5G wireless communications.

UAVs or drones are small aircrafts controlled remotely by pilots or embedded computer programs, which were originated as military devices for surveillance, reconnaissance, to perform targeted air strikes and precision warfare in hostile territories, due to its inherent attributes such as mobility, flexible deployment, autonomy, ability to establish line-of-sight, and adjustable altitude [3]. Owing to rapid advancements of 5G and beyond 5G wireless networks, rapid advancements in miniaturization, control, computerization, cost reduction in UAV's manufacturing technologies, and accelerated involvement in industrial and research sectors, UAVs have been regarded as enablers of various industrial, commercial and civilian applications. UAVs are being used in package delivery, precision agriculture, smart healthcare, search and rescue, intelligent transport systems, remote sensing, goods delivery, aerial photography and transporting human organs across a city, and to perform environmental monitoring as they have the capability to access complex and harsh environments [4].

In order to seamlessly and safely integrate UAVs on to airspace, standardization bodies such as the Third Generation Partnership Project (3GPP), Institute of Electronic Engineers (IEEE), International Telecommunication Union (ITU), European Telecommunications Standards Institute (ETSI), Federation aviation authority (FAA), and European Aviation Safety Agency (EASA) have developed standards and conformity assessments that is required to support UAV connectivity, by identifying requirements, protocols and, technologies for aerial communications. UAV-enabled use cases that would be supported in 5G networks was identified in 3GPP TR 22.829, and network infrastructure and protocols to facilitate identification, connectivity and tracking of UAVs was addressed in 3GPP TR 23.754 [5–8]. Moreover, 3GPP Release 18 which was released in 2023 addressed UAV user identifications and collision avoidance to ensure compliance with recent changes in regulatory requirements [9]. Several IEEE committees focused on issues

such as air-to-air communications, traffic management for low altitude UAVs, and their applications, and ITU established stable and functional architecture for UAVs to access IMT-2020 as user terminals [5,6,10]. Both FAA and EASA implemented regulatory frameworks for UAVs [6]. Thus, all of the aforementioned standardizing initiatives have contributed to increase in compatibility among telecommunication vendors and to mitigate network operation and device costs for UAV use cases [11].

1.1.1 UAV Classifications and Use Cases

UAVs can be categorized based on their operating altitudes as, (i) high altitude platforms (HAPs) and low altitude platforms (LAPs). HAPs operate above 17 km, quasi-stationary, expensive, have longer endurance and deployment times compared to LAPs. On the other hand, LAPs operating altitudes range from tens of meters up to a few kilometers, flexible, have quick mobility, cost-effective, can be easily recharged or replaced when required and can be quickly deployed [12]. UAVs can also be categorized into fixed-wing and rotary-wing UAVs based on the type where, fixed-wing UAVs are small aircrafts that need to move forward to remain in air, whereas rotary-wing UAVs have the capability hover and remain stationary [12]. It is evident that it is important to carefully choose the appropriate type of UAV to suit the needs of various UAV use cases. **Therefore, in this thesis, we focus on LAP UAVs due to their desirable and interesting attributes.**

Moreover, UAVs that have wireless communication capabilities have the ability to gather and transmit data, perform tasks autonomously, coexist with other UAVs and/or terrestrial and/or non-terrestrial users, and provide reliable, on-demand, and, cost effective wireless communication services in wide range of real-world situations [13]. Thus, developing network support for UAVs has, therefore, been a hot topic of recent research [3,10,12,14,15]. Depending on whether UAVs are used as base stations to assist wireless communication of ground users, or as aerial users, there are two main paradigms for incorporating UAVs into cellular networks [3]: (i) UAV-assisted wireless communications where UAVs are employed to enhance coverage and support connectivity of existing communication networks and (ii) cellular-connected UAVs where UAVs are used as aerial users.

Cellular-connected UAVs are being used in a wide range of industries across

Australia such as; (i) farming where, UAVs are used across Queensland for surveillance, management of water and assets, and ground analysis, (ii) remote health where, UAVs are used in Nothern Territory to deliver medical supplies to remote communities quickly and efficiently, (iii) disaster relief and rescue where, UAVs are used by New South Wales Fire and Rescue for damage assessment of infrastructure, thermal imagery, and identify potential hazards and debris, during flood and fire emergencies, while enabling immediate disaster responses and ensuring the safety of rescue teams, (iv) media and entertainment where, UAVs are used in the filming industry and vivid drone displays in Sydney and Adelaide [16, 17]. Thus, it is evident that applications of cellular-connected UAVs in civilian, industrial and, commercial sectors have accelerated in the recent years. Moreover, it has been estimated that a medium level of UAV uptake in Australia will boost real gross domestic product (GDP) by AUD 14.5 billion with a cost saving of AUD 9.3 billion across the aforementioned sectors between 2020 and 2040 [18].

On the other hand, next generation wireless networks are expected to employ UAV-assisted wireless communications to handle the exponential rise in user demands and traffic explosions, and to provide reliable, on-demand and cost-effective wireless coverage for devices without infrastructure coverage due infrastructure damage caused by natural disasters, short-transmission range of devices due to low transmit powers, severe shadowing by urban and mountain terrain, etc. [19]. Apart from numerous applications of UAVs used as aerial BSs in cellular 5G networks while complementing terrestrial infrastructure, UAVs can also be used in maritime communication networks to provide on-demand services onboard and, used as relays or access points in emergency scenario use cases such as disaster reporting, remote sensing, volcanic eruption reporting and, forest fire monitoring [20]. Compared to cellular-connected UAVs that are widely employed in numerous use cases across Australia, deployment of UAV-assisted wireless communications is still at its infancy. However, due to desirable attributes of UAVs compared to fixed communication infrastructure, there is an increasing interest in investigating UAV-assisted wireless communications such as (i) UAV-aided ubiquitous coverage, (ii) UAV-aided relaying and, (iii) UAV-aided information dissemination and data collection, in UAV-centric research [19].

1.1.2 Thesis Motivation

Thus, in this thesis, we have selected three interesting use cases of UAVs within the aforementioned paradigms in various integrated aerial networks, that are relevant to current and future trends of UAV applications in Australia and world-wide. Specifically, in Research Work 1 (RW1), presented in Chapter 2, we consider a UAV use case in cellular-connected UAVs paradigm where a UAV user is employed for surveillance or monitoring applications. In RW1, we consider an integrated aerial-terrestrial communication network investigate how to seamlessly and efficiently integrate aerial user equipments (AUEs) into existing cellular networks with terrestrial UEs, while accounting for UAV's mobility. In Research Work 2 (RW2), presented in Chapter 2, we consider a UAV use cases in UAV-assisted communication paradigm where IoT devices are deployed to monitor an event of interest in practical scenarios such as bushfire detection, and consider an integrated aerial-IoT communication network, where a UAV is deployed as a data aggregator in a UAV-assisted IoT monitoring network with high reliability and low latency requirements to increase communication range and improve reliability. In Research Work 3 (RW3), presented in Chapter 4, we consider a futuristic UAV-assisted communication paradigm use case in an integrated aerial-maritime-satellite communication network where, UAVs are deployed as aerial relays in a finite aerial region to facilitate communication between Low Earth Orbit satellites and low-powered and short-range maritime users that are located in a finite maritime region which is out of the coverage area of onshore base stations. The overview of the research works presented in this thesis is illustrated in Fig. 1.1.

Having identified the research works, we mainly use stochastic geometry as the analytical tool to formulate and analyze the system models of use cases corresponding to each research work in this thesis. Stochastic geometry is regarded as a powerful tool for performance analysis of cellular and ad-hoc networks and, as an alternative to system-level simulations which are error susceptible, extremely time consuming, involve complex operations and, have high resource requirements. Although, system-level simulations are essential in network analysis, analytical approaches can provide tractable theoretical frameworks, can reveal parameter dependencies and trends, and are useful in benchmarking and performance compar-

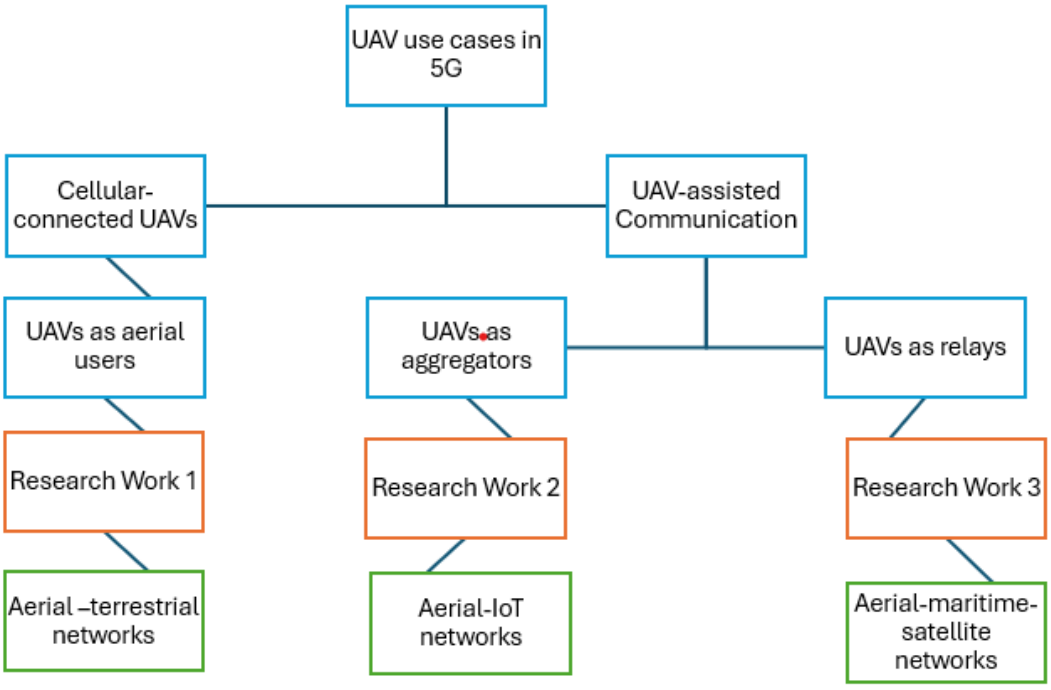

Figure 1.1: Flow diagram of thesis overview

isons [12,21]. In stochastic geometry, the locations of devices are modeled as point processes to evaluate performance metrics such as coverage or outage probability, throughput, rate and delay, in order to characterize the system performance [12]. Thus, in this thesis, we adopt suitable and realistic point processes to model the locations and/or trajectory processes of UAVs, terrestrial users, IoT devices, maritime users, and satellite constellations, and exploit tools from stochastic geometry to formulate tractable frameworks to characterize the performance, and also use optimization theory in RW2 to design the system.

1.2 Motivation and Literature Review

This section presents the motivation and state-of-the-art works that are relevant to the research works in each integrated aerial network corresponding to the research works stated in Section 1.1.

1.2.1 Research Work 1: Integrated Aerial-Terrestrial Networks

While UAV-assisted wireless communications, where UAVs act as aerial base stations (BSs), access points, relays, data aggregators, are regarded as a promising futuristic paradigm, before leaping forward with the deployment of UAV BSs, cellular-connected UAVs as user equipments (UEs) are being considered by standardization bodies as a priority for now [15]. For instance, the 3rd Generation Partnership Project (3GPP) is expected to consider cellular-connected UAVs in Release-17, which is expected to be finalized by September 2021 [4]. Hence, how to seamlessly and efficiently integrate aerial user equipments (AUEs) into existing cellular networks with terrestrial UEs becomes an important problem.

Trials by a number of leading industry vendors have demonstrated the feasibility of using existing cellular networks to support UAVs in the low-altitude airspace [22, 23]. In particular, it has been shown that terrestrial BSs with downtilted antennas provide adaquate coverage via antenna side lobes for UAVs flying below 120 m [10]. While the antenna side lobes have reduced gain, this is offset by favorable line-of-sight (LoS) links. However, at higher altitudes, the gain from LoS links diminishes and the coverage becomes insufficient. In [24], the use of co-ordinated multi-point (CoMP) transmission was investigated for serving aerial users, which was shown to increase the coverage up to 200 m altitude. The results in [14, 22–24] assumed dedicated resources allocated to an aerial UE. However, this may not be efficient in future wireless networks as the resources dedicated to aerial users may be underutilized [14].

Recently, non-orthogonal multiple access (NOMA) has been proposed as a promising technology to address the resource scarcity issue in wireless communications [25]. The basic idea of NOMA is to serve multiple users in the same resource block, leading to more efficient resource utilization compared to conventional orthogonal multiple access [26, 27]. The use of NOMA in UAV-assisted wireless communication has been widely explored [28–33]. These studies focused on UAVs serving terrestrial users using NOMA in both microwave [28] and mmwave [29] bands, resource allocation [30], user association strategies [33] or trajectory optimization problems [28,31,32]. *On the other hand, only a few studies have investigated the use*

of NOMA in cellular-connected UAV networks [34–36]. A beamforming strategy exploiting NOMA technique was proposed in [34] to allow a UAV to send its data to a selected subset of terrestrial BSs, which decode the UAV signal and then cancel it before decoding the messages of their served terrestrial users. By assuming the co-operative interference cancellation among the terrestrial BSs via backhaul links, a co-operative NOMA scheme for cellular-connected UAVs was proposed in [35]. The energy efficiency of a NOMA scheme in a downlink mmwave cellular-connected UAV network was investigated and optimized in [36]. However, the coexistence of terrestrial and aerial UEs and the ability of UAVs to move in the horizontal plane was not considered in [36]. The work in [37] developed a NOMA clustering strategy where the terrestrial and aerial devices in different power zones were clustered together. Moreover, [37] used stochastic processes to model the locations of the UAVs. In addition, [34] and [35] assumed that the UAVs are located in fixed locations and ignored the impact of UAVs' trajectories on the system performance.

Mobility is an intrinsic characteristic of UAVs. The movement of a UAV results in a UAV trajectory which can be given or optimized. Given or pre-defined trajectories are important in some practical scenarios where the UAV has a primary task such as surveillance of building assets, inspection of power lines or image surveys over a large farm field etc. The UAV trajectory must be properly accounted for in the modeling and design of UAV systems. In UAV-assisted wireless networks, different approaches have been taken to model the trajectory of aerial BSs. Studies adopting optimization techniques focused on optimal positioning [38,39] or trajectory planning [40–42] problems and determined what path UAV should follow. Studies adopting stochastic geometry techniques typically assumed stationary UAVs and modeled them using Poisson or Binomial Point Processes [43–47]. Recently, some progress has been made in the trajectory modeling of UAVs. Two trajectory processes for aerial BSs that provide the same uniform coverage behavior as the uniform Binomial Point Process were proposed in [48]. Inspired from the UAV trajectory model used in 3GPP study in [49], [50] modeled the initial locations of the UAV as a Poisson point process and assumed that they move in straight lines in uniformly random directions at a constant height and speed. Moreover, [51] used Random walk and Random waypoint models to model the UAV movement in spatial and vertical directions, respectively. However, the sys-

tem performance in [50, 51] was characterized from a time-average perspective, rather than the location of the UAV at a particular point along its trajectory. For cellular-connected UAVs, the prior relevant studies in [34–36] have considered stationary aerial users only. *To the best knowledge of the authors, the use of NOMA to efficiently serve both aerial and terrestrial users, while accounting for the given trajectory of cellular-connected UAVs, has not been investigated in the literature to date.*

1.2.2 Research Work 2: Integrated Aerial-IoT Sensor Networks

According to the International Disasters Database, 432 catastrophic events were recorded globally in 2021, which is significantly higher than the average of 357 annual extreme weather events recorded between 2001 and 2020 [52]. Such events come at a huge ecological, social and financial cost. For instance, it is estimated that the direct cost from extreme weather events will reach $35 billion by 2050 in Australia [53]. Thus, there is a great interest in IoT-based environmental monitoring systems which can provide early warnings to help mitigate economic and social impacts and to improve the disaster resilience of communities and countries.

Recently, IoT-based environmental monitoring networks have been deployed to monitor an event of interest (EoI) in practical scenarios such as (i) bushfire detection [54], (ii) hazardous gas detection in a volcanic area [55], and (iii) water pollution monitoring systems [56]. These systems generate heterogenous traffic, depending on environmental conditions. Under the normal condition, IoT devices measure environmental data and send smooth, non-real time, and low-rate traffic data to a control center [57, 58]. However, when an EoI is detected, IoT devices generate uplink dominant and time-critical high-rate traffic, which may include information about the crisis event and corrective actions to resolve the event. *Thus, it is important to design IoT-based environmental monitoring networks to meet high-reliability and low-latency requirements when an EoI occurs, which motivates this work..*

UAV for IoT-based Environmental Monitoring Networks: The IoT devices are typically low-cost battery-limited sensors with limited computational capabilities,

and have short transmission range which is inadequate to reach high altitude platforms and satellites [59]. If the IoT devices are deployed in an area with poor wireless coverage, e.g., in a mountain or forest area with no terrestrial cellular infrastructure, the reliable and low-latency transmission of data becomes a major challenge [12, 60]. In such deployment, unmanned aerial vehicles (UAVs) can be strategically deployed in IoT environments to increase the communication range of the IoT devices and improve the reliability of IoT communications [12, 61–63]. Consequently, the IoT devices can transmit data with low transmit power, resulting in prolonged battery life [12]. Also, due to the aerial nature, UAVs have the capability to establish line-of-sight communication links with the IoT devices. This would further favor IoT communications by mitigating shadowing and signal blockage in communication links compared to terrestrial communications [12, 60, 61, 64]. Thus, UAVs are considered as an attractive solution to IoT data aggregation before transmitting to a cellular base station (BS).

Multiple Access Protocol for IoT-based Environmental Monitoring Networks: To support the connectivity of IoT devices, two main access protocols have been proposed in the literature [65], namely, orthogonal multiple access (OMA) and non-orthogonal multiple access (NOMA). In OMA, the radio resources are only occupied by a single device. In NOMA, this limitation is overcome by multiplexing devices over a single channel resource [66–68]. Thus, NOMA is suitable for IoT-based environmental monitoring networks due to its large availability for using channel resources.

The channel resource access protocol of multiplexing users in NOMA needs to be carefully chosen. In the conventional grant-based (GB) access, the users perform uplink scheduling requests via contention-based random access, which is known as a performance bottleneck due to its high latency and signaling overhead [65]. On the other hand, grant-free (GF) access, where the IoT devices are able to wake up and transmit, is preferred for low-latency transmission and also reduces the power consumption of the IoT devices [69]. Thus, GF-NOMA is a suitable multiple-access protocol for IoT-based environmental monitoring networks.

Recently, multiuser shared access (MUSA) has been proposed as a signature-based GF-NOMA scheme [65, 66]. MUSA utilizes smart interfering management methods, i.e., successive interference cancellation (SIC), and exploits device-specific

signatures to decode the data at the receiver [65, 66]. In MUSA, devices autonomously and randomly choose complex-valued short spreading codes with low cross-correlation whenever they have data to transmit. Thus, no resource coordination is required at the devices. Due to the additional design freedom provided by the real and imaginary components of the spreading code, the active devices have the option to choose from a wide range of low cross-correlation sequences of short length. This minimizes the sequence collisions within a given time-frequency resource block, while improving the detection probability at the receiver [65,69–71]. The spreading codes are also designed to simplify SIC at the receiver [65]. Thus, MUSA is a suitable GF-NOMA multiple-access protocol for IoT-based environmental monitoring networks.

Short Packet Communication for IoT-based Environmental Monitoring Networks: To enable low-latency IoT communications, we use short packet communication by employing short frame structure and short packets [66,72]. Due to the short packet size and the low-latency requirements, the decoding errors in such communications cannot be ignored and the decoding probability cannot be characterized by Shannon's capacity without underestimating the latency and reliability [72, 73]. In the finite block regime, the short packet transmission error probability has been characterized in the literature [74].

State-of-the-Art in the Literature: Next, we present the state-of-the-art in the literature related to MUSA-based GF-NOMA and short packet communications. Recently, several studies have proposed to use NOMA in short packet communications to reduce the latency of time-critical applications while improving the spectral efficiency [75–77]. Moreover, the aforementioned merits of utilizing UAVs in the IoT infrastructure have motivated the modeling and analysis of UAV-assisted IoT networks with short packet communication to improve reliability, latency, throughput, and energy efficiency [64, 78–82]. Despite that the performance analysis of NOMA in IoT networks in the infinite block regime using stochastic geometry has also been widely investigated in literature [83–85]. There lacks analytical frameworks to evaluate the performance of MUSA-based short packet communication in UAV-assisted IoT networks. Prior studies on short packet communication have been mostly limited to the case of two NOMA users or a single transmitter-receiver pair [68], while the studies focusing on multiuser NOMA have not addressed short

packet communication [86], latency [87], or UAV data aggregation [88]. For example, [68] analyzed the outage performance in a semi-GF system where GF users and GB users share the same spectral resources in a two-user NOMA scenario. An analytical model of a GF-NOMA machine-type communication system was proposed in [86] where the aggregate data rate without considering short packet decoding errors was analyzed. In [87], SIC decoding was designed based on power-domain NOMA which relies solely on the channel diversity of devices, while the latency requirements of short packets were not considered. The average system throughput under massive NOMA in the infinite and finite block length regimes was derived in [88], where UAV-assisted data aggregation was not addressed. *To the best of our knowledge, there is no solution available to analyze and satisfy the high-reliability and low-latency requirements when an EoI occurs in a UAV-assisted IoT-based environmental monitoring network, which motivates our work.*

1.2.3 Research Work 3: Integrated Maritime-Aerial-Satellite Networks

Safeguarding the world's oceans, which relates to UN Sustainable Development Goals especially life underwater (Goal 14), through improved maritime communications and maritime internet-of-things has received increasing attention recently [89, 90]. Maritime applications, such as marine tourism, transportation, offshore aquaculture and mineral exploration, search and rescue, coastal defence and monitoring ocean health, are mainly categorised into underwater and overwater layer applications. Underwater layer is comprised of underwater sensor nodes deployed in shallow sea areas to monitor oceanic parameters, and autonomous underwater vehicles (AUVs) that can move to target underwater areas to conduct topographic mapping, ocean explorations, etc. [91]. Overwater layer is comprised of high-end maritime users (MUs) such as ships, low-end MUs such as buoys, and maritime infrastructure such as drilling platforms and wind power plants [91]. A key challenge to support safe, secure and sustainable maritime activities is extending network coverage over the oceans, which cover 71 per cent of the planet's surface.

Currently, overwater MUs rely on onshore base stations (BSs) to provide coverage. The use of ship borne and unmanned aerial vehicle (UAV) enabled BSs can ex-

tend the range to a certain extent. However, this communication infrastructure has inherent limited coverage as BSs cannot be installed far offshore in oceans [92, 93]. Therefore, to enable wider coverage to overwater users that are out of the coverage region of onshore BS, satellite communication is employed [89]. At present, many operators are building new low Earth orbit (LEO) satellite networks that will provide truly global network coverage, including over remote oceans. However, directly connecting to satellites requires high-end MUs that have high transmit powers, large antenna gains and costly equipment [94]. Low-end MUs generally lack the technology to connect directly to satellites, as even LEO satellites deployed at lower altitudes between 300 to 2000 km are located far away from the low-powered and short-range buoys [94]. In particular, low-end buoys having meteorological and oceanographic data, are expected to be increasingly deployed to better monitor the climate and help maintain clean, healthy oceans that support human livelihoods. In this regard, UAVs can be utilized as relays to enable multi-hop communication between buoys and satellites as they can be flexibly deployed from ships at closer proximity to the buoys [90, 92]. Thus, it is crucial to investigate integrated maritime-aerial-satellite solutions to extend LEO satellite network coverage for low-end MUs.

Related work: Integrated maritime-aerial-satellite networks have been considered in only a few existing works [94–98]. Work in [94] proposed a novel space-air-sea network where high-end users directly communicate with a satellite, while low-end users communicate with a satellite via UAVs, and investigated energy-efficient resource allocation problem. However, this work used simulations and only considered a single satellite, as opposed to satellite constellations. [95] minimized the energy consumption while guaranteeing the quality of service (QoS) of a hybrid satellite-UAV-terrestrial maritime communication network consisting of a single satellite, single onshore BS, multiple UAVs, and multiple vessels. However, in this model, the satellite is only used to provide signals for the maritime area but not incorporated in the analysis. Moreover, Stochastic geometry has been used to evaluate network performance analytically for underwater-to-surface communication, and surface communication to onshore BS or UAV or satellite communications [96–98]. [96] proposed a space-air-ground-sea integrated network (SAGIN) where surface stations (SSs) transmit to terrestrial BSs via four types of relays

Table 1.1: Related works

Reference	Communication link	Distribution model	Performance metric	Limitations
Satellite Communications				
[99]-2020	Uplink	Multiple satellites with HPPP and terrestrial users (TUs) with HPPP	SIR	Homogenous distribution of TUs on Earth
[100]-2020	Downlink	Multiple satellites with BPP and single TU in Voronoi cell of each satellite	SINR	Homogenous distribution of TUs on Earth
[101]-2020	Uplink and downlink	Multiple satellites with BPP and homogeneous distribution of TUs	SNR	Homogeneous distribution of TUs on Earth
[102]-2021	Uplink and downlink	Multiple satellites with NPPP and single TU	SNR	Single TU
[103]-2021	Downlink	Multiple satellites with HPPP and single user	SINR	Single user
[104]-2021	Uplink	Multiple satellites with HPPP, terrestrial BSs with HPPP, and users with HPPP	SINR	Homogeneous distribution of users and BSs
[105]-2021	Downlink	Single satellite, multiple terrestrial relays with HPPP and single TU	SINR	Single TU and single satellite
[106]-2021	Downlink	Multiple satellites with homogeneous BPP, satellite gateways with HPPP, and single TU	SNR	Single TU
[107]-2022	Downlink	Multiple satellites with non-homogenous PPP (NPPP) and single TU	SINR	Single TU
[108]-2022	Uplink	Multiple satellites with HPPP and IoTs with HPPP	SINR	Homogeneous distribution of users
[109]-2022	Uplink	Single satellite and multiple IoTs with HPPP	SINR	Single satellite
[110]-2022	Uplink	Multiple satellites with homogenous BPP and users with homogeneous BPP	SINR	Homogenous distribution of users
[111]-2022	Downlink	Multiple satellites with homogeneous BPP and single TU	SNR	Single TU
[112]-2024	Downlink	Multiple satellites with Cox point process and multiple users with independent PPPs	SINR	Homogenous distribution of users
Terrestrial Communications				
[113]-2017	User-user	Multiple transmitting users with BPP and single reference receiver	SIR	No satellites
[114]-2017	downlink	Multiple transmitting nodes with BPP and single reference receiver	SIR	No satellites
[44]-2017	Downlink	Multiple UAVs with BPP and single reference receiver	SIR	No satellite
[115]-2021	UAV-user	Multiple UAVs with BPP and single target user	SINR	No satellites
Maritime Communications				
[96]-2023	Uplink	Single SS, multiple terrestrial BSs, with multiple OSs, TBs, HAPs and SATs as relays	SINR	OSs, TBs and HAPs modeled as 1D PPP and single SS
[97]-2023	Uplink and downlink	Multiple satellites with BPP, single transmitting BS and single MU	SNR	Single MU and no UAVs
[98]-2022	Uplink	Multiple surface sink nodes with HPPP and single UAV	SINR	Single UAVs and no satellites
This work	Uplink	Multiple MUs and UAVs with finite BPP, and multiple satellites with HPPP	SINR	–

such as onshore stations (OSs), tethered balloons (TBs), high altitude platforms (HAPs), and satellites (SATs). However, in this work, OSs, TBs and HAPs were modeled as one-dimensional (1D) Poisson point process (PPP), and only a single transmitting SS was considered. [97] modelled a LEO-satellite aided shore-to-ship communication network considering direct BS-to-ship and indirect BS-to-satellite-ship communication links. However, this work considered a single transmitting BS, single destination ship, and assumed that the ship has the ability to communicate directly with the onshore BS or satellites. Moreover, aerial networks were not integrated in this model. [98] proposed a UAV-assisted underwater sensor model, where underwater sensor nodes transmit data to UAVs via surface nodes such as buoys. However, the performance analysis of surface sink to-UAV link was limited to a single UAV, and satellite communication was not incorporated in this work.

Stochastic geometry has been widely used for performance analysis in satellite communications works such as, [99–112], as specialized softwares used for satellite constellation modeling do not provide tractable analytical insights, and such simulations are error susceptible, extremely time consuming, involve complex operations and, have high resource requirements [12, 21, 116]. As summarized in Table I, prior works mostly focused on terrestrial satellite communications, and either considered a single user located at a reference location or a homogeneous Poisson point (HPPP) distribution of users on the surface of Earth. Such works have carried out satellite-centric analysis in the downlink as interference is generated by satellites within the local dome in downlink, and user-satellite-centric analysis in

the uplink as interference is generated by ground users within the satellite footprint in the uplink [116]. In reality, terrestrial and maritime users are distributed in finite geographical areas, and the performance of such networks is location-dependent due to varying satellite association probabilities and interference. Prior works in terrestrial and aerial communications have conducted finite stochastic geometry analysis by modelling the distribution of terrestrial/aerial users using finite two-dimensional (2D) binomial point processes (BPP) [44,113–115]. *However, there lacks prior literature that incorporates satellite communication into finite area integrated maritime-aerial-satellite networks. In addition, location-dependent performance analysis means that, instead of the conventional user-centric analysis, we must employ UAV-centric analysis in the uplink in integrated maritime-aerial-satellite networks. Thus, we address the issue of providing network coverage to low-end MUs in the context of integrated maritime-aerial-satellite networks, while considering finite region distribution of maritime users and UAVs, satellite constellation parameters and curvature of Earth. To the best of our knowledge, such analysis has not been conducted in the prior literature.*

1.3 Thesis Overview and Contributions

The main focus of this thesis is the performance analysis and design of interesting use case of UAVs in 5G wireless communications, where UAVs are integrated with terrestrial, IoT, maritime and, satellite communication networks, using techniques such as infinite and finite area stochastic geometry and, optimization. The specific contributions of each chapter in this thesis are presented below:

1.3.1 Chapter 2: Uplink NOMA for Cellular-Connected UAV: Impact of UAV Trajectories and Altitude

In this work, we focus on a cellular-connected aerial UE (AUE) employed for surveillance or monitoring a cellular region. The AUE periodically transmits its data to the BS with a target data rate requirement. For efficient spectrum usage, we enable the concurrent uplink transmissions by the AUE and a terrestrial UE (TUE) by employing power-domain aerial-terrestrial uplink NOMA. The main contributions

of this work are as follows:

- We consider a successive interference cancellation (SIC) decoding strategy where the BS decodes the AUE first by treating the TUE as interference. If the AUE cannot be decoded then the BS tries to decode the TUE first and then the AUE. This decoding order leverages the fact that generally AUE link is stronger than the TUE one due to the favorable line-of-sight propagation. However, if the AUE is flying close to the cell edge and the TUE is located close to the BS, then the TUE link may be stronger than the AUE link.

- Using stochastic geometry, we develop a general analytical framework to compute the rate coverage probability, i.e., the probability that the achievable data rates of both the AUE and TUE exceeds the respective threshold target rates. The proposed framework explicitly incorporates the given trajectory of a cellular-connected AUE. Using the proposed framework, we determine the minimum height of the AUE for each transmission point along its given trajectory in order to meet a certain quality of service (QoS) in terms of the coverage probability for different built-up environments.

- Our results show that for a spiral trajectory, the minimum height increases as the AUE moves from the center to the cell edge. For low to moderate AUE target data rates, the target QoS is satisfied along the entire trajectory for suburban, urban and dense urban environments, and along the initial part of the trajectory for the urban high-rise environment. For the trajectory model adapted from the 3GPP recommendations, the minimum height of the AUE depends on its distance from the BS. The results highlight the importance of modeling the trajectory in the design of NOMA-assisted cellular-connected AUEs.

The results of this chapter have appeared in the following publications [117] [118].

J1: N. Senadhira, S. Durrani, X. Zhou, N. Yang and M. Ding, "Uplink NOMA for Cellular-Connected UAV: Impact of UAV Trajectories and Altitude,"

IEEE Trans. Commun., vol. 68, no. 8, pp. 5242-5258, Aug. 2020.

C1: N. Senadhira, S. Durrani, X. Zhou, N. Yang and M. Ding, "Impact of UAV Trajectory on NOMA-Assisted Cellular-Connected UAV Networks," Proc. IEEE ICC, Dublin, Ireland, 2020.

1.3.2 Chapter 3: UAV-assisted IoT Monitoring Network: Adaptive Multiuser Access for Low-Latency and High-Reliability Under Bursty Traffic

In this work, we consider a UAV-assisted IoT-based environmental monitoring system generating heterogeneous traffic with specific reliability and latency requirements. For this system, we develop an analytical framework to analyze the performance of short packet communication, and optimize the performance to satisfy reliability and latency requirements. The main contributions of this work are:

- We propose an adaptive transmission scheme for a UAV-assisted IoT-based environmental monitoring network, where IoT devices generate short packets with stringent latency and reliability requirements and produce heterogeneous traffic when an EoI occurs. The proposed scheme employs MUSA-based GF-NOMA, with ideal multi-user decoding (MUD) at the UAV, to enable IoT-to-UAV communications.

- We analyze the statistical performance of the MUSA-based GF-NOMA scheme and MUD at the UAV using the signal-to-interference-plus-noise ratio (SINR) coverage probability, which is defined as the average probability that a packet transmitted by a device during a given time slot in a transmission frame is not subjected to MUSA collision and the SINR exceeds a certain threshold. We also address the decoding error at the UAV due to transmission of short packets by considering short packet transmission error probability subject to packet size and transmission duration.

- We design an adaptive transmission scheme for the IoT-to-UAV communication by formulating and solving an optimization problem. We maximize

the SINR coverage probability for a device with multiple packets to transmit, given a stringent latency constraint, by optimizing the number of transmission time slots, while satisfying the short packet reliability requirements with respect to short packet transmission error probability. The proposed scheme prevents the over-utilization of time-frequency resources under low-rate traffic and under-utilization of resources under high-rate traffic in an EoI.

- We compare our proposed scheme with a transmit power diversity scheme (TPDS) and a non-adaptive scheme (NAS). Our results show that the proposed scheme outperforms NAS and exhibits superior reliability and stability than the state-of-the-art TPDS at moderate to high average traffic rates. The results demonstrate the potential of UAV-assisted short packet communication with MUSA-based GF-NOMA to process high-rate traffic data when an EoI happens in an IoT-environmental monitoring system.

The results of this chapter have appeared in the following conference publication [119] and under preparation for journal submission [120].

C1: N. Senadhira, S. A. Alvi, N. Yang, X. Zhou and S. Durrani, "Adaptive Multiuser Access for UAV-Assisted IoT Monitoring Networks Under Bursty Traffic," Proc. IEEE ICC Workshops, Rome, Italy, 2023.

J2: N. Senadhira, S. Durrani, S. Alvi, N. Yang and X. Zhou, " UAV-assisted IoT Monitoring Network: Adaptive Multiuser Access for Low-Latency and High-Reliability Under Bursty Traffic," (submitted to) IEEE Trans. Commun., May 2024, [Online], Available: https://arxiv.org/abs/2304.12684.

1.3.3 Chapter 4: Design and Performance Analysis of UAV-Assisted Maritime-LEO Satellite Communication Networks

Contributions: In this work, we consider a UAV-assisted maritime-satellite communication network, where low-end MUs, such as buoys, are distributed in a finite ocean region that is outside the coverage region of onshore BSs. The low-end MUs

transmit to a LEO satellite constellation via a swarm of UAVs hovering in a finite aerial region. For this network, we develop a UAV-centric analytical framework for MU-to-UAV and UAV-to-satellite communication links. Using stochastic geometry, we analyze the network performance as a function of the location of a reference UAV within the finite aerial region. The main contributions of this work are:

- We develop a maritime-aerial-satellite network architecture, which allow us to analyze the successful message reception from a MU to a reference UAV, and subsequent transmission from the reference UAV to its closest satellite in a tractable way. We consider two transmission phases, i.e., (i) MU-to-UAV and (ii) UAV-to-satellite. In the MU-to-UAV phase, a reference UAV hovering at an arbitrary location receives data from its closest MU, and in the UAV-to-satellite transmission phase, the same reference UAV hovering at an arbitrary location forwards the data received in the MU-to-UAV communication phase to its closest satellite. To capture the realistic deployment of MUs and UAVs, we model the spatial distributions within finite regions.

- For the considered network, our analytical framework is used to evaluate the UAV-location-dependent performance of the MU-to-UAV and UAV-to-satellite communication phases relative to a reference UAV located at an arbitrary location, using an effective performance metric, i.e., success probability, which characterizes the joint probability that (i) the transmission from MU to reference UAV is received successfully at the reference UAV, (ii) the reference UAV is uniquely associated with its closest satellite, and (iii) the transmission from the reference UAV is successfully received by its closest satellite. In this UAV-centric analysis, we consider the finite distribution of both MUs and UAVs, characterize the location-dependent aggregate interferences, signal-to-interference-noise ratios (SINRs), and association probabilities, accounting for satellite constellation parameters.

- Under realistic parameters settings, the analytical results match well with simulation results. Our numerical results show that for a given set of satellite constellation parameters (e.g., number of satellites, height, and beamwidth), there is an interplay between path loss and interference that determines the

success probability. The results provide theoretical guidance for the deployment and plan of integrated maritime-aerial-satellite networks, targeting to provide coverage for low-end MUs in remote ocean regions.

The results of this chapter are under preparation for journal paper submission [121]

J3: N. Senadhira, S. Durrani, J. Guo, N. Yang and X. Zhou, " Design and Performance Analysis of UAV-Assisted Maritime-LEO Satellite Communication Networks", (submitted to) IEEE Open J. Commun. Soc., Oct. 2024.

Chapter 2

Uplink NOMA for Cellular-Connected UAV: Impact of UAV Trajectories and Altitude

This Chapter considers an emerging cellular-connected unmanned aerial vehicle (UAV) architecture for surveillance or monitoring applications. We study a scenario of interest where a cellular-connected aerial user equipment (AUE) periodically transmits in uplink, with a given data rate requirement, while moving along a given trajectory. For efficient spectrum usage, we enable the concurrent uplink transmission of the AUE and a terrestrial user equipment (TUE) by employing power-domain aerial-terrestrial non-orthogonal multiple access (NOMA), while accounting for the AUE's known trajectory. To characterize the system performance, we develop an analytical framework to compute the rate coverage probability, i.e., the probability that the achievable data rate of both the AUE and TUE exceeds the respective target rates. We use our analytical results to numerically determine the minimum height that the AUE needs to fly, at each transmission point along a given trajectory, in order to satisfy a certain quality of service (QoS) constraint for various AUE target data rates and different built-up environments. Specifically, the results show that the minimum height of the AUE depends on its distance from the BS as the AUE moves along the given trajectory. Our results highlight the importance of modeling AUE trajectory in cellular-connected UAV systems.

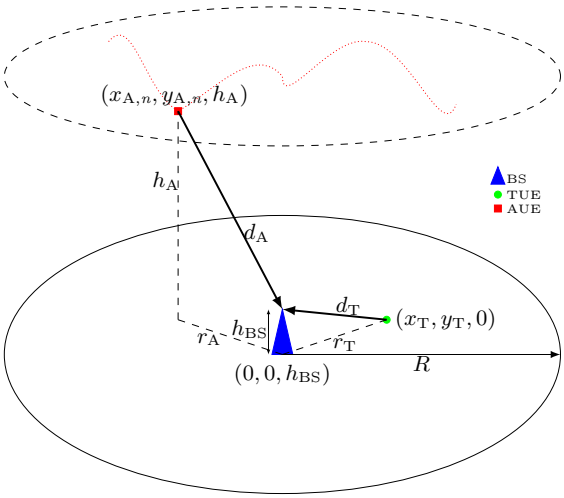

Figure 2.1: Illustration of the three-dimensional system model. Blue triangle, red square, and green circle represent the BS, AUE, and TUE, respectively. AUE's arbitrary trajectory is denoted by the red dotted line.

This Chapter is organized as follows. Section 4.1 details the system model and the assumptions. Section 2.2 describes the proposed NOMA scheme which enables the simultaneous uplink transmissions of the AUE and the paired TUE. Section 4.2 presents the analytical framework that is used to compute the rate coverage probabilities. Section 4.3 presents the results and highlights the impact of the system parameters on the system performance. Finally, Section 4.4 concludes the Chapter.

2.1 System Model

We consider a single-cell wireless communication system with one base station (BS), multiple terrestrial user equipments (TUEs), and multiple aerial user equipments (AUEs). We assume that each TUE is assigned an orthogonal time-frequency resource block in the uplink to transmit to the BS. This practical assumption is in line with the existing and near future cellular networks [122]. Hence, there is no intra-cell interference among the TUEs in the cell. The AUEs are employed for surveillance or monitoring the region and each AUE periodically transmits its data to the BS. Depending on the nature of surveillance, it also has a target data rate requirement. In this work, we assume that each AUE is not assigned a dedicated

resource block for its uplink transmission. Instead, for efficient spectrum usage, we assume that the TUEs can share their spectrum resources with the AUE. We assume that each AUE is randomly paired with a different TUE. Thus, the scenario of interest is simplified to the performance of a single AUE and a paired TUE. Under this assumption, there is intra-cell interference between the AUE's uplink transmission and a TUE's uplink transmission. Hence, we propose to use non-orthogonal multiple access (NOMA) to enable an efficient uplink communication between the AUE and BS by pairing the transmissions of the AUE and a random TUE. The TUE paired with the AUE is referred to as the active TUE[1]. Thus, the AUE transmits on the same resource block as the active TUE.[2]

2.1.1 Spatial Model

The single-cell is modeled as a disk region $\mathcal{S}$ with a radius R. Without loss of generality, we adopt the three-dimensional (3D) cartesian coordinate system in this work. The BS is located at the center of the cell at a fixed height h_{BS}, i.e., at coordinates $(0, 0, h_{\mathrm{BS}})$. In this work, we focus on the AUE pairing with a random TUE. Hence, an assumption on the number of TUEs is not required. We assume that the active TUE is randomly located in the disk region at coordinates $(x_{\mathrm{T}}, y_{\mathrm{T}}, 0)$ where $r_{\mathrm{T}} = \sqrt{{x_{\mathrm{T}}}^2 + {y_{\mathrm{T}}}^2}$ is the horizontal distance between the BS and the active TUE.

[1]Note that since the TUE is assigned an orthogonal resource block, the AUE is paired with a different TUE at each transmission point. Also, since we focus on the AUE pairing with a random TUE, an assumption on the number of TUEs and their mobility is not required.

[2]We assume that inter-cell interference coordination techniques are employed to mitigate terrestrial inter-cell interference, e.g., orthogonal resource block allocation to active TUEs in neighbouring cells [123, 124]. Since each AUE uses NOMA with TUEs in the corresponding cells, neither AUE nor the active TUE will share the same resource blocks across different cells. Thus, we assume the inter-cell interference is negligible in our case. Moreover, any unaccounted AUE inter-cell interference is also attenuated to the level below the background noise due to the ideal beamforming assumption as stated in Section II-D. Thus, in this work, we focus on the equivalent scenario of interest with a single BS and a single AUE-TUE pairing in a cell, without the presence of inter-cell interference.

2.1.2 AUE Trajectory and Mobility Model

The AUE trajectory and mobility model is illustrated in Fig. 2.1. We assume that the AUE flies along a given trajectory $\mathcal{T}$ to cover the disk region, with a constant speed v_{A} at an altitude h_{A} above the ground[3]. The AUE's uplink transmissions are periodic with time period T_{A}, resulting in N transmission points along the trajectory $\mathcal{T}$, i.e. , $\mathcal{T} \triangleq \{\mathcal{T}[n]\}_{n=1}^{N}$ where n is the transmission point index. In $\mathcal{T}$, we define N as $N = \lfloor \frac{s(\mathcal{T}[N])}{v_{\mathrm{A}} T_{\mathrm{A}}} \rfloor$, where $s(\mathcal{T}[N])$ is the total path length of $\mathcal{T}$ and $\lfloor \cdot \rfloor$ is the floor function. $\mathcal{T}[n] = (x_{\mathrm{A},n}, y_{\mathrm{A},n}, h_{\mathrm{A}})$ denotes the cartesian coordinates of the location of the AUE at the nth transmission point, where $r_{\mathrm{A},n} = \sqrt{{x_{\mathrm{A},n}}^2 + {y_{\mathrm{A},n}}^2}$ is the horizontal distance between the projection of the AUE on the ground and the BS.

2.1.3 Channel Model

Recently, progress has been made in the understanding of different types of channels in UAV communications [45,125,126]. The different channels can include, air-to-air channel model (between UAVs in the sky), air-to-ground/ ground-to-air channel model (between a UAV and an user on the ground) and cellular-to-air/ air-to-cellular channel model (between a UAV and an elevated terrestrial BS). Note that the distinction between air-to-ground and air-to-cellular lies in the non-negligible height of the terrestrial BS [45, 125, 126].

In our system model we have the following two types of links: (i) air-to-cellular (A2C) channel between the AUE and the terrestrial BS and (ii) terrestrial channel between the active TUE and BS.

The terrestrial channel is modeled as a combination of a large-scale path-loss attenuation, with path-loss exponent α_{T}, and small-scale Rayleigh fading component, with fading power gain H_{T}. Due to the path-loss, the transmit signal power of TUE decays at a rate ${d_{\mathrm{T}}}^{-\alpha_{\mathrm{T}}}$, where $d_{\mathrm{T}} = \sqrt{{r_{\mathrm{T}}}^2 + {h_{\mathrm{BS}}}^2}$ is the 3D propagation distance between the TUE and the BS. The small-scale Rayleigh fading gain H_{T} follows an exponential distribution with probability density function (PDF) and

[3]Note that the AUE is capable of varying its height along the course of the trajectory. In Sections 4.3 C-D we assume that the AUE flies at a constant height along the entire trajectory and, in Sections 4.3 E-F, we consider a case where the AUE can vary its height at each trajectory point to achieve a certain quality of service.

cumulative distributive function (CDF) of $f_{H_\mathrm{T}}(x) = e^{-x}$ and $F_{H_\mathrm{T}}(x) = 1 - e^{-x}$, respectively.

Following the state-of-the-art in [45, 125, 126], the air-to-cellular (A2C) channel is modeled as a combination of a probabilistic distance and height dependent large-scale path-loss and small-scale Nakagami-m fading, with fading power gain H_A. The path loss is determined according to whether the A2C channel is line-of-sight (LoS) or non-line-of-sight (NLoS) with probabilities of occurrence $\mathbb{P}_\mathrm{LoS}$ and $1-\mathbb{P}_\mathrm{LoS}$, respectively. In this work, we consider the International Telecommunication Union (ITU) model for determining the probability of LoS. The details are presented in Section 4.3. The corresponding path-loss is given as

$$\zeta_\mathrm{A} = \begin{cases} \eta_\mathrm{L} {d_\mathrm{A}}^{-\alpha_\mathrm{L}}, & \text{if LoS} \\ \eta_\mathrm{N} {d_\mathrm{A}}^{-\alpha_\mathrm{N}}, & \text{if NLoS,} \end{cases} \tag{2.1}$$

where $d_\mathrm{A} = \sqrt{{r_\mathrm{A}}^2 + (h_\mathrm{A} - h_\mathrm{BS})^2}$ is the 3D propagation distance between the BS and the AUE, η_ν, α_ν, $\nu \in \{\mathrm{L}, \mathrm{N}\}$ are the additional attenuation factors and path-loss exponents for LoS and NLoS channels. The small-scale Nakagami fading gain H_A follows a Gamma distribution with parameters for the LoS and NLoS channels denoted by m_L and m_N, respectively. The PDF and CDF of H_A are given by 2.2 and 2.3, respectively.

$$f_{H_\mathrm{A}}(x) = \mathbb{P}_\mathrm{LoS} \frac{m_\mathrm{L}^{m_\mathrm{L}} x^{m_\mathrm{L}-1} e^{-m_\mathrm{L} x}}{\Gamma(m_\mathrm{L})} + (1 - \mathbb{P}_\mathrm{LoS}) \frac{m_\mathrm{N}^{m_\mathrm{N}} x^{m_\mathrm{N}-1} e^{-m_\mathrm{N} x}}{\Gamma(m_\mathrm{N})} \tag{2.2}$$

$$F_{H_\mathrm{A}}(x) = \mathbb{P}_\mathrm{LoS} \sum_{i=0}^{m_\mathrm{L}-1} (m_\mathrm{L} x)^i \frac{1}{i!} e^{-m_\mathrm{L} x} + (1 - \mathbb{P}_\mathrm{LoS}) \sum_{j=0}^{m_\mathrm{N}-1} (m_\mathrm{N} x)^j \frac{1}{j!} e^{-m_\mathrm{N} x} \tag{2.3}$$

2.1.4 Received Signal

We assume that the TUE and AUE are equipped with single omnidirectional antennas. In order to serve both the active TUE and AUE simultaneously, the BS is equipped with a dual antenna array [46], i.e., BS can simultaneously beamform towards an active TUE and AUE, with associated antenna gains G_T and G_A, re-

spectively[4].

The AUE transmits with a fixed transmit power P_{A}. For the active TUE, we use the channel inversion power control [126, 127]. We assume that the BS has a receiver sensitivity of $\rho_{\min}$. Therefore, the active TUE adjusts its transmit power such that average signal power received at the BS is equal to the cutoff threshold ρ_{T}, where $\rho_{\mathrm{T}} > \rho_{\min}$. Hence,

$$P_{\mathrm{T}} = \rho_{\mathrm{T}} d_{\mathrm{T}}^{\alpha_{\mathrm{T}}}. \tag{2.4}$$

Based on the aforementioned system model, the received signal at the BS due to an AUE located at coordinates $(x_{\mathrm{A},n}, y_{\mathrm{A},n}, h_{\mathrm{A}})$ and an active TUE located at coordinates $(x_{\mathrm{T}}, y_{\mathrm{T}}, 0)$ is

$$\Psi_{\mathrm{BS}} = \sqrt{P_{\mathrm{T}} {d_{\mathrm{T}}}^{-\alpha_{\mathrm{T}}} H_{\mathrm{T}} G_{\mathrm{T}}}\Psi_{\mathrm{T}} + \sqrt{P_{\mathrm{A}} \zeta_{\mathrm{A}} H_{\mathrm{A}} G_{\mathrm{A}}}\Psi_{\mathrm{A}} + \mathfrak{n}, \tag{2.5}$$

where $\mathfrak{n}$ is the additive white Gaussian noise with variance σ^2, and Ψ_{ϱ}, $\varrho \in \{\mathrm{T}, \mathrm{A}\}$ denotes the signal transmitted by active TUE and AUE, respectively.

2.2 Proposed NOMA scheme

The simultaneous uplink transmissions of the AUE and the active TUE are facilitated by using power-domain aerial-terrestrial uplink NOMA with successive interference cancellation (SIC) at the BS. Power-domain NOMA utilizes the power domain for user multiplexing, allowing the active TUE and AUE to share a single time-frequency resource block [26, 27]. SIC allows the signals of each user to be decoded successively at the receiver end.

In the uplink terrestrial NOMA, the user with the strongest channel link quality is decoded first while treating the users with weaker link quality as interference. Then, the decoded signal is subtracted from the superimposed signal before decoding the users with weaker link quality. This process is continued until the user with the weakest link quality is decoded [26]. Due to analytical tractability, most

[4]In practical scenarios, AUEs maybe equipped with directional antennas with specific antenna gains. Since the BS is located at the centre of the circular cell and the AUE's location on its trajectory is deterministic, the antenna gain of AUE can be derived analytically. Thus, our analytical framework is still applicable in this case as the mathematical derivations accounts for G_{A}. However, the focus of this work is not on the complicated antenna modeling of the AUE. Thus, we use the ideal antenna model for simplicity.

studies in terrestrial uplink NOMA evaluate the channel link quality based on the average received power of each user, e.g., [128]. The channel link quality ranking assumes that the user closest to the BS has the strongest channel link quality and vice versa. Thus, the decoding order in this case is fixed and distance dependent. However, the fixed decoding order ignores the possibility where the closer user experiences severe small-scale fading and farther user experiences weaker small-scale fading. This possibility is accounted for in dynamic decoding order in terrestrial NOMA [129, 130], where the channel link quality is ranked based on the instantaneous received power of each user, which considers both large-scale path loss and small-scale fading of the terrestrial users.

In this work we consider a SIC decoding strategy with adaptive decoding order. We assume that channel state information (CSI) is available at the BS. Due to the strong LoS environment of the aerial link, we assume that the received signal power corresponding to the AUE is stronger than that of the active TUE for most of the time. Based on this assumption, we assume that the AUE is decoded first at the BS[5]. However, if the AUE cannot be decoded, then the BS tries to decode the TUE, and then the AUE. This additional decoding step accounts for the case, where the received power corresponding to the active TUE is greater than that of the AUE when the AUE is flying closer to the cell edge and the active TUE is located closer to the BS. A detailed description of the decoding events and the aforementioned extra decoding step of the proposed aerial-terrestrial NOMA scheme is presented below.

The tree diagram of the decoding events in the proposed NOMA scheme is illustrated in Fig. 2 and is explained as follows. The received signal at the BS is comprised of the superimposed Ψ_{A} and Ψ_{T}. The possible decoding events at the BS are discussed below.

- With SIC at the BS, Ψ_{A} is decoded first by treating Ψ_{T} as interference. If Ψ_{A} is decoded successfully, Ψ_{T} is decoded using SIC. This corresponds to

[5]We can also consider another decoding order case where the signal transmitted by the TUE is decoded first. The working principle of this case would be similar to the case where the signal transmitted by the AUE is decoded first. However, due to the nature of the proposed NOMA scheme, the decoding order has no effect on the system performance in terms of the metrics defined in Section 4.2. Thus, in this work, we only focus on the case where the signal transmitted by the AUE is decoded first.

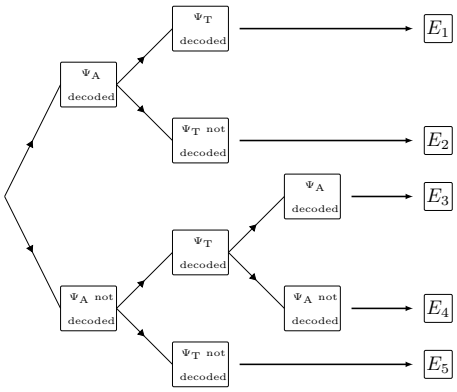

Figure 2.2: Tree diagram of decoding events for proposed NOMA scheme.

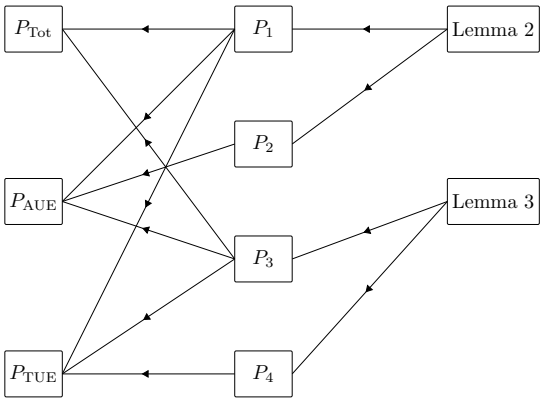

Figure 2.3: Summary of the analytical framework metrics.

decoding events E_1 or E_2, depending on the successful decoding of Ψ_{T}.

- If Ψ_{A} is not decoded successfully in the first step, then the BS tries to decode Ψ_{T} by considering Ψ_{A} as interference[6]. If Ψ_{T} is decoded successfully at this stage, BS tries to decode the previously unsuccessful Ψ_{A} using SIC. This corresponds to decoding events E_3 or E_4, depending on the successful decoding of the Ψ_{A} in the third decoding step.

- The last decoding event E_5 corresponds to the case where both Ψ_{A} and Ψ_{T} fail to decode.

Each branch of the probability tree in Fig. 2.2 corresponds to a joint decoding event where either/ both/ none of the signals are decoded. Events corresponding to each branch are defined as follows.

- E_1 : Event that Ψ_{A} (i.e., AUE) is decoded in the first step and Ψ_{T} (i.e., TUE) is decoded in the second step.

[6]In this work, we assume that, if Ψ_{A} is not decoded successfully, then error propagation occurs, i.e., BS treats the AUE's entire signal as interference when decoding Ψ_{T}. If Ψ_{A} is decoded successfully, due to availability of CSI at the BS, the error propagation factor is 0, i.e,. AUE's entire signal is subtracted from the superimposed signal [131]. In practical scenarios where channel estimation error is non-negligible, the error propagation factor is non zero and AUE's signal may not be perfectly reconstructed and completely subtracted from the superimposed signal at the BS. Due to additional interference caused by the imperfect reconstruction and subtraction of AUE's signal, the SINR of the TUE and associated probabilities may slightly decrease.

- E_2 : Event that Ψ_{A} is decoded in the first step and Ψ_{T} is not decoded in the second step.
- E_3 : Event that Ψ_{A} is not decoded in the first step, Ψ_{T} is decoded in the second step, and Ψ_{A} is decoded in the third step.
- E_4 : Event that Ψ_{A} is not decoded in the first step, Ψ_{T} is decoded in the second step, and Ψ_{A} is not decoded in the third step.
- E_5 : Event that Ψ_{A} is not decoded in the first step and Ψ_{T} is not decoded in the second step.

Remark 2.1 *Due to the extra decoding step (corresponding to events E_3 and E_4), the tree diagram in this work is different from the tree diagrams in prior studies in terrestrial NOMA [128, 132]. In addition, we take the dependency of individual decoding steps into account rather than making the assumption that the decoding steps are independent as done in [128].*

The probability corresponding to each event E_i is given by $P_i = \mathbb{P}(E_i)$, where $i = 1, 2, 3, 4$. These probabilities will be derived in Section 4.2 to characterize the system performance under the proposed NOMA scheme.

2.3 Analytical Framework

In this section, we analyze the performance of the system using the rate coverage probability as the performance metric.

Definition 2.1 *The rate coverage probability is the probability that the achievable data rate of a user exceeds the target data rate. It is defined as $\mathbb{P}(B\log_2(1+\mathrm{SINR}_\varrho) \geq \pi_\varrho)$, where $\varrho \in \{\mathrm{T}, \mathrm{A}\}$ denotes TUE and AUE, and B, SINR_ϱ and π_ϱ correspond to the bandwidth, signal-to-interference-plus-noise ratio and target data rate of the user, respectively.*

For analytical simplicity, we re-express the rate coverage probability as

$$P_{\mathrm{cov}} = \mathbb{P}[\mathrm{SINR}_\varrho \geq \theta_\varrho], \tag{2.6}$$

which is the complementary cumulative distribution function (CCDF) of SINR, where $\theta_{\varrho} = 2^{\frac{\pi_{\varrho}}{B}-1}$ is the target SINR threshold of the user. Note that we evaluate the rate coverage probability at each trajectory point of AUE, by averaging it over the location of the active TUE, and small-scale fading of AUE and TUE.

For each trajectory point, we evaluate the performance by computing three main rate coverage probabilities as defined below. The following probabilities correspond to linear combinations of probabilities of joint decoding events defined in Section 2.2.

- P_{Tot} : Rate coverage probability of the event where both AUE and TUE are decoded successfully and is given by $P_{\text{Tot}} = P_1 + P_3$.
- P_{AUE} : Rate coverage probability of the event where AUE is decoded successfully and is given by $P_{\text{AUE}} = P_1 + P_2 + P_3$.
- P_{TUE} : Rate coverage probability of the event where TUE is decoded successfully and is given by $P_{\text{TUE}} = P_1 + P_3 + P_4$.

The rest of this section presents the lemmas and propositions used in the derivation of P_{Tot}, P_{AUE} and P_{TUE}. The relationship between the main results is illustrated in Fig. 2.3.

First we present three Lemmas, which help to derive the main results in this Chapter.

Lemma 2.3.1 *The probability density function (PDF) of the 3D propagation distance d_T between BS and TUE is*

$$f_{d_T}(z) = \frac{2z}{R^2} \ , \ h_{BS} \leq z \leq \sqrt{R^2 + h_{BS}^2}. \tag{2.7}$$

Proof

See Appendix A.1.

Lemma 2.3.2 *The cumulative distribution function (CDF) and PDF of the received power ψ_T corresponding to the active TUE, assuming TUE fading channel is Rayleigh fading, are*

$$F_{\psi_T}(x) = 1 - \exp\left(\frac{-x}{\rho_T G_T}\right), \tag{2.8}$$

and

$$f_{\psi_T}(x) = \frac{1}{\rho_T G_T} \exp\left(\frac{-x}{\rho_T G_T}\right), \tag{2.9}$$

respectively, where $\psi_T = P_T {d_T}^{-\alpha_T} H_T G_T$.

Proof

See Appendix A.2.

Lemma 2.3.3 *The CDF and PDF of the received power* ψ_A *corresponding to the AUE are*

$$F_{\psi_A}(x) = 1 - \mathbb{P}_{LoS} \sum_{i=0}^{m_L-1} \frac{(\beta_L x)^i}{i!} \exp(-\beta_L x) - (1 - \mathbb{P}_{LoS}) \sum_{j=0}^{m_N-1} \frac{(\beta_N x)^j}{j!} \exp(-\beta_N x), \tag{2.10}$$

and

$$f_{\psi_A}(x) = \mathbb{P}_{LoS} \frac{\exp(-x\beta_L) {\beta_L}^{m_L} x^{m_L-1}}{\Gamma(m_L)} + (1 - \mathbb{P}_{LoS}) \frac{\exp(-x\beta_N) {\beta_N}^{m_N} x^{m_N-1}}{\Gamma(m_N)}, \tag{2.11}$$

respectively, where $\psi_A = P_A \zeta_A H_A G_A$, $\beta_L = \frac{m_L}{P_A \eta_L d_A^{-\alpha_L} G_A}$ *and* $\beta_N = \frac{m_N}{P_A \eta_N d_A^{-\alpha_N} G_A}$ *and,* m_L *and* m_N *correspond to the fading parameters for the LoS and NLoS aerial channels, respectively.*

Proof

See Appendix A.2.

Next, we derive the rate coverage probabilities of the joint decoding events defined in Section 2.2.

Proposition 2.1 *The rate coverage probability that AUE is decoded in the first step and TUE is decoded in the second step is*

$$P_1 = \frac{1}{\mu} \exp\left(\frac{\sigma^2}{\mu}\right) \left[\mathbb{P}_{LoS} \sum_{i=0}^{m_L-1} \frac{(\beta_L \theta_A)^i}{i!} \left(\beta_L \theta_A + \frac{1}{\mu}\right)^{-i-1} \Gamma\left(1+i, (1+\theta_T)\left(\beta_L \theta_A + \frac{1}{\mu}\right)\sigma^2\right) \right.$$

$$+ (1 - \mathbb{P}_{LoS}) \sum_{j=0}^{m_N - 1} \frac{(\beta_N \theta_A)^j}{i!} \left(\beta_N \theta_A + \frac{1}{\mu} \right)^{-j-1} \Gamma \left(1 + j, (1 + \theta_T) \left(\beta_N \theta_A + \frac{1}{\mu} \right) \sigma^2 \right) \Bigg], \tag{2.12}$$

where $\mu = \rho_T G_T$.

Proof

The proof relies on stochastic geometry and is presented in Appendix A.3.

Proposition 2.2 *The rate coverage probability that AUE is decoded in the first step and TUE is not decoded in the second step is*

$$P_2 = \frac{1}{\mu} \exp\left(\frac{\sigma^2}{\mu} \right) \Bigg[\mathbb{P}_{LoS} \sum_{i=0}^{m_L - 1} \frac{(\beta_L \theta_A)^i}{i!} \left(\beta_L \theta_A + \frac{1}{\mu} \right)^{-i-1} \Bigg[\Gamma \left(1 + i, \left(\beta_L \theta_A + \frac{1}{\mu} \right) \sigma^2 \right) - \Gamma \left(1 + i, (1 + \theta_T) \left(\beta_L \theta_A + \frac{1}{\mu} \right) \sigma^2 \right) \Bigg] + (1 - \mathbb{P}_{LoS}) \sum_{j=0}^{m_N - 1} \frac{(\beta_N \theta_A)^j}{j!} \left(\beta_N \theta_A + \frac{1}{\mu} \right)^{-j-1} \times \left[\Gamma \left(1 + j, \left(\beta_N \theta_A + \frac{1}{\mu} \right) \sigma^2 \right) - \Gamma \left(1 + j, (1 + \theta_T) \left(\beta_N \theta_A + \frac{1}{\mu} \right) \sigma^2 \right) \Bigg] \Bigg]. \tag{2.13}$$

Proof

The proof relies on stochastic geometry and is presented in Appendix A.3.

Proposition 2.3 *The rate coverage probability that AUE is not decoded in the first step, TUE is decoded in the second step, and AUE is decoded in the third step is*

$$P_3 = \begin{cases} \exp\left(\frac{-\theta_T \sigma^2}{\mu} \right) \Bigg[\frac{\mathbb{P}_{LoS}}{\Gamma(m_L)} \beta_L^{m_L} \left(\beta_L + \frac{\theta_T}{\mu} \right)^{-m_L} \Gamma \left(m_L, \theta_A \left(\beta_L + \frac{\theta_T}{\mu} \right) \sigma^2 \right) \\ \quad + \frac{1 - \mathbb{P}_{LoS}}{\Gamma(m_N)} \beta_N^{m_N} \left(\beta_N + \frac{\theta_T}{\mu} \right)^{-m_N} \Gamma \left(m_N, \theta_A \left(\beta_N + \frac{\theta_T}{\mu} \right) \sigma^2 \right) \Bigg], & \text{if } \theta_A \theta_T \geq 1 \\ \frac{\mathbb{P}_{LoS}}{\Gamma(m_L)} \exp\left(\frac{\sigma^2}{\mu} \right) {\beta_L}^{m_L} \left(\beta_L + \frac{1}{\theta_A \mu} \right)^{-m_L} \Gamma \left(m_L, \left(\beta_L \theta_A + \frac{1}{\mu} \right) \sigma^2 \right) \\ \quad + \frac{1 - \mathbb{P}_{LoS}}{\Gamma(m_N)} \exp\left(\frac{\sigma^2}{\mu} \right) {\beta_N}^{m_N} \left(\beta_N + \frac{1}{\theta_T \mu} \right)^{-m_N} \Gamma \left(m_N, \left(\beta_N \theta_A + \frac{1}{\mu} \right) \sigma^2 \right) \\ \quad - \frac{1}{2} \frac{\theta_A {\theta_T}^2 \sigma^4 (1 + \theta_A)^2}{(1 - \theta_A \theta_T)}, & \text{if } 0 \leq \theta_A \theta_T < 1. \end{cases} \tag{2.14}$$

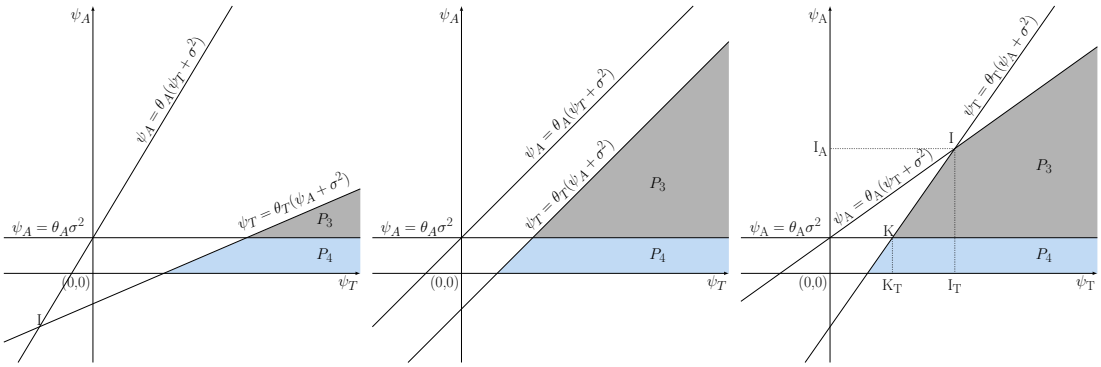

(a) $\theta_A\theta_T > 1$ (b) $\theta_A\theta_T = 1$ (c) $\theta_A\theta_T < 1$

Figure 2.4: Integral regions of P_3 and P_4, when $\theta_A\theta_T > 1$, $\theta_A\theta_T = 1$, and $\theta_A\theta_T < 1$, respectively, for proof of Propositions 2.3 and 2.4.

Proof

The rate coverage probability P_3 can be expressed as

$$\begin{aligned} P_3 &= \mathbb{P}_{\psi_A,\psi_T}\left(\frac{\psi_A}{\sigma^2} \geq \theta_A, \frac{\psi_T}{\psi_A+\sigma^2} \geq \theta_T, \frac{\psi_A}{\psi_T+\sigma^2} < \theta_A\right) \\ &= \mathbb{P}_{\psi_A,\psi_T}\left(\psi_A \geq \theta_A\sigma^2, \psi_T \geq \theta_T(\psi_A+\sigma^2), \psi_A < \theta_A(\psi_T+\sigma^2)\right). \end{aligned} \tag{2.15a}$$

The inequalities in (2.15a) are plotted in Fig. 2.4. P_3 is derived by calculating the area covered by all three curves. The point of intersection of $\psi_A = \theta_A(\psi_T + \sigma^2)$ and $\psi_T = \theta_T(\psi_A + \sigma^2)$ is given by $\mathrm{I} = \left(\frac{\theta_T\sigma^2(1+\theta_A)}{1-\theta_A\theta_T}, \frac{\theta_A\sigma^2(1+\theta_T)}{1-\theta_A\theta_T}\right)$. Depending on the value of $\theta_A\theta_T$, the point of intersection, I can be located in different quadrants or non-existent (in the case of $\theta_A\theta_T = 1$). Thus, P_3 can have different values in these cases.

We first present the proof of P_3 when $\theta_A\theta_T \geq 1$.

$$P_3 = \mathbb{P}_{\psi_A,\psi_T}\left(\psi_T \geq \theta_T(\psi_A+\sigma^2), \psi_A \geq \theta_A\sigma^2\right) \tag{2.16a}$$

$$= \mathbb{E}_{\psi_A}\left[\mathbb{P}_{\psi_T}\left(\psi_T \geq \theta_T(a+\sigma^2), a \geq \theta_A\sigma^2\right)\right]$$

$$= \int_{\theta_A\sigma^2}^{\infty} \mathbb{P}_{\psi_T}\left(\psi_T \geq \theta_T(a+\sigma^2)\right) f_{\psi_A}(a)da \tag{2.16b}$$

$$= \int_{\theta_A\sigma^2}^{\infty} \mathbb{P}_{H_T,d_T}\left(H_T \geq \frac{\psi_T(a+\sigma^2)}{P_T {d_T}^{-\alpha_T} G_T}\right) f_{\psi_A}(a)da$$

$$= \int_{\theta_A\sigma^2}^{\infty} \mathbb{E}_{d_T}\left[\exp\left(-\frac{\theta_T(a+\sigma^2)}{P_T {d_T}^{-\alpha_T} G_T}\right)\right] f_{\psi_A}(a)da \tag{2.16c}$$

$$= \int_{\theta_{\rm A}\sigma^2}^{\infty} \left[\int_{h_{\rm BS}}^{\sqrt{{h_{\rm BS}}^2+R^2}} \exp\left(-\frac{\theta_{\rm T}(a+\sigma^2)}{\rho_{\rm T} z^{\alpha_{\rm T}} z^{-\alpha_{\rm T}} G_{\rm T}} \right) \left(\frac{2z}{R^2} \right) dz \right] f_{\psi_{\rm A}}(a) da$$

$$= \int_{\theta_{\rm A}\sigma^2}^{\infty} \exp\left(\frac{-\theta_{\rm T}(a+\sigma^2)}{\rho_{\rm T} G_{\rm T}} \right) \Big[\mathbb{P}_{\rm LoS} \frac{\exp(-a\beta_{\rm L}) {\beta_{\rm L}}^{m_{\rm L}} a^{m_{\rm L}-1}}{\Gamma(m_{\rm L})}$$

$$+ (1-\mathbb{P}_{\rm LoS}) \frac{\exp(-a\beta_{\rm N}) {\beta_{\rm N}}^{m_{\rm N}} a^{m_{\rm N}-1}}{\Gamma(m_{\rm N})} \Big] da, \tag{2.16d}$$

where (2.16a) is the simplified expression for the area of P_3 based on Fig. 2.4(a) and 2.4(b). (2.16c) comes from the fact that $H_{\rm T}$ follows an exponential distribution. Integration of (2.16d) with respect to a and substitution of $\mu = \rho_{\rm T} G_{\rm T}$ into (2.16d) yield (2.14) for the case $\theta_{\rm A}\theta_{\rm T} \geq 1$.

The proof of P_3 for the case $\theta_{\rm A}\theta_{\rm T} < 1$ is presented as follows. Let ${\rm I} = ({\rm I_T}, {\rm I_A})$, where $\rm I_T$ denotes the x-coordinate and $\rm I_A$ denotes the y-coordinate of point I, and, ${\rm K_T} = \theta_{\rm T}\sigma^2(\theta_{\rm A}+1)$ is the x-coordinate of point K as illustrated in Fig. 2.4(c). Let $P_{3,Q}$ be the triangular area enclosed by the curves, $\psi_{\rm T} = \theta_{\rm T}(\psi_{\rm A}+\sigma^2)$, $\psi_{\rm A} = \theta_{\rm A}\sigma^2$ and $\psi_{\rm T} = {\rm I_T}$. Let $P_{3,R}$ be the quadrilateral area enclosed by the curves, $\psi_{\rm A} = \theta_{\rm A}(\psi_{\rm T}+\sigma^2)$, $\psi_{\rm A} = \theta_{\rm A}\sigma^2$ and $\psi_{\rm T} = {\rm I_T}$. Thus, we can write $P_3 = P_{3,Q} + P_{3,R}$. The derivations of $P_{3,Q}$ and $P_{3,R}$ are presented below.

$$P_{3,Q} = \frac{1}{2}({\rm I_T} - {\rm K_T})({\rm I_A} - \theta_{\rm A}\sigma^2) = \frac{1}{2} \frac{\theta_{\rm A}{\theta_{\rm T}}^2\sigma^2(1+\theta_{\rm A})}{(1-\theta_{\rm A}\theta_{\rm T})} \frac{\theta_{\rm A}\theta_{\rm T}\sigma^2(1+\theta_{\rm A})}{(1-\theta_{\rm A}\theta_{\rm T})} \tag{2.17a}$$

$$= \frac{1}{2} \frac{{\theta_{\rm A}}^2{\theta_{\rm T}}^3\sigma^4(1+\theta_{\rm A})^2}{(1-\theta_{\rm A}\theta_{\rm T})^2}, \tag{2.17b}$$

where (2.17a) is the area of a triangle.

$$P_{3,R} = \mathbb{P}_{\psi_{\rm A},\psi_{\rm T}} \left(\psi_{\rm A} < \theta_{\rm A}(\psi_{\rm T}+\sigma^2), \psi_{\rm A} \geq \theta_{\rm A}\sigma^2 \right) - \frac{1}{2}{\rm I_T}({\rm I_A} - \theta_{\rm A}\sigma^2) \tag{2.18a}$$

$$= \mathbb{E}_{\psi_{\rm A}} \left[\mathbb{P}_{\psi_{\rm T}} \left(\psi_{\rm T} > \frac{a}{\theta_{\rm A}} - \sigma^2, a \geq \theta_{\rm A}\sigma^2 \right) \right] - \frac{1}{2} \frac{\theta_{\rm A}{\theta_{\rm T}}^2\sigma^4(1+\theta_{\rm A})^2}{(1-\theta_{\rm A}\theta_{\rm T})^2}$$

$$= \int_{\theta_{\rm A}\sigma^2}^{\infty} \mathbb{P}_{\psi_{\rm T}} \left(\psi_{\rm T} > \frac{a}{\theta_{\rm A}} - \sigma^2 \right) f_{\psi_{\rm A}}(a) da - \frac{1}{2} \frac{\theta_{\rm A}{\theta_{\rm T}}^2\sigma^4(1+\theta_{\rm A})^2}{(1-\theta_{\rm A}\theta_{\rm T})^2}$$

$$= \int_{\theta_{\rm A}\sigma^2}^{\infty} \exp\left(-\frac{(\frac{a}{\theta_{\rm A}} - \sigma^2)}{\rho_{\rm T} G_{\rm T}} \right) f_{\psi_{\rm A}}(a) da - \frac{1}{2} \frac{\theta_{\rm A}{\theta_{\rm T}}^2\sigma^4(1+\theta_{\rm A})^2}{(1-\theta_{\rm A}\theta_{\rm T})^2}, \tag{2.18b}$$

where (2.18a) is the difference between the triangular area enclosed by $\psi_{\mathrm{A}} = \theta_{\mathrm{A}}(\psi_{\mathrm{T}}+\sigma^2)$ and $\psi_{\mathrm{A}} = \theta_{\mathrm{A}}\sigma^2$, and the triangular area enclosed by $\psi_{\mathrm{A}} = \theta_{\mathrm{A}}(\psi_{\mathrm{T}}+\sigma^2)$, $\psi_{\mathrm{A}} = \theta_{\mathrm{A}}\sigma^2$ and $\psi_{\mathrm{T}} = \mathrm{I}_{\mathrm{T}}$. Evaluating and simplifying (2.18b), we obtain (2.14).

Proposition 2.4 *The rate coverage probability that AUE is not decoded in the first step, TUE is decoded in the second step, and AUE is not decoded in the third step is*

$$P_4 = \exp\left(\frac{-\theta_T\sigma^2}{\mu}\right)\left[\frac{\mathbb{P}_{LoS}}{\Gamma(m_L)}\beta_L^{m_L}\left(\beta_L+\frac{\theta_T}{\mu}\right)^{-m_L}\left[\Gamma(m_L)-\Gamma\left(m_L,\theta_A\left(\beta_L+\frac{\theta_T}{\mu}\right)\sigma^2\right)\right]\right.$$
$$\left.+\frac{1-\mathbb{P}_{LoS}}{\Gamma(m_N)}\beta_N^{m_N}\left(\beta_N+\frac{\theta_T}{\mu}\right)^{-m_N}\left[\Gamma(m_N)-\Gamma\left(m_N,\theta_A\left(\beta_N+\frac{\theta_T}{\mu}\right)\sigma^2\right)\right]\right]. \tag{2.19}$$

Proof

The rate coverage probability P_4 can be expressed as

$$P_4 = \mathbb{P}_{\psi_{\mathrm{A}},\psi_{\mathrm{T}}}\left(\frac{\psi_{\mathrm{A}}}{\sigma^2}<\theta_{\mathrm{A}},\frac{\psi_{\mathrm{T}}}{\psi_{\mathrm{A}}+\sigma^2}\geq\theta_{\mathrm{T}},\frac{\psi_{\mathrm{A}}}{\psi_{\mathrm{T}}+\sigma^2}<\theta_{\mathrm{A}}\right)$$
$$= \mathbb{P}_{\psi_{\mathrm{A}},\psi_{\mathrm{T}}}\left(\psi_{\mathrm{A}}<\theta_{\mathrm{A}}\sigma^2,\psi_{\mathrm{T}}\geq\theta_{\mathrm{T}}(\psi_{\mathrm{A}}+\sigma^2),\psi_{\mathrm{A}}<\theta_{\mathrm{A}}(\psi_{\mathrm{T}}+\sigma^2)\right) \tag{2.20a}$$
$$= \mathbb{P}_{\psi_{\mathrm{A}},\psi_{\mathrm{T}}}\left(\psi_{\mathrm{A}}<\theta_{\mathrm{A}}\sigma^2,\psi_{\mathrm{T}}\geq\theta_{\mathrm{T}}(\psi_{\mathrm{A}}+\sigma^2)\right) = \mathbb{E}_{\psi_{\mathrm{A}}}\left[\mathbb{P}_{\psi_{\mathrm{T}}}\left(a<\theta_{\mathrm{A}}\sigma^2,\psi_{\mathrm{T}}\geq\theta_{\mathrm{T}}(a+\sigma^2)\right)\right] \tag{2.20b}$$
$$= \int_0^{\theta_{\mathrm{A}}\sigma^2}\mathbb{P}_{\psi_{\mathrm{T}}}\left(\psi_{\mathrm{T}}\geq\theta_{\mathrm{T}}(a+\sigma^2)\right)f_{\psi_{\mathrm{A}}}(a)da$$
$$= \int_0^{\theta_{\mathrm{A}}\sigma^2}\exp\left(-\frac{\theta_{\mathrm{T}}(a+\sigma^2)}{\rho_{\mathrm{T}}G_{\mathrm{T}}}\right)f_{\psi_{\mathrm{A}}}(a)da. \tag{2.20c}$$

The inequalities in (2.20a) are plotted in Fig. 2.4. Note that the areas enclosed by the relevant curves do not vary with the value of $\theta_{\mathrm{A}}\theta_{\mathrm{T}}$. (2.20b) is the simplified expression for the quadrilateral area of P_4. In (2.20c), the evaluation of $\mathbb{P}_{\psi_{\mathrm{T}}}\left(\psi_{\mathrm{T}}\geq\theta_{\mathrm{A}}(a+\sigma^2)\right)$ is similar to that in (2.16b). By integrating (2.20c) with respect to a, we obtain (2.19).

The final rate coverage probabilities P_{Tot}, P_{AUE} and P_{TUE} can be computed after evaluating P_1, P_2, P_3 and P_4, as summarized in Fig. 2.3.

The following remark discusses an important insight related to the rate coverage probability expressions.

Remark 2.2 *As the distance between the AUE and the BS increases, probabilities P_1 and P_2 decrease while probabilities P_3 and P_4 increase. This is due to the deteriorating LoS conditions and increasing path loss for the A2C channel. Overall, P_1 has the dominating impact and thus the different rate coverage probabilities decrease as the distance between the AUE and the BS increases.*

2.4 Numerical Results

In this section, we investigate the performance of the proposed NOMA scheme with respect to the AUE SINR threshold, TUE SINR threshold and AUE altitude. The analytical expressions in Propositions 2.1, 2.2, 2.3, and 2.4 involve Gamma functions and/or finite sums only and are easily evaluated using Mathematica. The accuracy of the derived analytical expressions is validated by comparing them with simulation results. The simulation results are obtained using system level computer simulations in Matlab based on the exact system scenario by averaging over 10^6 Monte Carlo simulation runs. The parameter values used for the results are given in Table 4.1. The chosen values are consistent with other relevant works in the literature [10,49,126]. We assume a bandwidth of 10 MHz and consider AUE target SINR thresholds $\{0, 10, 20, 30, 40\}$ dB, corresponding to AUE target rates $\{10, 34.6, 66.6, 99.7, 134.6\}$ Mbps. Note that 0 dB and above can satisfy command and control transmissions, 10 dB and above can satisfy 4K HD video, and 20 dB and above can satisfy 8K HD video [133]. We consider a target rate of 10 Mbps (corresponding to a target SINR threshold of 0 dB) for the TUE, unless stated otherwise.

2.4.1 Probabilistic LoS model

We adopt the probabilistic LoS model suggested in ITU recommendation report [134] by considering AUE as the transmitter and the terrestrial BS as the receiver.

Table 2.1: Parameter values for numerical and simulation results.

Parameter	Symbol	Value	Parameter	Symbol	Value
Cell radius	R	500 m	Number of rounds	m	3
Height of BS	h_{BS}	30 m	Time period for AUE's transmission	T_{A}	30 s
Noise power	σ^2	-100 dBm	AUE's transmit power	P_{A}	0.1 W
TUE			AUE's antenna gain	G_{A}	1
TUE's cutoff threshold	ρ_{T}	-75 dBm	Pathloss exponent for LoS link	α_{L}	2.2
TUE's antenna gain	G_{T}	1	Pathloss exponent for NLoS link	α_{N}	3.5
Pathloss exponent of terrestrial link	α_{T}	3.5	Attenuation for LoS link	η_{L}	0 dB
AUE			Attenuation for NLoS link	η_{N}	13 dB
AUE's speed	v_{A}	15 m/s	Fading parameter for LoS link	m_{L}	5
AUE's altitude	h_{A}	25 m, 120 m	Fading parameter for NLoS link	m_{N}	1

Thus, the probability of LoS between the AUE and the terrestrial BS is [135]

$$\mathbb{P}_{\mathrm{LoS}} = \prod_{n_{\mathrm{ITU}}=0}^{m_{\mathrm{ITU}}} \left[1 - \exp\left(- \frac{\left[h_{\mathrm{A}} - \frac{\left(n_{\mathrm{ITU}}+\frac{1}{2}\right)(h_{\mathrm{A}}-h_{\mathrm{BS}})}{m_{\mathrm{ITU}}+1} \right]^2}{2\delta_{\mathrm{ITU}}} \right) \right], \tag{2.21}$$

where $m_{\mathrm{ITU}} = \left\lfloor \left(\frac{r_{\mathrm{A}}\sqrt{\alpha_{\mathrm{ITU}}\beta_{\mathrm{ITU}}}}{1000} - 1 \right) \right\rfloor$ and $\lfloor \cdot \rfloor$ is the floor function. α_{ITU}, β_{ITU} and δ_{ITU} correspond to the environment-related parameters that can be used to describe the built-up area. α_{ITU} and β_{ITU} correspond to the ratio of land area covered by buildings to total land area, and the average number of buildings per unit area, respectively. δ_{ITU} is the parameter for the Rayleigh distribution that determines the building heights. The values of these parameters for suburban, urban, dense urban and urban high-rise environments are given in Table I in [136].

Insights: Fig. 2.5 illustrates the probabilistic LoS behavior for two different AUE altitudes. Fig. 2.5(a) demonstrates the variation of LoS probability with the horizontal distance of AUE from the BS, whereas Fig. 2.5(b) shows the variation of the LoS probability with angle of elevation between the AUE and BS. Note that both plots exhibit step-wise discrete behavior due to the blockage caused by buildings in the urban built-up area. This behavior becomes smooth and continuous at very high AUE altitudes. However, in this work, we consider a practical AUE altitude range of $25 - 300$ m.

2.4.2 AUE Trajectory Model

For the purpose of generating the results, we model the trajectory of AUE using an Archimedes' spiral. The Archimedes' spiral has a special property that any ray

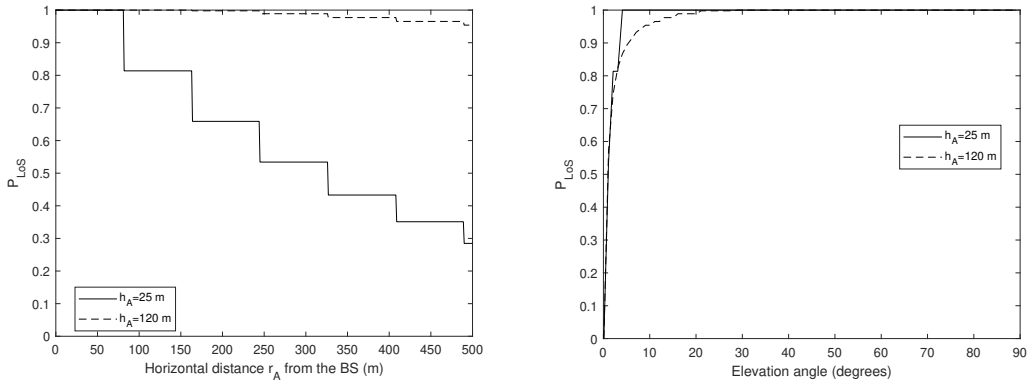

(a) (b)

Figure 2.5: Probability of line-of-sight, $\mathbb{P}_{\text{LoS}}$ versus (a) horizontal distance from the BS r_{A} (m), and (b) elevation angle between the AUE and BS. The adopted values for the environmental parameters corresponding to the urban built-up area are, $\alpha_{\text{ITU}} = 0.3$, $\beta_{\text{ITU}} = 500$ and $\delta_{\text{ITU}} = 15$.

from the origin intersects successive turnings of the spiral in points with a constant separation distance. Hence, it is a suitable trajectory for monitoring or surveillance in a disk region. *Note that the proposed framework in this Chapter is valid for any trajectory model.* In Sections 4.3 C-E we consider the Archimedes' spiral trajectory and in Section 2.4.6 we consider the 3GPP trajectory model.

The AUE starts its spiral trajectory at the center of the cell at a height h_{A}. The trajectory of the AUE can be described by a spiral with equation $r_{\text{A}} = \frac{R}{2\pi m}\phi_{\text{A}}$, where m is the number of rounds and ϕ_{A} is the orientation of AUE in the azimuth plane, measured with respect to the +x-axis. The equation for r_{A} is derived based on the assumption that the spiral starts at the center of the cell and reaches the cell edge at $\phi_{\text{AEdge}} = 2\pi m$ which is the maximum angle in the azimuth plane for a given number of rounds. Hence, the expressions for N and $r_{\text{A},n}$ for the Archimedes' spiral are given as follows:

The number of transmission points along the AUE trajectory defined by the Archimedes' spiral is given by

$$N = \left\lfloor \frac{R\left(2\pi m\sqrt{1+(2\pi m)^2} + \sinh^{-1}(2\pi m)\right)}{4\pi m v_{\text{A}} T_{\text{A}}} \right\rfloor. \tag{2.22}$$

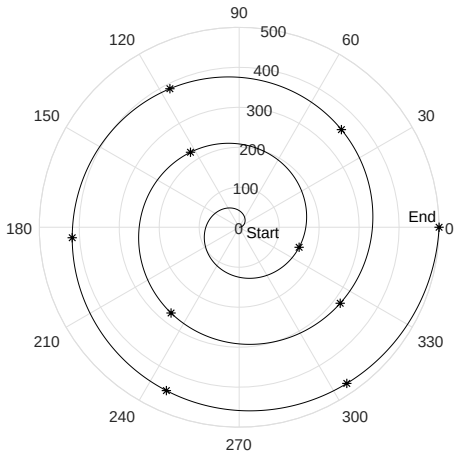

Figure 2.6: Archimedes' spiral trajectory with $m = 3$ and $R = 500$ m. AUE's transmission points are denoted by asterisk ($v_{\mathrm{A}} = 15$ m/s, $T_{\mathrm{A}} = 30$ s).

The horizontal distance $r_{\mathrm{A},n}$ between the AUE and BS at the nth transmission point is

$$r_{\mathrm{A},n} = R\sqrt{\frac{n}{N}}, \tag{2.23}$$

where $n = 1, \ldots, N$.

Fig. 2.6 demonstrates the Archimedes' trajectory for the case where the AUE travels three complete rounds to reach the cell edge. The AUE performs uplink transmission at 10 points along the trajectory, and the final transmission point lies at the cell edge.

2.4.3 Model Validation

Fig. 2.7 presents the total rate coverage probability P_{Tot} for an aerial-terrestrial network where the AUE flies according to an Archimedes' trajectory at a fixed height h_{A} along the entire trajectory. The model validation results are presented only for P_{Tot}, since P_{AUE} and P_{TUE} exhibit similar trends as that for P_{Tot}. We present the results when $\theta_{\mathrm{T}} = 0$ dB and AUE flies at altitudes 25 m and 120 m in an urban built-up area with the ITU probabilistic LoS model. We can see that the analytical results match well with the simulation results. This validates the accuracy of the analytical framework in Section 4.2.

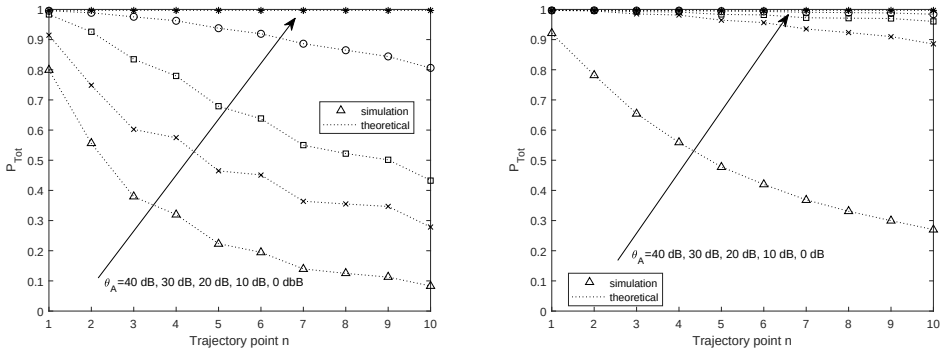

(a) P_{Tot} at h_{A}=25 m (b) P_{Tot} at h_{A}=120 m

Figure 2.7: Rate coverage probabilities of the events where both AUE and TUE are decoded (P_{Tot}) for (a) $h_{\text{A}} = 25$ m and (b) $h_{\text{A}} = 120$ m. The simulation values and the theoretical values are represented by markers and dotted lines, respectively.

Insights: Fig. 2.7 shows that P_{Tot} generally decreases when AUE's SINR threshold (corresponding to AUE's target data rate) increases and when the horizontal distance between the AUE and the BS increases. This is because it becomes harder for the BS to decode the AUE signal in the first step, which has a dominant impact on the system performance. This is in accordance with earlier Remark 2. We can see that the performance is better at 120 m compared to that at 25 m. This is due to the fact that in the ITU probabilistic LoS model, as illustrated in Fig. 2.5(a), the probability of LoS is higher at higher AUE height.

In the next two subsections, we only present the numerical results using the proposed analytical framework due to the accuracy of our analytical results.

2.4.4 Impact of SINR Thresholds of TUE and AUE

Fig. 2.8 shows the impact of θ_{T} (equivalently, the target data rate of TUE), on rate coverage probabilities P_{Tot}, P_{AUE} and P_{TUE} for different θ_{A} values along the spiral trajectory. The results are presented for two different AUE heights (25 m and 120 m) in the urban built-up environment. $n = 1$ corresponds to the first transmission point and $n = 10$ corresponds to the last transmission point when the AUE reaches the cell edge (see transmission points marked in Fig. 2.6).

Insights: Fig. 2.8 shows that, depending upon the SINR thresholds θ_{T} and θ_{A}, P_{Tot} can be dominated by either decoding of TUE or AUE. Generally, for lower θ_{T}

value and a higher θ_{A} value, P_{Tot} is dominated by the decoding of AUE when the AUE is flying closer to the cell edge at a lower height. However, at a relatively higher θ_{T} value and low to moderate θ_{A} value, P_{Tot} is dominated by the decoding of the TUE. This is explained by comparing the subfigure results as follows.

Fig. 2.8(a) and 2.8(c) compare the rate coverage probabilities at $\theta_{\mathrm{T}} = 0$ dB for $h_{\mathrm{A}} = 25$ m and 120 m. For both heights, we can see that P_{Tot}, P_{AUE} and P_{TUE} have similar rate coverage probability values for lower θ_{A} values ($0 - 20$ dB). However, this trend changes at $\theta_{\mathrm{A}} = 30$ dB and 40 dB. When AUE is flying at 25 m (see Fig. 2.8(a)) and is closer to the cell edge, P_{TUE} is slightly higher than P_{Tot} and P_{AUE} at $\theta_{\mathrm{A}} = 30, 40$ dB. This is caused by the high path loss and poor LoS aerial links in proximity to the cell edge. *In this case, P_{Tot} is dominated by the decoding of AUE.* However, this behavior becomes less prominent at higher AUE heights (see Fig. 2.8(c)). This is because at higher AUE heights, the AUE is almost always guaranteed to be successfully decoded due to the strong LoS aerial links.

Fig. 2.8(b) and 2.8(d) compare the rate coverage probabilities at $\theta_{\mathrm{T}} = 10$ dB for $h_{\mathrm{A}} = 25$ and 120 m. For both heights, P_{Tot} is similar to P_{TUE} for low to moderate θ_{A} values (0, 10, 20, 30 dB). This implies that P_{Tot} *is dominated by the decoding of TUE* at higher θ_{T} for low to moderate θ_{A}. In Fig. 2.8(b), we can see that this effect becomes insignificant when θ_{A} is higher and AUE is flying at a relatively low height. It is important to note that this behavior in Fig. 2.8(b) is consistent throughout the trajectory at a higher θ_{T}, unlike in Fig. 2.8(a), where the trend changes as the AUE moves from cell center to cell edge. At 120 m, due to the strong LoS aerial links, P_{Tot} is dominated by the decoding of TUE for all considered θ_{A} values throughout the trajectory at higher θ_{T} values (see Fig. 2.8(d)).

Note that the trends of P_{AUE} and P_{TUE} are similar to that of P_{Tot} for each of the cases presented in Fig. 2.8. Thus, for the rest of the results section, we only present the corresponding results for P_{Tot}.

2.4.5 Impact of AUE Altitude and Built-Up Environments

Previously, we assumed that the AUE flies at a constant height in a spiral trajectory. Now we consider the case where the AUE still follows the spiral trajectory, but it can ascend or descend at each trajectory point to achieve a certain quality of service

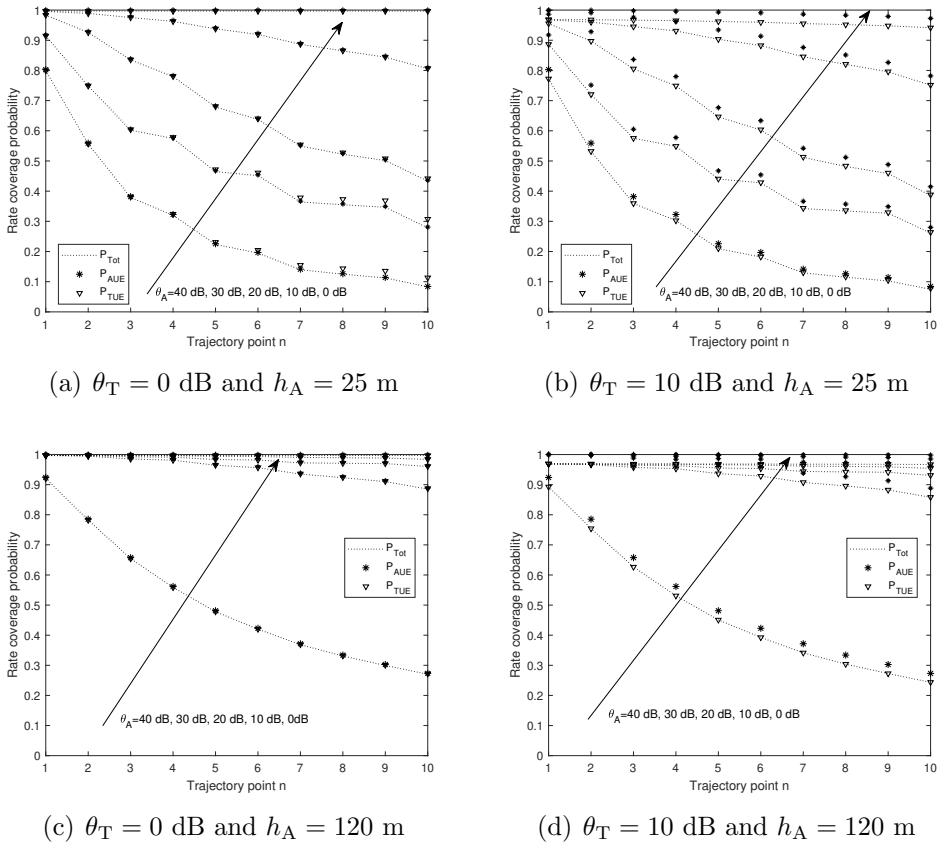

(a) $\theta_{\mathrm{T}} = 0$ dB and $h_{\mathrm{A}} = 25$ m

(b) $\theta_{\mathrm{T}} = 10$ dB and $h_{\mathrm{A}} = 25$ m

(c) $\theta_{\mathrm{T}} = 0$ dB and $h_{\mathrm{A}} = 120$ m

(d) $\theta_{\mathrm{T}} = 10$ dB and $h_{\mathrm{A}} = 120$ m

Figure 2.8: Rate coverage probabilities P_{Tot}, P_{AUE} and P_{TUE} vs. trajectory point n for different $\theta_{\mathrm{A}} = 0$, 10, 20, 30, 40 dB and, (a) $\theta_{\mathrm{T}} = 0$ dB and $h_{\mathrm{A}} = 25$ m, (b) $\theta_{\mathrm{T}} = 10$ dB and $h_{\mathrm{A}} = 25$ m, (c) $\theta_{\mathrm{T}} = 0$ dB and $h_{\mathrm{A}} = 120$ m and (d) $\theta_{\mathrm{T}} = 10$ dB and $h_{\mathrm{A}} = 120$ m. P_{Tot}, P_{AUE} and P_{TUE} are denoted by solid line, asterisk and circle, respectively.

(QoS).

We define the QoS as the probability where both AUE and TUE are decoded, which is equivalent to P_{Tot}. Current regulations in most countries do not permit AUEs to fly higher than a certain height [10, 14]. Hence, in this section, we focus on the minimum height of AUE at each trajectory point, to achieve a QoS of 90% (corresponds to $P_{\mathrm{Tot}} = 0.9$) for different built-up environments.

Insights: Fig. 2.9 plots P_{Tot} versus the minimum height to meet QoS constraint for different environments. From Fig. 2.9(a) for the suburban environment, we can see that due to the lower building density and shorter building height, a QoS of 90% can be achieved by the AUE even if it is flying at a very low height of 25

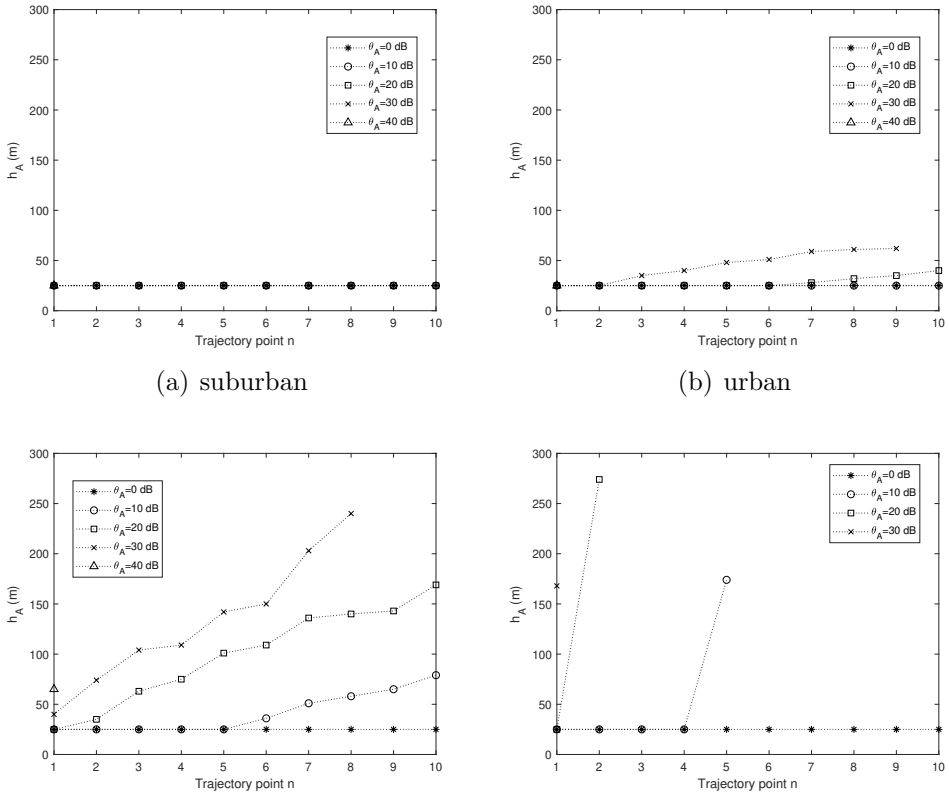

(a) suburban (b) urban

(c) dense urban (d) urban high-rise

Figure 2.9: Minimum height of AUE to achieve a total rate coverage probability of 0.9 vs. the trajectory point for (a) suburban, (b) urban, (c) dense urban and (d) urban high-rise environments. The severity of the environmental parameters increases in the order of suburban, urban, dense urban and urban high-rise built-up environments.

m. However, for the rest of the environments (see Fig. 2.9(b), 2.9(c) and 2.9(d)), the AUE needs to ascend when AUE flying towards the cell edge, in order to meet the QoS requirement. Moreover, this minimum height increases when the environmental parameters become severe. For an instance, for urban high-rise environment (see Fig. 2.9(d)), where there is a high density of taller buildings, a target QoS of 90% cannot be achieved for higher θ_{A} and r_{A} values even if the AUE is flying at a height of 300 m. Moreover, the target QoS at $\theta_{\mathrm{A}} = 40$ dB can only be satisfied at the first trajectory point (closer to the BS) for urban and dense urban built-up environments, and can not be satisfied at all for urban high-rise environment. This insight is summarized in the remark below.

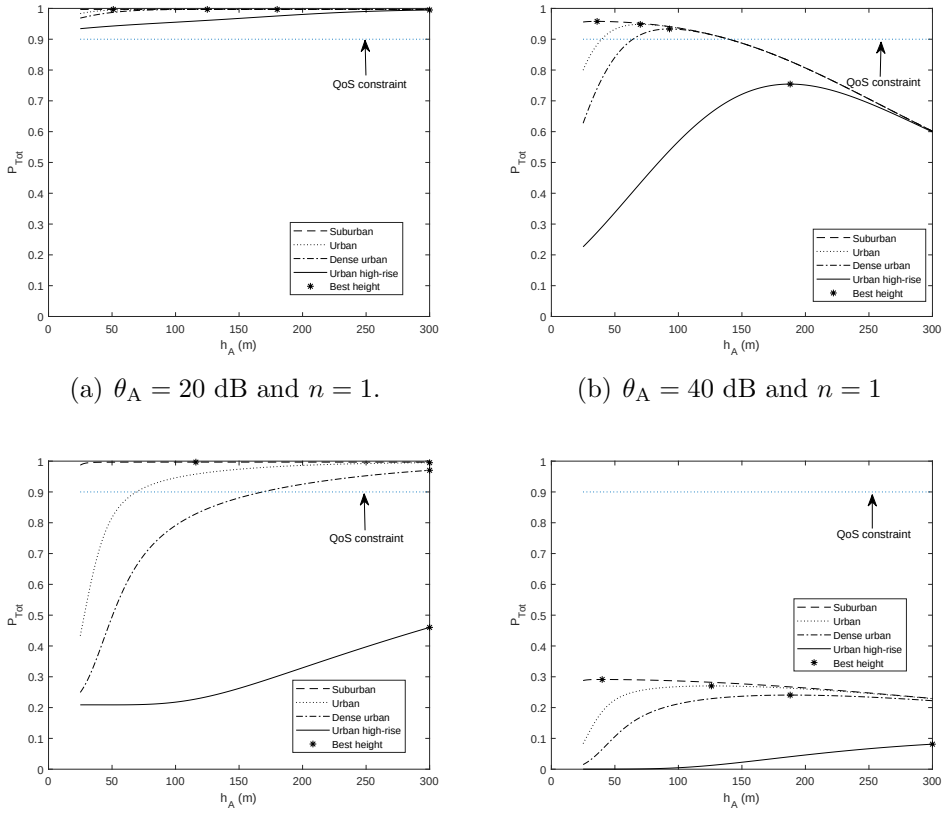

(a) $\theta_{\mathrm{A}} = 20$ dB and $n = 1$.

(b) $\theta_{\mathrm{A}} = 40$ dB and $n = 1$

(c) $\theta_{\mathrm{A}} = 20$ dB and $n = 10$

(d) $\theta_{\mathrm{A}} = 40$ dB and $n = 10$

Figure 2.10: Total rate coverage probability vs. AUE height h_{A} for different environments for (a) $\theta_{\mathrm{A}} = 20$ dB and $n = 1$, (b) $\theta_{\mathrm{A}} = 40$ dB and $n = 1$, (c) $\theta_{\mathrm{A}} = 20$ dB and $n = 10$ and (d) $\theta_{\mathrm{A}} = 40$ dB and $n = 10$. The best AUE height where P_{Tot} is maximum is indicated by markers. Dotted line correspond to a P_{Tot} threshold of 0.9.

Remark 2.3 *As the AUE moves away from the BS along its trajectory and as the severity of environmental parameters increases, the minimum AUE height to meet a QoS constraint of* 90% *increases.*

Since the first ($n = 1$) and last ($n = 10$) trajectory points represent the best and worst cases for the spiral trajectory, we also look at the variation of P_{Tot} with respect to the height of AUE at these trajectory points. We compare the P_{Tot} for two different TUE SINR threshold values at $n = 1$ and $n = 10$ (see Fig. 2.10). At $\theta_{\mathrm{A}} = 20$ dB (see Fig. 2.10(a) and 2.10(c)), P_{Tot} increases as the AUE height increases at both trajectory points. However, at $\theta_{\mathrm{A}} = 40$ dB (see Fig. 2.10(b)

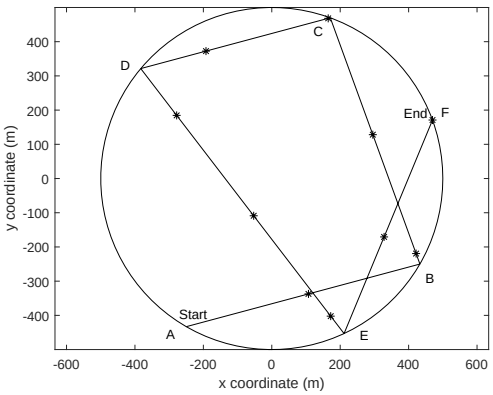

Figure 2.11: 3GPP-inspired trajectory model.

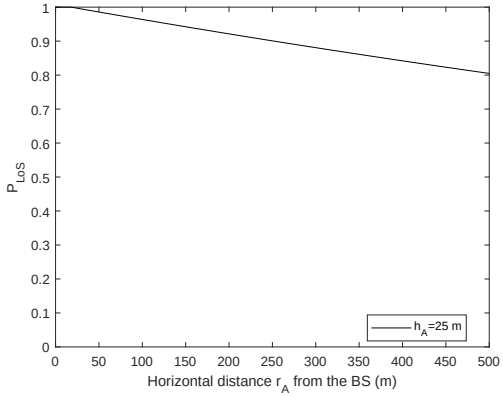

Figure 2.12: 3GPP probabilistic LoS model.

and 2.10(d)), there is a best height where the P_{Tot} is maximized. This trend is prominent when the AUE is closer to the BS (see Fig. 2.10(b)), and becomes less significant when AUE is closer to the cell boundary (see Fig. 2.10(d)). Moreover, the best height increases as the environmental conditions become severer for both trajectory points. Note that for $\theta_{\text{A}} = 20$ dB, the best height satisfies the QoS constraint of $P_{\text{Tot}} = 0.9$, except for urban high-rise at $n = 10$. For $\theta_{\text{A}} = 40$ dB, the best height satisfies the QoS constraint only for some environments at cell center ($n = 1$) and none of the environments at cell edge ($n = 10$). This insight is summarized in the remark below.

Remark 2.4 *As the AUE moves away from the BS along its trajectory, while having a higher target data rate, there is a best height where the total rate coverage probability is maximized, and this best height increases as the severity of the environmental parameters increases.*

Next, we apply the proposed NOMA scheme to a straight line AUE trajectory model adapted from the UAV trajectory model used in 3GPP study in [49].

2.4.6 3GPP Probabilistic LoS and Trajectory Models

We adopt the trajectory model and probabilistic LoS model proposed in Section A.2.2 of [49] for this evaluation. In 3GPP probabilistic LoS model, the probability of LoS between the AUE and the terrestrial BS, in the urban environment where

the BS antennas are positioned above the rooftop levels of buildings is [49]

$$\mathbb{P}_{LoS} = \begin{cases} \frac{d_1}{r_{\mathrm{A}}} + \exp\left(\frac{-r_{\mathrm{A}}}{p_1}\right)\left(1 - \frac{d_1}{r_{\mathrm{A}}}\right), & \text{if } r_{\mathrm{A}} > d_1, 22.5 < h_{\mathrm{A}} \leq 100 \\ 1, & \text{if } r_{\mathrm{A}} \leq d_1, 22.5 < h_{\mathrm{A}} \leq 100 \\ 1, & \text{if } 100 < h_{\mathrm{A}} \leq 300, \end{cases} \tag{2.24}$$

where $d_1 = \max(294.05 \log_{10}(h_{\mathrm{A}}) - 432.94, 18)$ and $p_1 = 233.98 \log_{10}(h_{\mathrm{A}}) - 0.95$. The probability of LoS at $h_{\mathrm{A}} = 25$ m is illustrated in Fig. 2.12. Compared with ITU LoS probability for the same height from Fig. 2.5(a), we can see that the LoS probability is very favorable even at low height of AUE.

The trajectory model for this scenario is defined as follows. The AUE starts its trajectory at a random initial location at the cell edge. Then, it moves at a randomly selected orientation in a straight line until it reaches the cell edge. Once it reaches the cell border, it picks another random orientation and moves in a straight line, and this process is continued until the AUE reaches its final trajectory point. An example realization, used for the purposed of generating results, is shown in Fig. 2.11. We consider AUE moves along multiple chords in the cellular cell, where A, B, C, D, E, and F correspond to the points at the cell edge where AUE changes the orientation of the trajectory. We consider that AUE transmits 10 times along its trajectory (see Fig. 2.11).

Fig. 2.13 presents the model validation results for the 3GPP probabilistic LoS and mobility model. We can see that simulation results match well with the analytical results. This confirms that our proposed NOMA model can be applied to any trajectory model. We can see that the trajectory point at $n = 7$, has the highest total rate coverage probability. This is because at this point the AUE has close proximity to the terrestrial BS, and this is consistent with the trends discussed in the previous trajectory model.

Insights: Fig. 2.14 illustrates the minimum height of AUE that satisfies a target QoS requirement of 90%. Note that, at $\theta_{\mathrm{A}} = 30$ dB, trajectory points $n = 4$ and $n = 10$, fail to meet this QoS requirement within the given height range. This is due to the fact that these transmission points are located very close to the cell edge. We can see that for $\theta_{\mathrm{A}} = 20$ and 30 dB, the minimum height required to maintain a QoS of 90% increases and decreases at various points in the trajectory. *This*

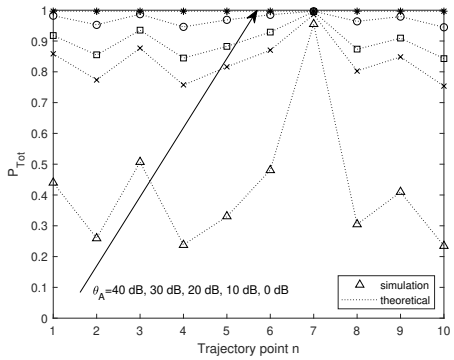

Figure 2.13: P_{Tot} for 3GPP-inspired trajectory model and probabilistic LoS model. The simulation values and the theoretical values are represented by bullets and dotted lines, respectively.

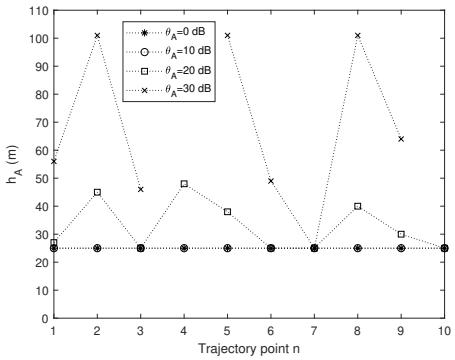

Figure 2.14: The minimum height of AUE to achieve a target QoS of 90% at each trajectory point in the urban environment for 3GPP-inspired trajectory model and probabilistic LoS model.

trend is different from the Archimedes' spiral trajectory where the minimum height increases as the AUE moves from the center to the cell edge. This highlights the importance of considering the specific UAV trajectory in the modeling and design of UAV communication systems.

2.5 Summary

In this Chapter, we focused on the coexistence of an AUE with a paired TUE in a cellular network. We assumed that the AUE flies in a given trajectory path and transmits to the BS periodically. To facilitate the concurrent uplink transmissions of the AUE and the TUE, we used an aerial-terrestrial NOMA scheme with SIC at the BS. We formulated an analytical framework that evaluates the rate coverage probability of each user and the system, at each transmission point on the trajectory. The numerical results showed that, for the spiral trajectory, the rate coverage probabilities decrease as the target data rate of the AUE increases and the AUE moves away from the BS. We also found the minimum height of AUE at each trajectory point in order to meet a QoS of 90% for different built-up environments. In the spiral trajectory, it was observed that the minimum height increases as the environmental parameters become more severe and when AUE moves towards the

cell edge. For the trajectory model adopted from the 3GPP study, it was observed that the minimum height increases and decreases depending on the distance of AUE from the BS.

Chapter 3

UAV-assisted IoT Monitoring Network: Adaptive Multiuser Access for Low-Latency and High-Reliability Under Bursty Traffic

In this Chapter, we propose an adaptive system design for an Internet of Things (IoT) monitoring network with latency and reliability requirements, where IoT devices generate time-critical and event-triggered bursty traffic, and an unmanned aerial vehicle (UAV) aggregates and relays sensed data to the base station. Existing transmission schemes based on the overall average traffic rates over-utilize network resources when traffic is smooth, and suffer from packet collisions when traffic is bursty which occurs in an event of interest. We address such problems by designing an adaptive transmission scheme employing multiuser shared access (MUSA) based grant-free non-orthogonal multiple access and use short packet communication for low latency of the IoT-to-UAV communication. Specifically, to accommodate bursty traffic, we design an analytical framework and formulate an optimization problem to maximize the performance by determining the optimal number of transmission time slots, subject to the stringent reliability and latency

constraints. We compare the performance of the proposed scheme with a non-adaptive power-diversity based scheme with a fixed number of time slots. Our results show that the proposed scheme has superior reliability and stability in comparison to the state-of-the-art scheme at moderate to high average traffic rates, while satisfying the stringent latency requirements.

This Chapter is organized as follows. Section 4.1 details the system model. Section 3.2 describes the proposed UAV-assisted IoT device transmission model. Section 3.3 presents the analytical framework used to compute the SINR coverage probability and short packet transmission error probability. Section 3.4 formulates and solves the optimization problem. Section 4.3 presents the results and illustrates the advantages of the proposed scheme. Section 4.4 concludes the Chapter.

3.1 System Model

We consider an IoT-based environmental monitoring system where low-powered and short-range IoT devices are required to transmit under specific reliability and latency requirements to a remote terrestrial BS that is out of the range of the IoT devices, as depicted in Fig. 3.1. To assist in the IoT-BS communication, a UAV is deployed as a data aggregator. The IoT devices that are located within the serving radius of the UAV transmit to the UAV and the successfully received data is aggregated and transmitted from the UAV to the BS. We assume that IoT-UAV and UAV-BS transmission phases are performed via orthogonal frequencies. Thus, there is no interference between these transmission phases. Also, the UAV uses a higher transmit power compared to the low-powered IoT devices. Furthermore, due to the high altitude of the UAV, it can establish high-quality communication with the BS. Thus, we assume highly reliable and fast communication between the UAV and the BS, and mainly focus on the IoT-UAV communication.

We assume that the IoT devices generate low-rate smooth traffic during the majority of the time, and UAV is only capable of handling low-rate traffic under normal system settings, while satisfying predetermined reliability and latency constraints. However, when an EoI occurs, high-rate bursty traffic is generated by the IoT devices. Thus, the UAV needs to change its operating mode to accommodate the change in traffic conditions in order to satisfy the reliability and latency require-

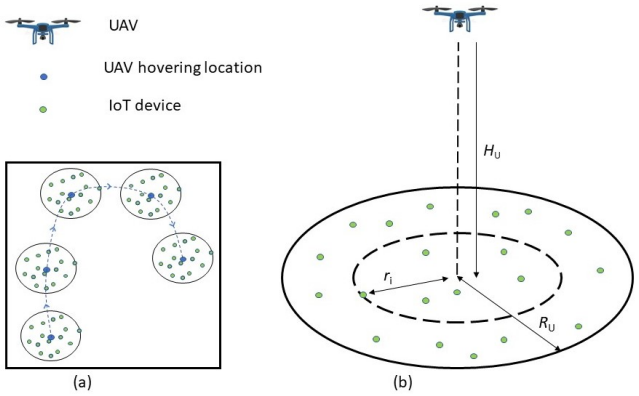

Figure 3.1: Illustration of the system model. Fig. (a) shows different hovering points of the UAV's trajectory within the cell. Note that the remote BS that is out of range of IoT devices is not shown in the figure as UAV-BS transmission is assumed to be highly reliable and fast. Thus, it is not the main focus of this work. Fig. (b) shows the serving zone area of the UAV at a given hovering point.

ments. In the next subsections, we present the IoT system and UAV deployment models, traffic generation pattern of EoI, and the communication channel models.

3.1.1 IoT System and UAV Deployment Model

The IoT devices are distributed on the ground, according to a homogeneous two-dimensional (2D) Poisson point process (PPP) with intensity ω. We assume that the UAV is deployed in a fly-and-hover manner, following a predetermined trajectory with multiple hovering locations within the cell to aggregate data from the transmitting IoT devices and transmit the aggregated data to the BS[1]. We also assume that the IoT-UAV data transmission only occurs at the hovering point[2]. The transmission protocol is similar at every hovering location. Therefore, for the rest of this work, we only focus on the system performance at a single hovering location.

When the UAV arrives at the hovering location, it hovers at a fixed altitude H_U for a fixed time duration T_{hov}. At the given altitude, the serving zone of the UAV is

[1]We assume that the UAV is initially located at the charging station and has sufficient energy to complete the communication tasks and return back to the charging station [59].

[2]The UAV trajectory design and optimization has been addressed in various existing studies, e.g., [137–139], and is outside the scope of this work.

defined as a disk of radius R_U. The hovering time duration T_{hov} consists of multiple transmission frames, each having a duration of t_{f}. In each frame, the IoT devices located within the serving zone become active with an activation probability P_A and remain active for the entire frame duration t_{f}. The transmitting devices are known as *active users*. The distribution of the active devices in a frame is modeled as a thinned PPP distribution with radius R_U with intensity $\varphi = \omega P_A$ [140]. Therefore, the number of active users in a transmission frame can be calculated as $N_{\text{A}} = \pi R_U^2 \omega P_A$.

3.1.2 Event-of-Interest Traffic Generation

We assume that the packets generated during the current frame are transmitted in the next frame. We also assume that an EoI can occur at any time. If an EoI occurs in the current frame, the system conditions to accommodate this change will occur in the next frame. We define the normal operating conditions and the EoI operating conditions of the IoT devices as the *non-emergency* scenario and *emergency* scenario, respectively, as described as follows:

Definition 3.1 *In the non-emergency scenario, each active device generates a single packet to transmit in the next frame.*

Definition 3.2 *In the emergency scenario where an EoI occurs, more devices become active and each active device generates multiple packets to transmit in the next frame. Specifically, each active device generates* $\rho_m \sim \text{Pois}(\lambda)$ *packets in the frame duration* t_{f}*, where* $m \in \{1, 2, \cdots, N_{\text{A}}\}$ *and* λ *is the average number of packets generated by an active device.*

The IoT devices transmit short packets of size D bits, and all packets must be transmitted in the next frame with the duration t_{f} which corresponds to the maximum allowable latency for transmission of packets[3]. We assume that the active device transmissions between two consecutive frames are independent of each other. Therefore, in the following we only focus on the transmission behavior in a single frame.

[3]In this work, the transmission durations of the short packets transmitted by the IoT devices, e.g., those considered in Section 4.3, conform to URLLC communication standards and the corresponding blocklengths are associated with the finite blocklength regime.

3.1.3 Channel Model

We model the IoT-UAV channel link as a combination of large-scale path loss, which depends on distance and height, and small-scale Rayleigh fading[4]. Particularly, we model its path loss as $\zeta_1 = \eta(r^2 + H_{\mathrm{U}}^2)^{\frac{\alpha}{2}}$, where r, η, and α correspond to the horizontal distance between the UAV and the IoT device, path loss attenuation coefficient, and path loss exponent, respectively [126]. The Rayleigh fading gain h follows an exponential distribution with unit mean. The PDF $f_h(x)$ and the CDF $F_h(x)$ of h are given by $f_h(x) = e^{-x}$ and $F_h(x) = 1-e^{-x}$, respectively. Moreover, the active IoT devices transmit to the UAV with fixed transmit power $\overline{\mathrm{P}} = \frac{P_{\max}}{\rho_{\max}}$, where $P_{\max}$ is the transmit power budget of an IoT device and $\rho_{\max} = \max_m\{\rho_m\}, \forall m$ is the maximum number of packets generated by an IoT device in a given frame[5].

3.2 Proposed UAV-assisted IoT Device Transmission Model

In this section, we employ the MUSA-based GF-NOMA scheme to support IoT-UAV transmission. The key contribution of Section 3.2 is two-fold: (i) EoI detection in Section 3.2.5 and (ii) Adaptive IoT-UAV transmission frame structure in Section 3.2.2. The MUSA-based GF NOMA scheme for IoT-UAV packet transmission in Section 3.2.3 and the ideal minimum mean squared error (MMSE) successive interference cancellation (SIC) for data recovery at the UAV in Section 3.2.4 are adapted from the literature and applied to our system model. The details are presented as follows.

[4]The studies [141–144] used Rayleigh fading to model the small-scale fading for ground-to-air (G2A) communication. Our analytical framework is valid for both Nakagami-m fading and Rayleigh fading models. However, due to the complexity of the analytical expressions in Section 3.3, the convexity of optimization problem presented in Section 3.4 cannot be analytically expressed for Nakagami-m fading. It has been shown in [141,145] that the quantitative performance trends in UAV communications remain unchanged even when the fading model is changed. For these reasons, we consider Rayleigh fading in this work.

[5]We assume that the UAV broadcasts the transmit power information to the IoT devices at the beginning of the time frame.

3.2.1 MUSA Spreading Code Generation

MUSA is a code-domain multiple access scheme. In this work, we use a binary complex spreading code consisting of $(+1, -1)$ with length J. Therefore, each element of the complex spreading code is produced from the set $\{1+i, -1+i, -1-i, 1-i\}$ before normalization. At the beginning of the transmission frame, the modulated symbols of each active device are spread by randomly chosen MUSA spreading codes, and the active devices' spread symbols are superimposed and transmitted on the same time-frequency resource.

3.2.2 IoT-UAV Transmission Frame Structure

We consider that each transmission frame consists of n_{s} time slots with a duration $t_{\mathrm{s}} = \frac{t_{\mathrm{f}}}{n_{\mathrm{s}}}$, as shown in Fig. 3.2. At the beginning of a frame, N_{A} devices randomly select time slots from n_{s} available time slots. Depending on the scenario, the active devices either have one packet per device or multiple packets per device to transmit within the frame duration. We assume that an active device can only transmit a single packet in one time slot. Therefore, the time slots allocated for the packets of a given device are orthogonal. Once the time slots are selected, the devices randomly allocate MUSA sequences for the packets. Unlike slot selection, the MUSA sequence selected by a device is not orthogonal. Then, the active devices transmit their packets in randomly selected time slots using the corresponding randomly selected MUSA sequences. The transmissions between two consecutive time slots are independent of each other. Therefore, in the following, we present the transmission scheme and the recovery procedure for a given time slot.

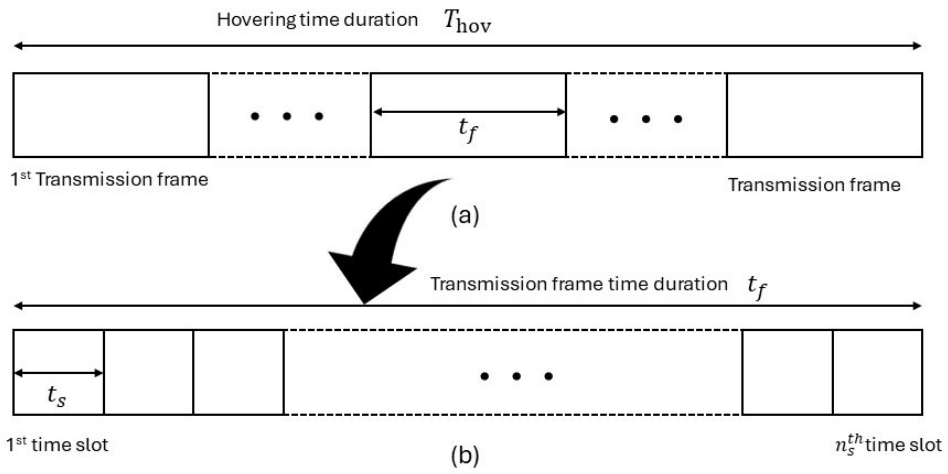

Figure 3.2: Illustration of the IoT-UAV transmission frame structure. Fig. (a) shows the hovering time duration which consists of multiple transmission frames with duration t_{f}. Fig. (b) shows a single transmission frame with n_{s} number of time slots with time slot duration t_{s}.

3.2.3 IoT-UAV Transmission Model

For a given time slot with $L_A \leq N_{\text{A}}$ active devices[6], D bits of each packet are modulated using binary phase shift keying to generate a stream of symbols for each device. After this, the modulated symbols of each device i, where $i \in \{1, 2, \cdots, L_A\}$, is spread with a randomly chosen complex spreading code s_i of length J and transmitted over J subcarriers. We denote $\mathbf{y} = [y_1, \cdots, y_J]^T$ as the superimposed signal of undecoded devices where $[\cdot]^T$ is the transpose. Then, $\mathbf{y}$ is given by

$$\mathbf{y} = \mathbf{G}\mathbf{P}^{\frac{1}{2}}\mathbf{x} + \mathbf{n}, \tag{3.1}$$

[6]We note that each active device generates $\rho_m \sim \text{Pois}(\lambda)$ packets in the frame duration t_{f}, where $m \in \{1, 2, \cdots, N_{\text{A}}\}$. Each active device randomly selects orthogonal time slots to transmit their packets within the transmission frame. When λ is high, if all N_{A} devices have a packet to transmit in a given time slot, the number of devices transmitting in that time slot is equal to the total number of active devices, and the condition $L_A = N_{\text{A}}$ is applicable. When λ is low, there are less packets transmitted in a given time slot and the number of devices transmitting in that time slot is less than the total number of active devices in the transmission frame; thus, the condition $L_A < N_{\text{A}}$ is applicable.

where $\mathbf{G} = [\mathbf{g}_1, \cdots, \mathbf{g}_{L_A}]$ is the equivalent channel of all the active devices, $\mathbf{x} = [x_1, \cdots, x_{L_A}]^T$ is the transmitted symbol vector, $\mathbf{P}^{\frac{1}{2}} = \text{diag}\left(\sqrt{\overline{\text{P}}}, \cdots, \sqrt{\overline{\text{P}}}\right) \in \mathbb{R}^{L_A \times L_A}$ is the transmit power matrix and $\mathbf{n} \sim \mathcal{CN}(0, \sigma^2 \mathbf{I}_J)$ is the noise vector. We then express $\mathbf{G}$ as $\mathbf{G} = \mathbf{H} \odot \mathbf{S}$, where $\mathbf{H} = [\mathbf{h}_1, \cdots, \mathbf{h}_{L_A}]$ with $\mathbf{h}_i = [h_{i,1}, \cdots, h_{i,J}]^T$ being the channel gain vector for the ith device, $\mathbf{S} = [\mathbf{s}_1, \cdots, \mathbf{s}_{L_A}]$ with $\mathbf{s}_i = [s_{i,1}, \cdots, s_{i,J}]^T$ being the MUSA sequence vector for the ith device, and $\odot$ is the element-wise product. We further denote $s_i \in S$ as the MUSA spreading code of length J chosen by the ith device, and $S = \left\{s_1, s_2, \cdots, s_{N_\mu}\right\}$ as the pool of spreading codes with $N_\mu = 9^J$ for binary MUSA spreading codes.

3.2.4 Data Recovery at UAV

At the UAV receiver, similar to prior studies [71,146–148], the ideal minimum mean squared error (MMSE) successive interference cancellation (SIC) is implemented to recover the transmitted data packets. We use this ideal MMSE SIC receiver due to its ability to achieve the best possible sum rate for detecting multiple data streams [70] and due to its low decoding complexity compared to other techniques such as message passing and maximum *a posteriori* estimation [147]. This receiver operates under ideal assumptions that the UAV has prior knowledge on the number of active users, their MUSA signatures, and fading channels. As our analytical framework does not rely on the instantaneous knowledge of the active users nor instantaneous channel conditions, we can use ideal MMSE SIC to retrieve the transmitted data in a time slot[7].

The SIC decoder uses the SINRs of the transmitting devices to estimate the transmitted symbols, reconstruct the interference, and decode the packets. This process is repeated until all the decodable packets are decoded. Moreover, we

[7]We note that, in reality, due to the GF nature of the access scheme, the UAV receiver may not have complete knowledge of the number active devices in the slot, their fading channels, and MUSA sequences. To address this practical concern, blind multi user detection (MUD) in MUSA is proposed [149,150]. The blind MUD uses blind estimation to select the device with the highest SINR by using blind channel estimation to reconstruct interference, and recover the transmitted symbols. Even though, the performance of blind MUD can approach that of ideal MMSE SIC, the implementation of which is relatively complex. Thus, we utilize the ideal MMSE SIC, which, although it requires prior knowledge of the active devices, their spreading sequences, and fading channels, is chosen for its simplicity. This approach, however, comes with a higher overhead compared to the blind MUD.

do not employ any power control mechanism at the IoT devices. Instead, the inherent received signal disparity due to the near-far effect and small-scale fading is utilized. Thus, the receiver utilizes both power disparity of the devices and low cross-correlation of the sequences to improve the decoding probability at the receiver. In the SIC decoding, the MMSE weights of the undecoded devices are computed at each iteration as [147]

$$\mathbf{W}^H = \left(\mathbf{P}^{\frac{1}{2}}\mathbf{G}^H\mathbf{G}\mathbf{P}^{\frac{1}{2}} + \sigma^2\mathbf{I}\right)^{-1}\mathbf{P}^{\frac{1}{2}}\mathbf{G}^H, \tag{3.2}$$

where $(\cdot)^H$ and $\mathbf{I}$ correspond to the Hermitian transpose and identity matrix, respectively.

The undecoded devices are then sorted based on the distance, and the undecoded device with the minimum distance at the kth iteration, where $k \in \{1, \cdots, L_A\}$, is considered as the kth strongest device. The SINR of the kth strongest device is given by [71]

$$\gamma_k = \frac{\overline{\mathrm{P}}|w_k^H g_k|^2}{\sum_{i=1+k}^{L_A}\overline{\mathrm{P}}|w_i^H g_i|^2 + \sigma^2\|w_k^H\|}, \tag{3.3}$$

where w_k is the kth MMSE weight. In this work, we consider that an active device in a given time slot is subjected to MUSA collision if it selects the same MUSA spreading code as another active device in the same time slot. We consider that the kth strongest device is decoded if it is not subject to MUSA collision and γ_k exceeds a given threshold θ_{T}. Otherwise, we consider that the kth strongest device and the rest weaker devices cannot be decoded. The decoded signal is reconstructed and its contribution to $\mathbf{y}$ is removed. This process is repeated until all the devices are decoded, provided there are no MUSA collisions and their SINRs exceed θ_{T}.

3.2.5 Event-of-Interest Detection

The existing transmission schemes and access mechanisms are designed based on overall average traffic rates, such that they over-utilize network resources under low-rate traffic but suffer from packet collisions under high-rate traffic. Thus, it is important to identify the occurrence of EoI so that the UAV-assisted IoT device transmission scheme is adapted to accommodate the change in traffic patterns

while ensuring the efficient utilization of time-frequency resources. Therefore, in this subsection we propose the following approach to determine the occurrence of an EoI.

To determine if an EoI has occurred, the UAV performs the following procedure at the beginning of the current time frame. Prior to the transmission, the UAV knows the number of actives devices N_{A} and the total number of packets ρ_{Σ} to be transmitted in the frame[8]. The UAV determines the occurrence of an EoI and changes its operating mode in the emergency scenario. The main parameter that determines the severity of the emergency scenario is λ which is the rate of a Poisson distribution. λ can be estimated by using the Multiple Hypothesis test. In this test, $M-1$ independent hypotheses are tested as $\mathcal{H}_2, \cdots, \mathcal{H}_M$, where $\mathcal{H}_i$ is the event that $\lambda = i$, and the corresponding probability densities for x conditioned on the given hypothesis is given as $p_{x|\mathcal{H}}(y|\mathcal{H}_i) = \frac{i^x e^{-i}}{x!}$, where $x = \overline{\lambda}$ is the calculated mean [128]. Then, the Maximum Likelihood Ratio test is conducted for $\mathcal{H}_i$ versus $\mathcal{H}_{i+1}$ to obtain $\widehat{\lambda}$ as

$$\Delta(x) = \frac{p_{x|\mathcal{H}}(y|\mathcal{H}_i)}{p_{x|\mathcal{H}}(y|\mathcal{H}_{i+1})} \underset{\mathcal{H}_i}{\overset{\mathcal{H}_{i+1}}{\gtrless}} 1. \tag{3.4}$$

The estimated λ is given by τ, where $\mathcal{H}_\tau$ is the decision of the Multiple Hypothesis test. However, this approach has a higher computational complexity. Thus, we adopt a simpler approach for estimating λ where λ can be approximated as $\overline{\lambda}$, with $\overline{\lambda} = \frac{\rho_{\Sigma}}{N_{\mathrm{A}}}$. If $\overline{\lambda} > 1$, the UAV determines the occurrence of an EoI and changes its operating mode in the emergency scenario.

The analytical framework presented in this work is applicable for any value of λ regardless of the estimation method. Thus, in the next section, we present an analytical framework to assess the performance of the system for the emergency scenario for a given λ.

[8]Note that active user detection has been widely addressed in the literature, which can be used by the UAV to know N_{A}.

3.3 Analytical Framework

The performance of the proposed UAV-IoT transmission protocol in Section 3.2 depends on (i) the SINRs in (3), (ii) the MUSA sequence collisions of the active devices within a transmission frame, (iii) the distance-based ordering of the undecoded devices, and (iv) decoding errors at the UAV due to short packet communication. While it may be possible to define a single metric that takes all these factors into account, we do not take this approach. Instead, for the sake of analytical tractability, and to ensure to convexity of the optimization problem in Section 3.4, we choose to define two metrics. The first metric accounts for the first three factors, while the second metric accounts for the short packet error probability. This choice allows us to leverage stochastic geometry to calculate the first metric, which is not derived in the prior literature for the considered system, and use the existing definition in the short packet communication literature to assess the second metric. and use the existing definition in the short packet communication literature to assess the second metric. Both metrics are then used to formulate the optimization problem in Section 3.4[9], to which we will develop an analytical solution.

The definitions and results for the two metrics are presented in the next subsections.

3.3.1 SINR Coverage Probability

Definition 3.3 *The SINR coverage probability within a transmission frame, P_{sc}, is defined as the average probability that a packet transmitted by a device in a given time slot within the transmission frame is not subjected to MUSA collision and the SINR exceeds a certain threshold θ_{T}.*

[9]In Section 3.4, we formulate the optimization problem such that the SINR coverage probability of an active device having multiple packets to transmit during a transmission frame is maximized by optimizing the number of time slots in the transmission frame, while satisfying the latency and reliability constraints of short packet transmission. In the emergency scenario, if the UAV's operating mode is not changed by optimizing the number of time slots within the transmission frame, the short packet transmission reliability will decrease due to high rate traffic generated by multiple packets of the active devices. It must be noted that the focus of this work is not on minimizing the short packet transmission error probability, but on maintaining it at an acceptable level. Thus, it is mathematically appropriate to consider two separate metrics.

In a given time slot, the active devices with unique MUSA sequences are defined as *singleton* devices, whereas the active users with colliding MUSA sequences are defined as *collided* devices. We assume that the singleton devices are in SINR coverage if their SINRs exceed θ_{T}. On the other hand, we assume that the collided devices are not in SINR coverage. Thus, the SINR for a given singleton device, denoted as γ, is expressed as

$$\gamma = \frac{\overline{\mathrm{P}}\eta\left(\widehat{r}^2 + H_{\mathrm{U}}^2\right)^{-\frac{\alpha}{2}} h}{I_{\mathrm{s}} + I_{\mathrm{s}} + \sigma^2}, \tag{3.5}$$

where $\widehat{r}$ corresponds to the horizontal distance between a singleton device and UAV, and σ^2 is the noise power, $I_{\mathrm{s}} = \sum_{i\in\phi_s} \overline{\mathrm{P}}\eta(r_i^2 + H_{\mathrm{U}}^2)^{-\frac{\alpha}{2}} h_i$ and $I_{\mathrm{c}} = \sum_{j\in\phi_c} \overline{\mathrm{P}}\eta(r_j^2 + H_{\mathrm{U}}^2)^{-\frac{\alpha}{2}} h_j$ denote the aggregate interference caused by the weaker singleton devices and all the collided devices, respectively, ϕ_s represents the homogeneous PPP of the interfering singleton devices with intensity φ_s, and ϕ_c represents the homogeneous PPP of the collided devices with intensity φ_c. Both ϕ_s and ϕ_c are independent thinned PPP distributions of ϕ and the corresponding intensities can be derived using Lemmas 3.3.1 and 3.3.2.

Next, we present useful Lemmas and Proposition to derive the SINR coverage probability P_{sc} defined in (3.5). First, we derive the probability that a packet of an active device chooses any time slot in Lemma 3.3.1 and the probability that a random device transmitting in a given time slot is not subjected to MUSA sequence collision in Lemma 3.3.2. Then, we characterize the singleton and collided interference in Lemmas 3.3.4 and 3.3.5, respectively. Finally, we present the expression for the SINR coverage probability P_{sc} in Theorem 3.1.

Lemma 3.3.1 *Given that the average number of packets generated by an active device is λ, and the number of time slots available for transmission is n_{s}, the probability that a packet of an active device chooses any time slot, denoted by P_λ, is given by*

$$P_\lambda = \sum_{L=1}^{n_{\mathrm{s}}} \frac{e^{-\lambda}\lambda^L}{n_{\mathrm{s}}(L-1)!} + \sum_{L=n_{\mathrm{s}}+1}^{\lambda+L_{\mathrm{lim}}} \frac{e^{-\lambda}\lambda^L}{L!}. \tag{3.6}$$

where L_{lim} corresponds to a constant which truncates the Poisson distribution of number of packets generated by an active device.

Proof

P_λ is expressed as

$$P_\lambda = \sum_L P_{\lambda|L} f_\lambda(L), \tag{3.7}$$

where $P_{\lambda|L}$ is the conditional probability of a device choosing any time slot from n_s available time slots to transmit one of its packets, given that the device has $L \sim \mathrm{Pois}(\lambda)$ number of packets to transmit within the time frame. Specifically, $P_{\lambda|L}$ is given by

$$P_{\lambda|L} = \begin{cases} \frac{L}{n_\mathrm{s}}, & \text{if } L < n_\mathrm{s} \\ 1, & \text{otherwise,} \end{cases} \tag{3.8}$$

where $f_\lambda(L) = e^{-\lambda}\frac{\lambda^L}{L!}$ is the PDF of the number of packets generated by an active device.

Lemma 3.3.2 *The collision free probability, P_cf, which is the probability that an active device in a given time slot does not choose the same MUSA sequence as another active device in the same time slot, is given by*

$$P_\mathrm{cf} = (1-P_\lambda)^{N_\mathrm{A}-1} + \sum_{n=1}^{N_\mathrm{A}-1} \binom{N_\mathrm{A}-1}{n} {P_\lambda}^n (1-P_\lambda)^{N_\mathrm{A}-n-1} \left(\frac{N_\mu - 1}{N_\mu}\right)^n. \tag{3.9}$$

Proof

For a device to be collision free in a given time slot, either no other device transmits on the same time slot or the devices that transmit on the same time slot must not choose the same MUSA sequence as the considered device. Thus, the collision free probability of a device can be expressed as

$$P_\mathrm{cf} = P_o + P_\sum, \tag{3.10}$$

where $P_o = (1-P_\lambda)^{N_\mathrm{A}-1}$ is the probability that only one device, out of N_A devices, is active and all the other $N_\mathrm{A}-1$ devices are not active in the given time slot. Moreover, $P_\sum$ is the probability that given a device and $n \in \{1, \cdots, N_\mathrm{A}-1\}$ other devices are active in the given time slot, there is no MUSA sequence collision between the considered device and other n active devices. We then derive $P_\sum$ as follows:

The probability that n devices transmit in a given time slot is given by $(P_\lambda)^n(1-P_\lambda)^{N_\mathrm{A}-1-n}\binom{N_\mathrm{A}-1}{n}$ and the probability that n devices do not choose the same MUSA sequence as the considered device in the same time slot is given by $\left(\frac{N_\mu-1}{N_\mu}\right)^n$. Therefore, $P_{\sum}$ can be derived as

$$P_{\sum} = \sum_{n=1}^{N_\mathrm{A}-1} \binom{N_\mathrm{A}-1}{n} (P_\lambda)^n (1-P_\lambda)^{N_\mathrm{A}-n-1} \left(\frac{N_\mu-1}{N_\mu}\right)^n. \tag{3.11}$$

Using Lemmas 3.3.1 and 3.3.2, the number of singleton devices L_s, in a given time slot can be computed as $L_s = N_\mathrm{A} P_\lambda P_\mathrm{cf}$. Next, we characterize the distance distribution and the interference on the singleton devices. First, we present an assumption for the purpose of analytical tractability.

Assumption 3.3.1 *The impact of path loss is more dominant compared to that of small-scale fading on the received signal power. Thus, for analytical tractability, we consider the fixed NOMA decoding order strategy based on the distance of devices from the UAV, as opposed to the dynamic NOMA decoding order strategy based on the instantaneous received signal power. Therefore, the distance-based ordering of L_s singleton devices is $r_1 \geq r_2 \geq \cdots r_k \geq \cdots r_{L_s}$, where r_1 is the horizontal distance of the strongest device that would be decoded first and r_{L_s} is that of the weakest device that would be decoded last. It follows that for the kth strongest device with $\widehat{r} = r_k$, the interference from the singleton devices is only generated by devices located farther away from $\widehat{r}$ from the UAV [128].*

Next, we characterize the distance distribution of the kth strongest singleton device in Lemma 3.3.3 based on Assumption 3.3.1.

Lemma 3.3.3 *The distance distribution of the kth strongest singleton device located at a horizontal distance $\widehat{r}$ away from the UAV is given by*

$$f_{\widehat{r}}(x) = \frac{L_s!}{(j-1)!(L_s-j)!} \left(\frac{2\widehat{r}^{2j-1}}{R_U^{2j}}\right) \left(1-\frac{\widehat{r}^2}{R_U^2}\right)^{L_s-j}, \tag{3.12}$$

where L_s is the number of singleton devices in the time slot.

Proof

Based on the kth order statistics, the PDF of the distance distribution $r_k = \widehat{r}$ of the kth strongest device is expressed as

$$f_{\widehat{r}}(x) = \frac{L_s!}{(k-1)!(L_s-k)!} f_r(x)(F_r(x))^{k-1}(1-F_r(x))^{L_s-k}, \tag{3.13}$$

where $f_r(x) = \frac{2x}{R_U^2}$ and $F_r(x) = \frac{x^2}{R_U^2}$ are the PDF and CDF of the distance distribution of a device located at a horizontal distance of x away from the UAV serving zone of radius R_U, respectively.

For a given time slot, to characterize the aggregated interference $I_\mathrm{s} + I_\mathrm{c}$ at the kth strongest singleton device located at a horizontal distance of $\widehat{r}$ from the UAV, we compute the Laplace transforms of I_s and I_c at s, conditioned on the random distance $\widehat{r}$, which we denote by $\mathcal{L}_{I_\mathrm{s}}(s)$ and $\mathcal{L}_{I_\mathrm{c}}(s)$, respectively.

Lemma 3.3.4 *The Laplace transform of interference on the kth strongest singleton device generated by the weaker singleton devices, denoted by $\mathcal{L}_{I_\mathrm{s}}(s)$, is derived as*

$$\mathcal{L}_{I_\mathrm{s}}(s) = \exp\left(-2\pi\varphi P_\mathrm{cf} \int_{\widehat{r}}^{R_U} \left(1 - \frac{1}{1 + s\overline{\mathrm{P}}\eta(r^2 + {H_\mathrm{U}}^2)^{-\frac{\alpha}{2}}}\right) r dr\right). \tag{3.14}$$

Proof

Please see Appendix B.1.

Lemma 3.3.5 *The Laplace transform of interference on the kth strongest singleton device generated by the collided devices, denoted by $\mathcal{L}_{I_\mathrm{c}}(s)$, is derived as*

$$\mathcal{L}_{I_\mathrm{c}}(s) = \exp\left(-2\pi\varphi(1-P_\mathrm{cf}) \int_{0}^{R_U} \left(1 - \frac{1}{1 + s\overline{\mathrm{P}}\eta(r^2 + {H_\mathrm{U}}^2)^{-\frac{\alpha}{2}}}\right) r dr\right). \tag{3.15}$$

Proof

The proof of (3.15) is similar to that of (3.14), except that the collided devices form a thinned PPP distribution of intensity $\varphi_c = \varphi(1-P_\mathrm{cf})$ within a disk of radius R_U. Therefore, the lower and upper integral limits in Campbell's theorem correspond to 0 and R_U, respectively.

Next, we derive the probabilities associated with the SINR coverage of the singleton devices. First, we present the conditional probability that the kth strongest

singleton device is in SINR coverage given the stronger singleton devices are in SINR coverage in Proposition 3.1. Then, we present the SINR coverage probability within a transmission frame in Theorem 3.1.

Proposition 3.1 *In a given time slot, the conditional probability that the kth strongest singleton device located at a horizontal distance of $\widehat{r}$ away from the UAV is in SINR coverage, given that $k-1$ stronger singleton devices are in SINR coverage, is derived as*

$$P_{COND}^{k} = \int_{0}^{R_U} \exp(-s\sigma^2)\mathcal{L}_{I_s}(s)\mathcal{L}_{I_c}(s)\frac{L_s!}{(j-1)!(L_s-j)!}\left(\frac{2\widehat{r}^{2j-1}}{R_U^{2j}}\right)\left(1-\frac{\widehat{r}^2}{R_U^2}\right)^{L_s-j} d\widehat{r}, \tag{3.16}$$

where $s = \frac{\theta_{\mathrm{T}}\left(\left(\widehat{r}\right)^2+H_{\mathrm{U}}^2\right)^{\frac{\alpha}{2}}}{\overline{\mathrm{P}}\eta}$ and L_s is total number of singleton devices in a given time slot.

Proof

P_{COND}^{k} can be expressed as

$$P_{COND}^{k} = \int_{0}^{R_U} P_{SIC|\widehat{r}}^{k}(s) f_{\widehat{r}}(\widehat{r}) d\widehat{r}, \tag{3.17}$$

where $P_{COND|\widehat{r}}^{k}$ is the conditional probability that the kth singleton device is in SINR coverage given it is located at $\widehat{r}$ distance from the UAV. To further derive (3.17), we obtain $P_{SIC|\widehat{r}}^{k}$ as

$$\begin{aligned}
P_{SIC|\widehat{r}}^{k}(s) &= \Pr\left(\frac{\overline{\mathrm{P}}\eta\left(\widehat{r}^2+{H_{\mathrm{U}}}^2\right)^{-\frac{\alpha}{2}}h}{I_{\mathrm{s}}+I_{\mathrm{c}}+\sigma^2} \geq \theta_{\mathrm{T}}\right) \\
&= \mathbb{E}_{I_{\mathrm{s}},I_{\mathrm{c}}}\left[1-F_h\left(\frac{\theta_{\mathrm{T}}\left(\widehat{r}^2+{H_{\mathrm{U}}}^2\right)^{-\frac{\alpha}{2}}}{\overline{\mathrm{P}}\eta}(I_{\mathrm{s}}+I_{\mathrm{c}}+\sigma^2)\right)\right] \\
&= \mathbb{E}_{I_{\mathrm{s}},I_{\mathrm{c}}}\left[\exp\left(-s(I_{\mathrm{s}}+I_{\mathrm{c}}+\sigma^2)\right)\right] \qquad (3.18a) \\
&= \exp(-s\sigma^2)\mathbb{E}_{I_{\mathrm{s}}}\left[\exp(-sI_{\mathrm{s}})\right]\mathbb{E}_{I_{\mathrm{c}}}\left[\exp(-sI_{\mathrm{c}})\right] \\
&= \exp(-s\sigma^2)\mathcal{L}_{I_{\mathrm{s}}}(s)\mathcal{L}_{I_{\mathrm{c}}}(s),
\end{aligned}$$

where (3.18a) is obtained using the CDF of the small-scale fading gain h and

$s = \frac{\theta_{\mathrm{T}}\widehat{r}^{\alpha}}{\overline{\mathrm{P}}\eta}$. By substituting (3.14), (3.15), (3.18), and (3.12) to (3.17), we obtain (3.16).

Next, we present another assumption made for the sake of tractable analysis.

Assumption 3.3.2 *In a given time slot, for a singleton device to be in SINR coverage, the singleton devices with the stronger average received powers, i.e., singleton devices that are closer to the UAV than the current specified singleton device, must be in SINR coverage. Since the singleton devices are independently distributed in R_U and the small-scale fading is exponentially distributed, the SINR coverage events of singleton devices are assumed to be independent.*

We now derive and present P_{sc} in the following theorem.

Theorem 3.1 *The SINR coverage probability within the transmission frame, P_{sc}, which is the average probability that a packet transmitted by a device in a given time slot within the frame is not subjected to MUSA collision and the SINR exceeds a certain threshold θ_{T}, is given by*

$$\begin{aligned} P_{\mathrm{sc}} = & \sum_{k=1}^{L_s} \frac{n_{\mathrm{s}}}{N_{\mathrm{A}}\lambda} \prod_{j=1}^{k} \int_0^{R_U} \exp(-s\sigma^2) \exp\left(-2\pi\varphi P_{\mathrm{cf}} \int_{\widehat{r}}^{R_U} \left(1 - \frac{1}{1 + s\overline{\mathrm{P}}\eta(r^2 + {H_{\mathrm{U}}}^2)^{-\frac{\alpha}{2}}}\right) r dr\right) \\ & \times \exp\left(-2\pi\varphi(1 - P_{\mathrm{cf}}) \int_0^{R_U} \left(1 - \frac{1}{1 + s\overline{\mathrm{P}}\eta(r^2 + {H_{\mathrm{U}}}^2)^{-\frac{\alpha}{2}}}\right) r dr\right) \\ & \times \frac{L_s!}{(j-1)!(L_s - j)!} \left(\frac{2\widehat{r}^{2j-1}}{R_U^{2j}}\right) \left(1 - \frac{\widehat{r}^2}{R_U^2}\right)^{L_s - j} d\widehat{r}, \end{aligned} \tag{3.19}$$

where $s = \frac{\theta_{\mathrm{T}}\widehat{r}^{\alpha}}{\overline{\mathrm{P}}\eta}$.

Proof

Based on Assumption 3.3.2, the probability that the kth strongest device is in SINR coverage is given as $P_{\mathrm{COV}}^k = \prod_{j=1}^{k} P_{COND}^j$. The probability that the devices are in SINR coverage within the transmission frame is given by $\frac{\sum_{k=1}^{L_s} P_{\mathrm{COV}}^k n_{\mathrm{s}}}{N_{\mathrm{A}}\lambda}$. Thus, substituting (3.18) into this, we obtain (3.19).

Remark 3.1 *For a given n_{s}, when the number of devices N_{A} and the average number of packets λ increase, the SINR coverage probability within the transmission*

frame decreases. On the other hand, for a given N_{A} and λ, when n_{s} increases, the SINR coverage probability within the transmission frame increases.

Remark 3.2 *We note that P_{sc} in* (3.19) *does not depend on the maximum transmit power, as we assume that all the active devices in the transmission frame transmit with equal power $\overline{\mathrm{P}}$. As such, P_{sc} gives the lower bound on the performance, due to lower receiver power diversity.*

3.3.2 Short Packet Transmission Error Probability

To address the decoding errors at the UAV due to short packet communications in the analysis, we define the short packet transmission error probability, denoted by ϵ, as follows.

Definition 3.4 *In the finite block regime, the short packet transmission error probability, ϵ, is defined as the error probability of receiving D bits of data within a single time slot duration $t_{\mathrm{s}} = \frac{t_{\mathrm{f}}}{n_{\mathrm{s}}}$, when the SINR of the device is γ. Here, ϵ characterizes the reliability of the system, given by [74]*

$$\epsilon = \mathbb{Q}\left[\sqrt{\frac{Bt_{\mathrm{f}}}{Vn_{\mathrm{s}}}}\left(\log_2\left(1+\gamma\right) - \frac{Dn_{\mathrm{s}}}{Bt_{\mathrm{f}}}\right)\right], \tag{3.20}$$

where $\mathbb{Q}\left[\cdot\right]$ is the Q-function, B, t_{f}, D, V, and n_{s} represent the bandwidth, frame duration which is the maximum allowable latency, size of the short packet transmitted in a time slot, channel dispersion, and the number of time slots, respectively.

Remark 3.3 *Given a device which has an SINR γ and packet size of D, its transmission reliability increases when the transmission duration increases. Thus, we see from* (3.20) *that ϵ decreases when the number of time slots n_{s} within the frame increases.*

It can be seen from Remarks 3.1 and 3.3 that both SINR coverage probability P_{sc} and short packet decoding error probability ϵ depend on the number of time slots n_{s} within a transmission frame. Therefore, in an EoI both P_{sc} and ϵ must be considered simultaneously when UAV changes its operating mode to accommodate the change in traffic conditions, for satisfying the relevant reliability and

latency constraints. Thus, in the next section, we propose an adaptive transmission scheme to prevent the over-utilization of resources under low-rate traffic and under-utilization of resources under high-rate traffic, by optimizing the number of time slots in a transmission frame.

3.4 Proposed Adaptive Transmission Scheme

In this section, we propose an adaptive transmission scheme for IoT-UAV communication by optimizing the number of time slots to maximize the SINR coverage probability of active devices under stringent reliability constraint (i.e., maximum short packet transmission error probability) and latency constraint in an EoI.

From (3.19), we can see that the SINR coverage probability is a function of the MUSA collision probability and the SINR. The MUSA collision probability is inversely proportional to the number of time slots in a frame. When the number of time slots increases, the average number of devices with colliding MUSA sequence increases. This decreases the number of singleton devices that can be recovered via SIC decoding and decreases the SINR coverage probability. Moreover, when the number of singleton devices in a time slot increases, the interference on the stronger singleton devices caused by the weaker singleton devices increases. This decreases the SINR and decreases the SINR coverage probability. On the other hand, when the number of time slots increases, the transmission time of a packet decreases and thus, the short packet transmission reliability decreases. Clearly, there is a trade-off between having less collisions and achieving high transmission reliability. To address this trade-off, we define the optimization problem as "*What is the optimal number of time slots that maximizes the SINR coverage probability of an active device having multiple packets to transmit within a given time duration t_{f}, while satisfying the reliability constraints of short packet transmission?*" We formulate this optimization problem with design parameter n_{s}, which is then used to reveal optimal t_{s}, as follows:

$$\begin{aligned} \mathbf{OP}: &\min_{n_{\mathrm{s}}} \ (-P_{\mathrm{sc}}) \\ \text{s.t. } \mathrm{C}_1: &n_{\mathrm{s}} - (N_{\mathrm{A}}\lambda + \delta(\lambda)) \leq 0, \end{aligned} \tag{3.21a}$$

$$\mathrm{C}_2 : \lambda - n_{\mathrm{s}} \leq 0, \tag{3.21b}$$

$$\mathrm{C}_3 : \mathbb{Q}\left[\sqrt{\frac{Bt_{\mathrm{f}}}{Vn_{\mathrm{s}}}}\left(\log_2\left(1+\gamma\right) - \frac{Dn_{\mathrm{s}}}{Bt_{\mathrm{f}}}\right)\right] - \epsilon \leq 0 \tag{3.21c}$$

$$\mathrm{C}_4 : \lambda_{\min} - \lambda \leq 0, \tag{3.21d}$$

$$\mathrm{C}_5 : \lambda - \lambda_{\max} \leq 0, \tag{3.21e}$$

$$\mathrm{C}_6 : R_{\min} - R_U \leq 0. \tag{3.21f}$$

where $n_{\mathrm{s}} = \frac{t_{\mathrm{f}}}{t_{\mathrm{s}}}$, with $t_{\mathrm{f}}, t_{\mathrm{s}} \in \mathbb{R}$. Thus, $n_{\mathrm{s}} \in \mathbb{R}$. However, in reality $n_{\mathrm{s}} \in \mathbb{Z}^+$. Therefore, to solve this OP, we relax this constraint and consider $n_{\mathrm{s}} \in \mathbb{R}$, and then use $\widetilde{n}_{\mathrm{s}} = \lfloor n_{\mathrm{s}}^* \rfloor$, where n_{s}^* is the solution to the **OP**, and $\widetilde{n}_{\mathrm{s}}$ is the practical value of number of time slots.

C_1 defines an approximate upper bound on the number of time slots. While this upper bound ensures the efficient use of resources, $\delta(\lambda)$ in C_1 is a constant that ensures that the resources are not overused, i.e., lower $\delta(\lambda)$ allows a higher upper bound and vice versa. C_2 defines the lower bound where the number of time slots must be greater than the average number of packets generated by a device. This ensures the minimal packet drop at the UAV. C_3 mandates that the error in short packet transmission satisfies the reliability constraint, where ϵ in (3.21c) is the maximum allowable error in short packet transmission and V is approximated as $(\log_2(e))^2$ [74]. Moreover, C_3 ensures that the successful transmission of a packet is completed within a maximum allowable latency of t_{f}. In C_3, we assume that the minimum time slot duration is associated with the maximum SINR, as the time slot duration is inversely proportional to the SINR for a given ϵ. We also assume that the maximum SINR corresponds to the scenario where the device closest to the UAV is the only active device in a given time slot. Thus, γ in (3.21c) is approximated by signal-to-noise ratio for mathematical tractability. C_4 defines the lower bound on λ where $\lambda_{\min}$ is the minimum λ for mode transition in an emergency scenario. C_5 defines the upper bound on λ where $\lambda_{\max}$ the worst case practical value for λ in an emergency scenario. C_6 is the minimum serving radius of the UAV aggregator.

The objective function and the constraints in (3.21) satisfy the second-order constraints for convexity [151]. Thus, **OP** in (3.21) is a convex optimization prob-

lem. Therefore, the optimal solution to the **OP** can be obtained by finding the solution that satisfy the relevant Karush-Kuhn-Tucker (KKT) conditions.

Theorem 3.2 *The practical number of time slots $\widetilde{n}_{\mathrm{s}}$, which will maximize P_{sc} within the frame duration t_{f} in an emergency scenario where the active devices generate λ packets in average is given by*

$$\widetilde{n}_{\mathrm{s}} = \lfloor n_{\mathrm{s}}^{*} \rfloor = \lfloor \min \{ n_{\mathrm{s}\lambda}, n_{\epsilon} \} \rfloor, \tag{3.22}$$

where, n_{s}^{*} is the solution to the **OP** *in* (3.21)*, $n_{\mathrm{s}\lambda} = N_{\mathrm{A}}\lambda + \delta(\lambda)$ and n_{ϵ} is given by the solution to the following equation*

$$\mathbb{Q}\left[\sqrt{\frac{Bt_{\mathrm{f}}}{n_{\epsilon}}} \left(\ln(1+\gamma) - \frac{D}{Bt_{\mathrm{f}}} \ln(2) n_{\epsilon} \right) \right] - \epsilon = 0. \tag{3.23}$$

Proof

Please see Appendix B.2.

Remark 3.4 *The average number of packets λ provides a lower bound on the optimal design variable on the optimization problem in* (3.21)*. We note that $\min(n_{\mathrm{s}\lambda}, n_{\epsilon})$ gives the optimal design parameter n_{s}^{*} when the all the constraints are slack, except for the first constraint. Particularly, $n_{\mathrm{s}\lambda}$ is the optimal number of time slots when the traffic is low. On the other hand, n_{ϵ} is the optimal number of time slots when the traffic is relatively high. This is due to the fact that in the emergency scenario where λ is high, the upper bound on the allowable number of time slots is bounded by the reliability constraint associated with short packet transmissions.*

Remark 3.5 *The optimal solution to* **OP** *depends on the statistical channel information, the average number of packets λ which can be estimated, and the active number of devices N_{A} which is known to the UAV at the beginning of the frame. Hence, in our proposed adaptive transmission scheme, the UAV can solve* **OP** *for different N_{A} and λ before transmission begins. We note that the UAV is only required to solve the* **OP** *when an EoI occurs. Once an EoI is detected in the transmission frame by performing the EoI detection procedure in Section 3.2.5, Hence,*

Table 3.1: Parameter values for numerical and simulation results.

Parameter	Symbol	Value	Parameter	Symbol	Value
UAV serving zone radius	R_U	50 m	SINR threshold	θ_{T}	0 dB
Time frame duration	t_{f}	10^{-3} s	Pathloss coefficient	η	0 dB
Packet size	D	200 bits	Pathloss exponent	α	2.2
Bandwidth	B	5 MHz	Noise power	σ^2	-100 dBm
Number of MUSA sequences	N_μ	64	Maximum transmit power	$P_{\max}$	10 dBm

in our proposed adaptive transmission scheme, the UAV can solve **OP** *for different* N_{A} *and* λ *before transmission begins. We note that the UAV is only required to solve the* **OP** *when an EoI occurs. Once an EoI is detected in the transmission frame by performing the EoI detection procedure in Section 3.2.2 to* $\widetilde{n}_{\mathrm{s}}$ *based on the severity of the emergency scenario.*

3.5 Numerical Results

In this section, we first evaluate the performance of the system in an emergency scenario under the non-optimal setting. The performance evaluation is conducted with respect to the number of active users N_{A}, severity of the emergency scenario which correlates to the average number of packets λ generated by a user, and the number of available time slots n_{s} to transmit within the given latency constraint t_{f} seconds. Next, we compare the performance of the proposed scheme presented in Section 3.4 to several benchmarks.

The simulation results for the MUSA-based GF-NOMA with ideal MMSE MUD scheme are obtained using system level computer simulations in Matlab where we average over 10^4 Monte Carlo simulation runs. The analytical results are obtained using (3.19) and the proposed scheme is obtained using (3.22). The numerical integrations in (3.19) are evaluated using Mathematica or approximated with Simpson's integral. In the **OP**, the gamma function, harmonic number function, Barnes-G function, and Q-function are evaluated numerically using Mathematica. The parameter values used for the results are presented in Table 4.1. We clarify that these values are consistent with other relevant studies in the literature, e.g., [117, 152, 153]. For the purpose of generating the results, we consider a fixed UAV altitude $H_{\mathrm{U}} = 125$ m, and assume that the IoT-UAV communication link has unit probability of line-of-sight at all times [154].

3.5.1 Model Validation and SINR Coverage Probability Behavior

Fig. 3.3(a) plots the SINR coverage probability P_{sc} within a transmission frame as a function of the average number of packets λ per active device, for a given number of active users N_{A} at a given hovering location while considering a maximum allowable latency of $t_{\text{f}} = 10^{-3}$ s. The results are presented for $N_{\text{A}} = 10, 15, 20$ active devices for a fixed number of time slots ($n_{\text{s}} = 20$). We observe that both analytical and simulation results present the same trends, as N_{A} and λ vary. The simulation results match reasonably well with the analytical results at severe traffic conditions, i.e., high N_{A} and λ values. The gap between the simulation and the analytical results at light traffic conditions, i.e., low N_{A} and λ values, can be attributed to assumptions made in the analytical framework. First, in the analytical framework, we estimate the number of singleton devices L_s in a time slot using the collision free probability P_{cf} in (3.9) and the number of devices transmitting in each time slot. However, due to the probabilistic nature of this approach, L_s is not always an integer. Thus, in the analytical framework, we consider the contribution of the fractional singleton devices to the SIC decoding process. Similarly, the interference at the decoding device also consists of fractional collided devices. In the simulation, no approximation on fractional devices is made and N_{A} active devices within the frame randomly choose time slots to transmit their packets. Second, in the analytical framework, as stated in Assumption 3.3.1, we assume distance-based ordering, instead of instantaneous received power-based ordering [128], at the UAV. This ignores the impact of small-scale fading and treats the closest device to the UAV as the device with the highest SINR. Thus, our assumption may not be true in severe fading environments. Nevertheless, as N_{A} and λ increases, the simulation results quickly approach the analytical results. Thus, in the following, we only present numerical results using the proposed analytical framework, due to its reasonable accuracy.

Fig. 3.3(b) presents the impact of N_{A} within the UAV serving zone on P_{sc} for different λ for a fixed number of time slots ($n_{\text{s}} = 20$) within a transmission frame with maximum latency of 10^{-3} s. We see that for fixed λ and n_{s}, when N_{A} increases, P_{sc} decreases. For a fixed number of time slots, when N_{A} within a

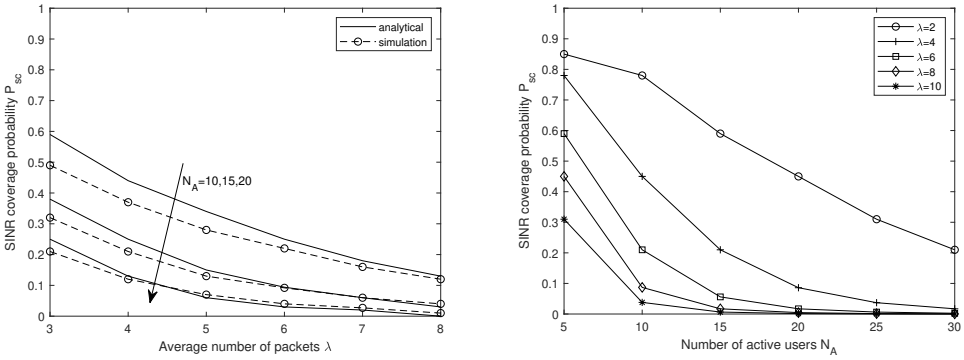

(a) P_{sc} vs. λ for different $N_{\text{A}} = 10, 15, 20$. (b) P_{sc} vs. N_{A} for different $\lambda = 2, 4, 6, 8, 10$.

Figure 3.3: The impact of the average number of users λ and number of active users N_{A} on the SINR coverage probability P_{sc} for a fixed number of time slots ($n_{\text{s}} = 20$) is presented in Figs. 3.3(a) and 3.3(b), respectively. In Fig. 3.3(a), the simulation and theoretical values are represented by dashed and solid lines, respectively. The gap in the results in Fig. 3.3(a) can be mainly attributed to the lower number of N_{A} and λ. It can be seen that the simulation results become asymptotically equivalent to theoretical results at higher N_{A} and λ. Thus, only analytical results are presented in Fig. 3.3(b).

transmission frame increases, the number of devices transmitting at a given time slot increases. This decreases the MUSA collision probability P_{cf} and increases the number of undecodable MUSA sequence collided devices. On the other hand, due to an increasing number of transmitting devices in the given time slot, the number of singleton devices also increases. As the devices are distributed within a fixed serving area and transmit with equal power, an increasing number of singleton devices implies a decrease in power disparity within the SIC decodable devices. This decreases the performance of the SIC receiver and decreases the P_{sc}. For a given N_{A}, when λ increases, P_{sc} decreases. When the number of packets generated by an active device increases, the probability that a given time slot is occupied by at least one device increases. This decreases P_{cf} and L_s in the time slot, and decreases P_{sc} as explained above. Furthermore, if the number of packets generated by a device exceeds the fixed number of available time slots, the excess packets are not transmitted to the UAV at all. This further decreases P_{sc} at the UAV.

Overall, it can be seen from Fig. 3.3(b) that for a fixed number of time slots,

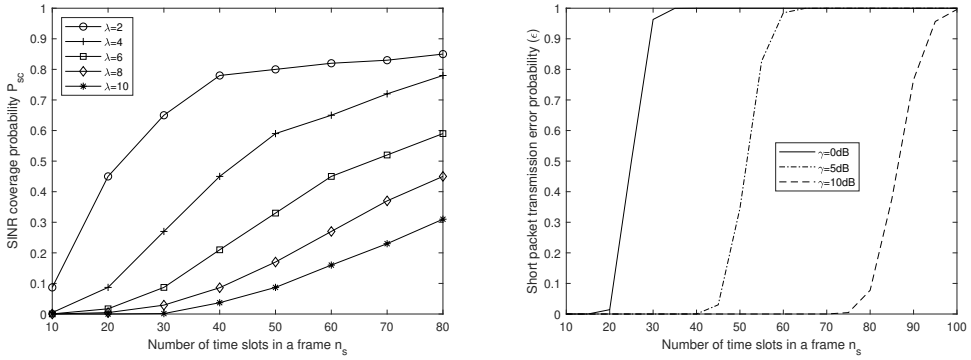

(a) SINR coverage probability P_{sc} vs. number of time slots n_{s} for different $\lambda = 2, 4, 6, 8, 10$.

(b) Short packet transmission error probability ϵ vs. number of time slots n_{s} for different $\gamma = 0, 5, 10$ dB.

Figure 3.4: Impact of number of time slots on the SINR coverage probability and short packet transmission error probability.

as the number of active devices and/or the number of packets generated by each active device increases, the SINR coverage probability is severely degraded. This illustrates the fact that under an EoI, the system reliability is severely degraded unless the UAV changes its operating mode to accommodate the change in traffic conditions by changing the number of time slots, as stated in Remark 3.1.

3.5.2 Impact of the Number of Time Slots

In this subsection, we investigate the impact of the number of time slots on the SINR coverage probability and the short packet transmission error probability.

Fig. 3.4(a) evaluates the impact on the number of time slots n_{s} for different λ for $N_{\text{A}} = 20$ within a transmission frame with the maximum latency of 10^{-3} s. We see that for a given λ, when n_{s} increases, P_{sc} increases. Similar trend is observed for all the values of λ. This is because when the number of time slots increases, the probability that a given time slot is occupied by more than one device decreases. As a result, the probability of MUSA collisions decreases and the number of singleton devices in a time slot decreases. When there are less singleton devices in a time slot, the performance of the SIC decoder increases. Thus, P_{sc} increases when n_{s} increases.

We also investigate the impact of number of time slots on short packet trans-

mission errors for the IoT-UAV transmission. We present the impact of the number of time slots n_{s} on the short packet transmission error probability ϵ for different SINRs γ in Fig. 3.4(b). We can see that for a given n_{s}, ϵ decreases when γ increases. Similarly, for a given γ, ϵ increases when n_{s} increases, as stated in Remark 3.3.

Overall, we see from Figs. 3.4(a) and 3.4(b) that there is a trade-off between P_{sc} and ϵ. Therefore, both P_{sc} and ϵ must be considered simultaneously to optimize the number of time slots n_{s} while maximizing the performance of the IoT-UAV communication. Given this, in the next subsection we will investigate the performance of the adaptive transmission scheme proposed in Section 3.4.

3.5.3 Proposed Scheme for Emergency Scenario

In this subsection, we first present the impact of severity of emergency scenario on the optimal number of time slots n_{s} in the transmission frame structure of the proposed adaptive transmission scheme. We then compare the performance of the IoT-UAV transmission achieved by the aforementioned transmission scheme with two benchmark schemes.

3.5.3.1 Impact of parameters on the optimal number of time slots

Fig. 3.5(a) shows how the optimal number of time slots $\widetilde{n_{\mathrm{s}}}$, varies with different average number of packets λ to be transmitted by an active device for $N_{\mathrm{A}} = 10, 20, 30$ active devices within the transmission frame. We see that for a given N_{A}, when λ increases, the optimal number of time slots $\widetilde{n_{\mathrm{s}}}$ increases gradually and then becomes stable after a certain λ. Moreover, at low λ, the optimal number of time slots $\widetilde{n_{\mathrm{s}}}$ has a higher value for higher N_{A}. This is because at low λ and N_{A}, when the severity of the emergency scenario is low; $\widetilde{n_{\mathrm{s}}}$ depends on $n_{\mathrm{s}\lambda}$ which is proportional to the total average of packets $N_{\mathrm{A}}\lambda$, while at high λ and N_{A}, when the severity of emergency scenario is high, $\widetilde{n_{\mathrm{s}}}$ is upper bounded by the reliability constraint associated with short packet transmission, as stated in Remark 3.4.

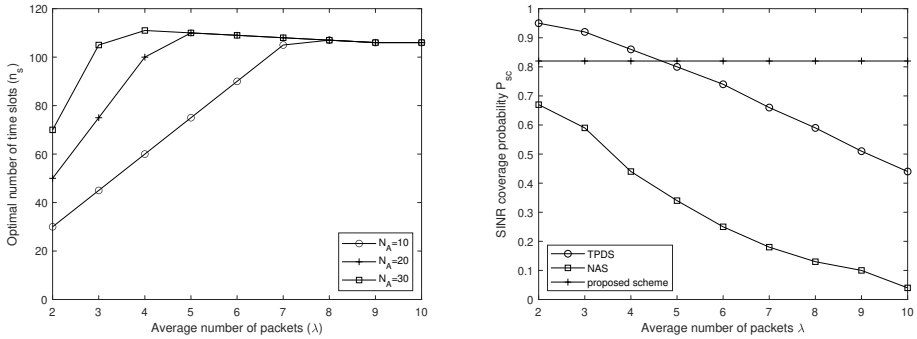

(a) Impact of λ and N_{A} on $\widetilde{n}_{\mathrm{s}}$ within a transmission frame in the proposed scheme.

(b) Performance comparison of TPDS, NAS and proposed schemes with a maximum latency of 10^{-3} s for $N_{\mathrm{A}} = 10$.

Figure 3.5: Impact of parameters on $\widetilde{n}_{\mathrm{s}}$ and performance comparison for the proposed scheme.

3.5.3.2 Comparison of the Proposed Scheme with Benchmark Schemes

We now present the performance of the proposed scheme in Section 3.4 and compare with two benchmarks, namely, transmit power diversity scheme (TPDS) and a non-adaptive scheme (NAS). In the TPDS, power diversity is introduced to improve the SIC decoding by assigning random transmit powers to active devices within the power budget[10]. In the TPDS, n_{s} remains fixed; however, the transmit power level of packets varies with the number of packets generated by a given device in a transmission frame. Suppose that the ith device has L_i packets and each packet transmits with an equal power of $\frac{P_{\max}}{L_i}$. Since L_i is a Poisson random variable, the transmit power of devices is random. In the NAS, neither the transmit power level nor the number of time slots changes with the number of packets generated by a user in a transmission frame.

Fig. 3.5(b) compares P_{sc} vs. λ for the proposed scheme, TPDS and NAS. In the proposed scheme, the maximum allowable latency and the short packet

[10]One alternative to introduce power diversity is to allocate different power levels to the packets of the same device. However, this implies that some packets have higher priority over others. In our system model, we assume that all the packets are equally important. Another alternative is to vary the transmit power of devices while assuming that all the devices transmitting in a particular time slot have the knowledge of device locations, number of packets, and time slot allocations of other devices. However, this requires the devices to communicate with each other. Therefore, to compare the performance of our proposed scheme, we choose the TPDS as the most appropriate power diversity-based benchmark scheme.

transmission error probability are constrained to 10^{-3} s and 10^{-5}, respectively. The results are presented for $N_{\mathrm{A}} = 10$ active devices. In Fig. 3.5(b), we see that both our scheme and the TPDS outperform the NAS. We then see that the TPDS outperforms the proposed scheme when λ is low, but then underperforms when λ increases. This is because that the TPDS randomizes the transmit power among devices by equally allocating $P_{\max}$ among the packets within the device. At low λ, the TPDS introduces enough power disparity between the transmitting devices in the time slot while maintaining a reasonable transmit power level.

At high λ, each packet of a given device is transmitted with a low transmit power, which decreases the SINR. Since the number of time slots remains unchanged in the TPDS, the MUSA collision probability increases and L_s in a time slot increases, both dominating the benefit of power diversity in the TPDS. We further see that the performance of the proposed scheme remains stable regardless of increase in λ, compared to the TPDS and NAS. This is due to the adaptable transmission frame structure of the proposed scheme which optimizes the number of time slots within a transmission frame according to the severity of the emergency scenario. Thus, the proposed scheme has superior reliability and stability in comparison to the state-of-the-art TPDS at moderate to high average traffic rates.

In the proposed scheme, all the devices transmit with fixed transmit power. According to Fig. 3.5(b), it is evident, that incorporating power diversity to the proposed scheme would improve the performance of the proposed scheme for low average traffic. Thus, future work may consider maximizing the SINR coverage probability of active devices under stringent reliability and latency constraints in EoI by jointly optimizing the transmission slot duration and transmit power of active devices within the transmission frame.

3.6 Summary

We propose a novel adaptive transmission scheme for a UAV-assisted IoT-based environmental monitoring network where IoT devices transmit heterogeneous traffic under specific reliability and latency requirements. We employed MUSA-based GF-NOMA and short packet transmission to enable high-reliability and low-latency IoT-UAV transmission. To establish the proposed adaptive transmission scheme,

we formulated an optimization problem to maximize the SINR coverage probability by optimizing the number of time slots in a transmission frame, subject to the short packet error constraint. Our results showed that, compared to benchmarks, the proposed scheme achieves superior reliability and stability at moderate to high average traffic rates while meeting the stringent low-latency constraints.

Chapter 4

Design and Performance Analysis of UAV-Assisted Maritime-LEO Satellite Communication Networks

To enable flexible coverage for low-end maritime users (MUs), such as buoys in remote ocean regions, we consider an UAV-assisted maritime-low earth orbit (LEO) satellite communication network. We assume that the low-end MUs are distributed in a finite ocean region that is outside the coverage region of onshore base stations (BSs) and transmit data to satellites via a swarm of relay UAVs hovering in a finite aerial region, leading to two transmission phases, i.e., (i) MU-to-UAV and (ii) UAV-to-satellite. By leveraging stochastic geometry and UAV-centric analysis in the uplink, we analyze the location-dependent performance and obtain the approximated yet accurate result for the success probability metric, which characterises the overall MU-to-UAV-to-satellite network performance. Our numerical results show that for a given set of satellite constellation parameters (e.g., number of satellites, height and beamwidth), there is an interplay between path loss and interference that determines the success probability. These results provide theoretical insights for the deployment and planning of integrated maritime-aerial-satellite networks to extend coverage for low-end MUs in remote ocean regions..

This Chapter is organized as follows. Section 4.1 details the system model, assumptions and the two-phase maritime-to-satellite communication scheme. Section 4.2 presents the analytical framework that is used to compute the success probability. Section 4.3 presents the results showing the impact of system parameters on the system performance. Finally, Section 4.4 concludes the Chapter.

4.1 System Model

4.1.1 Spatial Model of MUs and UAVs

We consider a UAV-assisted maritime-satellite communication network, where low-end MUs communicate with LEO satellites with the aid of aerial relays. In this network, we consider a set of MUs in a finite ocean region on the surface of the Earth, which are out of the coverage area of coastal BSs. We assume that the low-end MUs, such as buoys, have low antenna gains and low transmit power, lacking capability to directly communicate with LEO satellites. Thus, a swarm of UAVs are deployed at a fixed altitude above the mean sea level (MSL) to facilitate indirect communication between MUs and LEO satellites.

It is assumed that N_{M} MUs are independently and identically distributed (i.i.d.) in a finite ocean area defined by $\mathcal{C}_{\mathrm{M}} \equiv \mathbf{B}(O, R_{\mathrm{C}}) \subset \mathbb{R}^2$ of radius R_{C} centered at $O \equiv (0, 0, 0)$ on the Earth surface at the MSL, forming a Binomial Point process (BPP). A swarm of N_{U} UAVs are deployed at a fixed height H_U above the MSL in another disk $\mathcal{C}_{\mathrm{U}} \equiv \mathbf{B}(\acute{O}, R_{\mathrm{C}}) \subset \mathbb{R}^2$ of radius R_{C} centered at $\acute{O} \equiv (0, 0, H_U)$. As illustrated in Fig. 4.1(a), the distribution regions of MUs and UAVs can be visualized by a cylinder with centre O, radius R_{C}, and height H_U, where the UAVs are distributed on the top base of the cylinder and MUs are located on the bottom base of the cylinder.

We consider that UAVs follow spiral trajectories within $\mathcal{C}_{\mathrm{U}}$ to provide uniform coverage to MUs. It has been proven in the literature that statistical spiral trajectory processes can maintain the same coverage behavior as that of an uniform BPP [155]. Since UAVs are distributed in a finite area, the performance of UAVs depends on their locations. Thus, we consider that a reference UAV, U_0, is located at an arbitrary location $(x_0, H_U, 0)$ in $\mathcal{C}_{\mathrm{U}}$, where x_0 is the horizontal distance of U_0

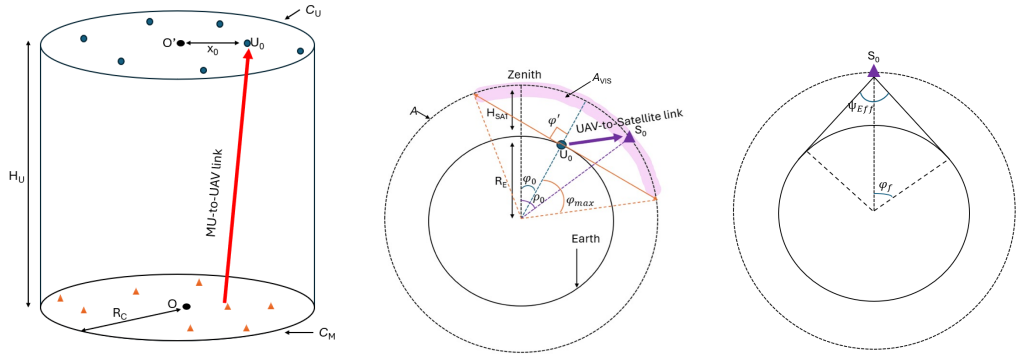

(a) (b) (c)

Figure 4.1: Network models for MU-to-UAV and UAV-to-Satellite communication links are presented in Figs. 4.1(a) and 4.1(b), respectively. Effective beamwidth ψ_{Eff} and ECZ angle φ_f corresponding to satellite footprint are depicted in Fig. 4.1(c).

from $\acute{O}$ along $x-$axis, and model the distribution of the remaining $N_{\mathrm{U}} - 1$ UAVs according to a BPP.

4.1.2 LEO Satellite Constellation Model

We consider a constellation of N_{S} LEO satellites at an altitude H_{Sat} above the MSL are homogeneously distributed on the surface of a sphere $\mathcal{A}$ with radius $H_{\mathrm{Sat}} + R_{\mathrm{E}}$, where R_{E} denotes the radius of the Earth. We denote the spherical coordinates of $\mathcal{A}$ by $\mathcal{A} = \{R_{\mathrm{E}} + H_{\mathrm{Sat}}, 0 \leq \varphi \leq \pi, 0 \leq \psi \leq 2\pi\}$, where φ and ψ represent the Earth-centered zenith (ECZ) angle and azimuthal angle, respectively. In order to preserve the homogeneity and independence overtime, similar to [108], we assume that each satellite follows a random orbit with radius $H_{\mathrm{Sat}} + R_{\mathrm{E}}$. Thus, we can approximate the location of satellites by a homogeneous PPP ϕ_S with intensity λ_S on $\mathcal{A}$.

From the satellite constellation perspective, the location of a reference UAV U_0 located at an arbitrary location $(x_0, H_U, 0)$ in $\mathcal{C}_{\mathrm{U}}$ can be reexpressed as $x_0 = R_{\mathrm{E}}\varphi_0$, where φ_0 is the ECZ angle of U_0. Moreover, for a UAV located at the Earth's zenith, i.e., $\varphi_0 = 0$, we consider that visible satellites, i.e., satellites that can potentially receive signals transmitted from the aforementioned UAV, are located

in a spherical cap $\mathcal{A}_{\text{VIS}} = \{R_{\text{E}}+H_{\text{Sat}}, 0 \leq \varphi \leq \varphi_{\max}, 0 \leq \psi \leq 2\pi\}$ where $\varphi_{\max}$ is the maximum ECZ angle below which the UAV can see satellites. This is illustrated in Fig. 4.1(b). φ can also be expressed using the users' zenith angle φ' which is given by [103]

$$\varphi = \cot^{-1}\left(\frac{\cot(\varphi' + \sqrt{\beta^2(1-\cot^2\varphi' - \beta^2)})}{1-\beta^2}\right) \tag{4.1}$$

where $\beta = \frac{R_{\text{E}}}{H_{\text{Sat}}+R_{\text{E}}}$. For $\varphi'_{\max} = \pi/2$, the maximum ECZ angle $\varphi_{\max}$ is given by

$$\varphi_{\max} = \cot^{-1}\left(\frac{\beta}{\sqrt{1-\beta^2}}\right). \tag{4.2}$$

Considering that the users' field of view is bounded by $\varphi' \in [0, \pi/2] \equiv \varphi \in [0, \varphi_{\max}]$, the area $\mathcal{A}_{\text{VIS}}$ is given as, $|\mathcal{A}_{\text{VIS}}| = 2\pi(R_{\text{E}} + H_{\text{Sat}})H_{\text{Sat}}$.

We define the effective beamwidth, ψ_{Eff}, as the minimum satellite-centred angle at which the satellite can provide connectivity. This is illustrated in Fig. 4.1(c). From a satellite's perspective, there exists a section of the Earth's surface, basically a spherical cap, representing the effective footprint. This spherical cap is bounded by an ECZ angle of $2\varphi_f$, where φ_f is the maximum ECZ angle which corresponds to the footprint boundary of a satellite. We further express ψ_{Eff} and φ_f, corresponding to the satellite footprint as [110]

$$\psi_{Eff} = \min\left[\psi_S, 2\arcsin\left(\beta\sin\left(\frac{\psi_U}{2}\right)\right)\right] \tag{4.3}$$

and

$$\varphi_f = \begin{cases} \arcsin\left(\frac{1}{\beta}\sin\left(\frac{\psi_{Eff}}{2}\right)\right) - \frac{\psi_{Eff}}{2}, & \text{if } \psi_{Eff} < \psi_S \\ \arccos(\beta), & \text{otherwise,} \end{cases} \tag{4.4}$$

respectively, where $\beta = \frac{R_{\text{E}}}{R_{\text{E}}+H_{\text{Sat}}}$. ψ_S and ψ_U correspond to the beamwidths of satellite and UAV, respectively.

4.1.3 Channel Model

We consider two types of communication links, namely, (i) MU-to-UAV and UAV-to-satellite, as follows:

The MU-to-UAV link is modeled as a combination of Euclidean distance-dependent large-scale path loss and small-scale Rician fading. Particularly, its path loss is modeled as $\eta_{\mathrm{m}}(r^2 + H_U^2)^{-\frac{\alpha_{\mathrm{m}}}{2}}$, where r, H_U, η_{m}, and α_{m} are the horizontal distance between a MU and UAV, height of UAV from the MSL, the path loss coefficient, and the path loss exponent for the MU-to-UAV link, respectively. For analytical tractability, Rician fading is approximated by setting $m_{\mathrm{M}} = \frac{(k+1)^2}{2k+1}$ in Nakagami-m fading, where m_{M} is the Nakagami fading parameter and k is the Rician fading parameter. Moreover, perfect line-of-sight (LoS) communication is assumed between MUs and UAVs, and MUs transmit to their corresponding associated UAVs with fixed transmit power $P_{\mathrm{T,M}}$.

The UAV-to-satellite link is also modeled as the Euclidean distance-dependent large-scale path loss $\eta_{\mathrm{S}} d^{-\alpha_{\mathrm{S}}}$, where d, η_{S}, and α_{S} are the Euclidean distance between UAV and satellite, the path loss coefficient, and the path loss exponent for the UAV-to-satellite link, respectively. Perfect LoS communication is assumed between UAVs and satellites, and small-scale fading is modeled using Nakagami-m fading with fading parameter m_{S}. We consider that UAVs transmit to the satellites with fixed transmit power $P_{\mathrm{T,U}}$.

4.1.4 Communication phases

We consider two communication phases: (i) MU-to-UAV transmission and (ii) UAV-to-satellite transmission. Moreover, we consider that the MU-to-UAV and UAV-to-satellite transmission phases are performed at orthogonal frequencies. Thus, there is no interference between these two communication phases. The communication phases are described as follows:

MU-to-UAV Communication Phase: In this phase, we consider that a reference UAV, U_0, is located at an arbitrary horizontal distance x_0 away from $\acute{O}$ in $\mathcal{C}_{\mathrm{U}}$, and receives a message by its closest MU, M_0, which is located at a horizontal distance t_0 from U_0 in a given time-frequency resource.

The transmission from M_0 to U_0 at a given time-frequency resource is considered

to be successful, if the SINR at U_0 exceeds a given threshold Θ_{M}. We assume that $N_{\mathrm{M}} \gg N_{\mathrm{U}}$, such that each UAV in $\mathcal{C}_{\mathrm{M}}$ has a transmit MU located within its Voronoi cell region. Hence, we can approximate the number of transmit MUs in $\mathcal{C}_{\mathrm{M}}$ as N_{U}, in a given time-frequency resource. Thus, the aggregate interference at U_0 is potentially generated by the other $N_{\mathrm{U}} - 1$ transmit MUs located within $\mathcal{C}_{\mathrm{M}}$. The successfully received message at U_0 is relayed to a satellite in the next phase.

UAV-to-Satellite Communication Phase: In this phase, we consider that U_0 relays its received message from M_0 to UAV's closest visible satellite S_0, which is located in $\mathcal{A}_{\mathrm{VIS}}$.

We consider that U_0 can be uniquely associated to S_0 if the following conditions are satisfied:

a) There must be least one satellite located in $\mathcal{A}_{\mathrm{VIS}}$ of U_0, and

b) Given S_0 is located within $\mathcal{A}_{\mathrm{VIS}}$, U_0 must be located within A_{foot} of S_0, and if more than one UAV is located within the Voronoi cell of S_0, S_0 must uniquely choose U_0 as its transmitting UAV.

Moreover, UAVs with successful MU-to-UAV transmissions in previous phase can transmit to a satellite in this phase, if it is uniquely associated with its closest satellite. Hence, we assume that the aggregate interference at S_0 is generated by other transmitting UAVs that are located within A_{foot} of S_0. Thus, the transmission from U_0 to S_0 is considered to be successful if the SINR of U_0 at S_0 exceeds a given threshold Θ_{S}.

Consequently, we consider that a transmission relayed by U_0 located at the ECZ angle φ_0 is successful if the following conditions are satisfied:

a) The SINR of transmission from M_0 at U_0 exceeds a given threshold Θ_{M},

b) Conditioned on a), U_0 is uniquely associated with its closest satellite S_0 and,

c) Conditioned on a) and b), the SINR of transmission from U_0 at S_0 exceeds a given threshold Θ_{S}.

4.1.5 Performance metric

We analyze the UAV-centric performance of the UAV-assisted maritime-to-satellite communication scheme[1] using stochastic geometry by adopting success probability as the performance metric, defined as follows:

Definition 4.1 *Conditioned on the location of U_0, defined by the ECZ angle $\varphi_0 = \frac{x_0}{R_\mathrm{E}}$, the success probability, denoted by $P_\mathrm{SUCC}(\varphi_0)$, is defined as the joint probability that (1) transmission from U_0's closest MU M_0 is received successfully at the U_0, denoted by $P^\mathrm{MU}_\mathrm{SINR}(\varphi_0 R_\mathrm{E})$, and (2) given condition (1) is satisfied, U_0 is uniquely associated with its closest satellite S_0, denoted by $P_\mathrm{Tag}(\varphi_0|P^\mathrm{MU}_\mathrm{SINR})$, and (3) given conditions (1) and (2) are satisfied, the transmission from the U_0 is successfully received by S_0, denoted by $P^\mathrm{SAT}_\mathrm{SINR}(\varphi_0|P^\mathrm{MU}_\mathrm{SINR} \cap P_\mathrm{Tag})$. Mathematically, the success probability is given by*

$$P_\mathrm{SUCC}(\varphi_0) = P^\mathrm{MU}_\mathrm{SINR}(\varphi_0 R_\mathrm{E}) P^\mathrm{SAT}_\mathrm{SUCC}(\varphi_0|P^\mathrm{MU}_\mathrm{SINR}), \tag{4.5}$$

where

$$P^\mathrm{SAT}_\mathrm{SUCC}(\varphi_0|P^\mathrm{MU}_\mathrm{SINR}) = P_\mathrm{Tag}(\varphi_0|P^\mathrm{MU}_\mathrm{SINR}) \times P^\mathrm{SAT}_\mathrm{SINR}(\varphi_0|P^\mathrm{MU}_\mathrm{SINR} \cap P_\mathrm{Tag}),$$

and $\varphi_0 = \frac{\delta R_\mathrm{C}}{R_\mathrm{E}}$ with $\delta \in (0, 1)$.

In the next Section, we derive relevant Lemmas and Propositions required to derive $P_\mathrm{SUCC}(\varphi_0)$ in (4.6).

4.2 UAV-CENTRIC ANALYTICAL FRAMEWORK

In this section, we conduct the UAV-centric performance analysis in a finite area by leveraging stochastic geometry to derive $P^\mathrm{MU}_\mathrm{SINR}(\varphi_0 R_\mathrm{E})$, $P_\mathrm{Tag}(\varphi_0|P^\mathrm{MU}_\mathrm{SINR})$, and $P^\mathrm{SAT}_\mathrm{SINR}(\varphi_0|P^\mathrm{MU}_\mathrm{SINR} \cap P_\mathrm{Tag})$ in Propositions 4.1, 4.2, and 4.3, respectively. Then, we use such results to compute $P_\mathrm{SUCC}(\varphi_0)$ in Theorem 4.1. The flowchart of Lemmas and Propositions used for the derivation of this theorem is illustrated in Fig. 4.2.

[1]Note that accounting for the spatial distribution of MUs, trajectories of UAVs relays in a finite regions, and satellite constellation parameters in the analytical framework, differentiates our proposed UAV-assisted maritime-to-satellite communication scheme from conventional terrestrial relay systems.

Since the UAVs are distributed in a finite aerial region which is modeled using a finite BPP, the performance of a UAV is location-dependent. This is due to that the aggregate interferences, signal-to-interference-noise ratios (SINRs), and association probabilities seen at the center of $\mathcal{C}_{\mathrm{U}}$ are different from those at the $\mathcal{C}_{\mathrm{U}}$ boundary. Thus, in this UAV-centric performance analysis, we evaluate the performance of the two communications phases with respect to a reference UAV, U_0, located at an arbitrary location in $\mathcal{C}_{\mathrm{U}}$.

4.2.1 Performance analysis of a MU-to-UAV link

First, we derive the expression for the probability that the transmission from U_0's closest MU, M_0, is received successfully at U_0 in the MU-to-UAV communication phase. Here, we consider that the transmission from M_0 to U_0 is successful if the corresponding SINR at U_0 is greater than Θ_{M}, and the corresponding probability is denoted by $P_{\mathrm{SINR}}^{\mathrm{MU}}$ and defined as follows[2]:

Definition 4.2 *Conditioned on the location of U_0, defined by the ECZ angle $\varphi_0 = \frac{x_0}{R_{\mathrm{E}}}$, the SINR coverage probability of M_0 at U_0, denoted by $P_{\mathrm{SINR}}^{\mathrm{MU}}(\varphi_0 R_{\mathrm{E}})$, is the probability that the SINR of M_0 at U_0 in the MU-to-UAV communication phase exceeds a given threshold Θ_{M}, and is given by*

$$P_{\mathrm{SINR}}^{\mathrm{MU}}(\varphi_0 R_{\mathrm{E}}) = \mathbb{P}\left(\mathrm{SINR}_{\mathrm{MU}} \geq \Theta_{\mathrm{M}}\right). \tag{4.6}$$

where $\mathrm{SINR}_{\mathrm{MU}} = \frac{P_{\mathrm{T,M}}\eta_{\mathrm{m}}\left(t_0^2+H_U^2\right)^{-\frac{\alpha_{\mathrm{m}}}{2}}h_0}{I_{\mathrm{M}}+\sigma_M^2}$. *$t_0$ and h_0 correspond to the distance between M_0 and U_0 and small-scale fading gain with Nakagami-m fading parameter m_{M}, respectively.*

Next, we present relevant Lemmas used in the subsequent derivations in this subsection, as illustrated in Fig. 4.2. Specifically, we characterize the distribution of the distance between any MU to U_0, that between the closest MU to U_0, and that between any interfering MU to U_0, in Lemmas 4.2.1, 4.2.2, and 4.2.3, respectively. Then, we present the Laplace transform of the interference at U_0 in Lemma 4.2.4.

[2]To avoid confusion, we denote $P_{\mathrm{SINR}}^{\mathrm{MU}}$ and $P_{\mathrm{SINR}}^{\mathrm{SAT}}$ as the SINR probability of M_0 at U_0 in the MU-to-UAV communication phase and SINR probability of U_0 at S_0 in the UAV-to-Satellite communication phase, respectively.

Lemma 4.2.1 *Conditioned on the location of U_0, which is defined by the horizontal distance x_0 from $\acute{O}$ on $\mathcal{C}_{\mathrm{U}}$, the CDF of horizontal distance W_i between any MU M_i for $i = 1, 2, \cdots, N_{\mathrm{M}}$ and U_0 is given by*

$$F_{W_i}(w, x_0) = \begin{cases} \frac{w^2}{R_{\mathrm{C}}^2}, & \text{if } 0 < w < |R_{\mathrm{C}} - x_0| \\ \frac{\mathbb{B}(w,x_0)}{\pi R_{\mathrm{C}}^2}, & \text{if } |R_{\mathrm{C}} - x_0| < w < |R_{\mathrm{C}} + x_0|, \end{cases} \tag{4.7}$$

where $W_i = \|x_0 - q_i\|$ and q_i denotes the horizontal distance of the ith MU from O in $\mathcal{C}_{\mathrm{M}}$, and $\mathbb{B}(w, x_0) = w^2\overline{\phi}(w, x_0) + R_{\mathrm{C}}^2\overline{\epsilon}(w, x_0)$, where $\phi(w, x_0) = \arccos\left(\frac{w^2+x_0^2-R_{\mathrm{C}}^2}{2wx_0}\right)$, $\epsilon(w, x_0) = \arccos\left(\frac{R_{\mathrm{C}}^2+x_0^2-w^2}{2R_{\mathrm{C}}x_0}\right)$, $\overline{\phi}(w, x_0) = \phi(w, x_0) - \frac{1}{2}\sin(2\phi(w, x_0))$, and $\overline{\epsilon}(w, x_0) = \epsilon(w, x_0) - \frac{1}{2}\sin(2\epsilon(w, x_0))$.

Proof

We perform the analysis on U_0 at an arbitrary location x_0 which is the horizontal distance of U_0 from origin $\acute{O}$ in $\mathcal{C}_{\mathrm{U}}$. Given, uniform BPP in $\mathcal{C}_{\mathrm{U}}$ is rotation variant around $\acute{O}$, we assume that the x-axis is aligned with the location of U_0. In this communication phase, we consider the closest transmitter selection policy where U_0 is associated with the closest transmitting MU located within its Voronoi cell. The proof is similar to that in [156], and is omitted here for brevity.

Lemma 4.2.2 *Conditioned on the location of U_0, which is defined by the horizontal distance x_0 from $\acute{O}$ on $\mathcal{C}_{\mathrm{U}}$, the PDF of the horizontal distance between U_0 and its closest MU M_0 (i.e., contact distance), denoted by t_0, is given by*

$$f_{t_0}(t|x_0) = \begin{cases} f_{t_0,1}(t|x_0), & \text{if } 0 < t < |R_{\mathrm{C}} - x_0| \\ f_{t_0,2}(t|x_0), & \text{if } |R_{\mathrm{C}} - x_0| < t < |R_{\mathrm{C}} - x_0|, \end{cases} \tag{4.8}$$

where $f_{t_0,1}(t|x_0)$ and $f_{t_0,2}(t|x_0)$ are given by

$$f_{t_0,1}(t|x_0) = N_{\mathrm{M}}\left(1 - \frac{t^2}{R_{\mathrm{C}}^2}\right)^{N_{\mathrm{M}}-1}\frac{2t}{R_{\mathrm{C}}^2} \tag{4.9}$$

and

$$f_{t_0,2}(t|x_0) = N_{\mathrm{M}}\left(1 - \frac{\mathbb{B}(t, x_0)}{\pi R_{\mathrm{C}}^2}\right)^{N_{\mathrm{M}}-1}\frac{2t}{\pi R_{\mathrm{C}}^2}\phi(t, x_0), \tag{4.10}$$

respectively, where $\mathbb{B}(t, x_0)$ *and* $\phi(t, x_0)$ *are defined below* (4.7).

Proof

Please refer to Appendix C.1.1.

Lemma 4.2.3 *Conditioned on the location of* U_0*, which is defined by the horizontal distance* x_0 *from Ó in* $\mathcal{C}_{\mathrm{U}}$*, and its contact distance* t_0*, the PDF of the horizontal distance between* U_0 *and any interfering MU, denoted by* V*, is given by*

$$f_V(v|t_0, x_0) = \begin{cases} \frac{2v}{R_{\mathrm{C}}^2 - t_0^2}, & \text{if } 0 \le t_0 \le v \le |R_{\mathrm{C}} - x_0| \\ \frac{2v\phi(v,x_0)}{\pi\left(R_{\mathrm{C}} - t_0^2\right)}, & \text{if } 0 \le t_0 \le |R_{\mathrm{C}}^2 - x_0| \le v \le R_{\mathrm{C}} + x_0 \\ \frac{2v\phi(v,x_0)}{\pi R_{\mathrm{C}}^2 - \mathbb{B}(t_0,x_0)}, & \text{if } |R_{\mathrm{C}} - x_0| \le t_0 \le v \le R_{\mathrm{C}} + x_0. \end{cases} \tag{4.11}$$

Proof

Please refer to Appendix C.1.2.

Next, to characterize the interference at U_0 in the MU-to-UAV communication phase, we compute the Laplace transform of interference I_{M}, conditioned on the location of U_0 and its contact distance t_0, in Lemma 4.2.4.

Lemma 4.2.4 *Conditioned on the location of* U_0*, which is defined by the horizontal distance* x_0 *from Ó in* $\mathcal{C}_{\mathrm{U}}$*, and its contact distance* t_0*, the Laplace transform of interference* I_{M} *at* s*, which is denoted as* $\mathcal{L}_{I_{\mathrm{M}}}(s|t_0, x_0)$*, is given by*

$$\mathcal{L}_{I_{\mathrm{M}}}(s|t_0, x_0) = \begin{cases} \left[\int_{t_0}^{|R_{\mathrm{C}}-x_0|} \vartheta_M(v,s)\frac{2v}{R_{\mathrm{C}}^2 - t_0^2}\mathrm{d}v + \int_{|R_{\mathrm{C}}-x_0|}^{R_{\mathrm{C}}+x_0} \vartheta_M(v,s)\frac{2v\phi(v,x_0)}{\pi\left(R_{\mathrm{C}}^2 - t_0^2\right)}\mathrm{d}v\right]^{N_{\mathrm{M}}-1}, & \text{if } 0 \ge t_0 \ge |R_{\mathrm{C}} \\ \left[\int_{t_0}^{R_{\mathrm{C}}+x_0} \vartheta_M(v,s)\frac{2v\phi(v,x_0)}{\pi R_{\mathrm{C}}^2 - \mathbb{B}(t_0,x_0)}\right]^{N_{\mathrm{M}}-1}, & \text{if } |R_{\mathrm{C}} - x_0| \ge \\ & t_0 \ge |R_{\mathrm{C}} + x_0|, \end{cases} \tag{4.12}$$

where $\vartheta_M(v,s) = \left(\frac{m_{\mathrm{M}}}{m_{\mathrm{M}} + s\eta_{\mathrm{m}} P_{\mathrm{T,M}}\left(v^2 + H_U^2\right)^{-\frac{\alpha_{\mathrm{m}}}{2}}}\right)^{m_{\mathrm{M}}}$ *and* m_{M} *is the Nakagami-m fading parameter for the MU-to-UAV communication phase.*

Proof

Please refer to Appendix C.1.3.

Finally, we present the SINR coverage probability for the MU-to-UAV communication phase in Proposition 4.1.

Proposition 4.1 *Conditioned on the location of U_0, which is defined by the horizontal distance x_0 from $\acute{O}$ in $\mathcal{C}_{\mathrm{U}}$, the SINR coverage probability of M_0 at U_0, denoted by $P_{\mathrm{SINR}}^{\mathrm{MU}}(x_0)$, which is defined as the as probability that SINR of M_0 at U_0 in the MU-to-UAV communication phase exceeds a given threshold Θ_{M}, is given by*

$$P_{\mathrm{SINR}}^{\mathrm{MU}}(x_0) = \int_0^{R_{\mathrm{C}}+x_0} \sum_{k=1}^{m_{\mathrm{M}}} \binom{m_{\mathrm{M}}}{k} (-1)^{k+1} \exp\left(-sk\sigma_M^2\right) \mathcal{L}_{I_{\mathrm{M}}}(sk|t_0, x_0) f_{t_0}(t|x_0) \mathrm{d}t, \tag{4.13}$$

where $\mathcal{L}_{I_{\mathrm{M}}}(sk|t_0, x_0)$ and $f_{t_0}(t|x_0)$, are given in (4.12) and (4.8), respectively.

Proof

Refer to Appendix C.1.4.

4.2.2 Performance analysis of a UAV-to-Satellite link

We first present the distribution of the ECZ angle between U_0 and S_0 in Lemma 4.2.5, which is used in the derivation of $P_{\mathrm{Tag}}(\varphi_0|P_{\mathrm{SINR}}^{\mathrm{MU}})$ in Proposition 4.2, as illustrated in Fig. 4.2.

Lemma 4.2.5 *Conditioned on the location of U_0, which is defined by an arbitrary ECZ angle $\varphi_0 = \delta\frac{R_{\mathrm{C}}}{R_{\mathrm{E}}}$, where $\delta \in (0, 1)$, the PDF of ECZ angle of U_0's closest satellite S_0, denoted by ρ_0, is given by*

$$f_{\rho_0}(\rho|\varphi_0) = \frac{N_{\mathrm{S}}}{2} \sin(\rho - \varphi_0) \exp\left(-\frac{N_{\mathrm{S}}}{2}(1 - \cos(\rho - \varphi_0))\right), \tag{4.14}$$

where $\rho \in \left[\varphi_0, \varphi_0 + \cot^{-1}\left(\frac{\beta}{\sqrt{1-\beta}}\right)\right]$ and $\beta = \frac{R_{\mathrm{E}}}{H_{\mathrm{Sat}}+R_{\mathrm{E}}}$.

Proof

Please refer to Appendix C.2.1.

Proposition 4.2 *Conditioned on the location of U_0, which is defined by the ECZ angle φ_0, the conditional UAV tag probability given the previous MU-to-UAV communication phase was successful, denoted by $P_{\mathrm{Tag}}(\varphi_0|P_{\mathrm{SINR}}^{\mathrm{MU}})$, is the probability that*

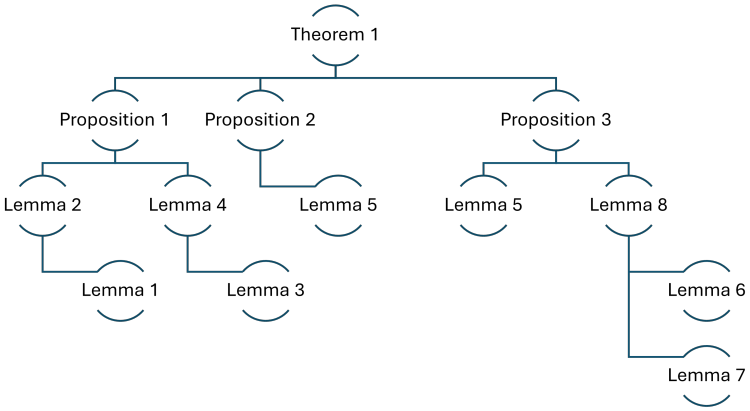

Figure 4.2: Flowchart of Lemmas and Propositions used for the derivation of Theorem 4.1.

U_0 is uniquely associated with its closest satellite S_0, and is given by

$$P_{\mathrm{Tag}}(\varphi_0|P_{\mathrm{SINR}}^{\mathrm{MU}}) = \underbrace{\left(1-\exp\left(-2\lambda_S\pi(R_{\mathrm{E}}+H_{\mathrm{Sat}})H_{\mathrm{Sat}}\right)\right)}_{P_{\mathrm{vis}}} \times \Bigg(\underbrace{\int_{\rho_{\max}}^{\rho_{\min}} \sum_{k=1}^{N_{\mathrm{U}}} \frac{1}{k}\binom{N_{\mathrm{U}}}{k}\left(\frac{A_{\mathrm{int}}(\rho|\varphi_0)}{A_{\mathrm{M}}}\right)^k \left(1-\frac{A_{\mathrm{int}}(\rho|\varphi_0)}{A_{\mathrm{M}}}\right)^{N_{\mathrm{U}}-k} \frac{N_{\mathrm{U}}}{2}\sin\left(\rho-\varphi_0\right)}_{P_{\mathrm{uniq}}} \times \underbrace{\exp\left(-\frac{N_{\mathrm{U}}}{2}\left(1-\cos\left(\rho-\varphi_0\right)\right)\right)\mathrm{d}\rho}_{P_{\mathrm{uniq}}} \Bigg), \tag{4.15}$$

where $A_{\mathrm{M}} = \pi R_{\mathrm{E}}^2\left(1-\cos\left(\frac{R_{\mathrm{C}}}{R_{\mathrm{E}}}\right)\right)$ and $|A_{\mathrm{int}}(\rho_0|\varphi_0)|$ is the intersecting area of maritime disk $\mathcal{C}_{\mathrm{M}}$ and footprint area A_{foot} of S_0, given by

$$|A_{\mathrm{int}}(\rho_0|\varphi_0)| = R_{\mathrm{C}}^2\arccos\left(\frac{d_1}{R_{\mathrm{C}}}\right) - d_1\sqrt{R_{\mathrm{C}}^2-d_1^2} + R_\mu^2\arccos\left(\frac{d_2}{R_\mu}\right) - d_2\sqrt{R_\mu^2-d_2^2}, \tag{4.16}$$

with $R_\mu = \min(R_{\mathrm{foot}}, R_{\mathrm{vor}})$, $R_{\mathrm{foot}} = R_{\mathrm{E}}\varphi_f$, $d_1 = \frac{R_{\mathrm{C}}^2-R_\mu^2+y_0^2}{2y_0}$, $d_2 = \frac{R_\mu^2-R_{\mathrm{C}}^2+y_0^2}{2y_0}$, and $y_0 = R_{\mathrm{E}}\rho_0$.

Proof

Please refer to Appendix C.2.2.

Next, we define the conditional SINR coverage probability of U_0 at S_0, denoted by $P^{\mathrm{SAT}}_{\mathrm{SINR}}(\varphi_0|P^{\mathrm{MU}}_{\mathrm{SINR}} \cap P_{\mathrm{Tag}})$, in Definition 4.3.

Definition 4.3 *The conditional SINR coverage probability of U_0 at S_0 given that the MU-to-UAV communication phase was successful and U_0 is uniquely associated with S_0, denoted by $P^{\mathrm{SAT}}_{\mathrm{SINR}}(\varphi_0|P^{\mathrm{MU}}_{\mathrm{SINR}} \cap P_{\mathrm{Tag}})$, is the probability that the SINR of U_0 at S_0 in the UAV-to-satellite communication phase exceeds a given threshold Θ_{S}. It is given by*

$$P^{\mathrm{SAT}}_{\mathrm{SINR}}(\varphi_0|P^{\mathrm{MU}}_{\mathrm{SINR}} \cap P_{\mathrm{Tag}}) = \mathbb{P}\left(\mathrm{SINR}_{\mathrm{SAT}} \geq \Theta_{\mathrm{S}}\right), \tag{4.17}$$

where $\mathrm{SINR}(\varphi_0) = \frac{P_{\mathrm{T,U}}\eta_{\mathrm{S}} d_0^{-\alpha_{\mathrm{S}}} h_0}{I_{\mathrm{U}}+\sigma_S^2}$, h_0 and σ_S^2 are small-scale fading gain with Nakagami-m parameter m_{S} and noise power, respectively, d_0 is the contact distance between U_0 and S_0, and I_{U} is the aggregate interference at S_0.

Now we present relevant Lemmas used for the derivation of $P^{\mathrm{SAT}}_{\mathrm{SINR}}(\varphi_0|P^{\mathrm{MU}}_{\mathrm{SINR}} \cap P_{\mathrm{Tag}})$ at S_0 for the UAV-to-satellite communication phase, as illustrated in Fig. 4.2. Specifically, we present the number of interfering UAVs at S_0, distance distribution between any interfering UAV and S_0, and Laplace transform of interference at S_0 in Lemmas 4.2.6, 4.2.7, and 4.2.8, respectively. Then, we derive $P^{\mathrm{SAT}}_{\mathrm{SINR}}(\varphi_0|P^{\mathrm{MU}}_{\mathrm{SINR}} \cap P_{\mathrm{Tag}})$ in Proposition 4.3.

Lemma 4.2.6 *Conditioned on the location of U_0, which is defined by the ECZ angle φ_0, the number of interfering UAVs at S_0, denoted by $N_{\mathrm{U,int}}$, is given by*

$$N_{\mathrm{U,int}}(\varphi_0) = \frac{\sum_{k=1}^{N_{\mathrm{U}}} P^k_{\mathrm{act}}}{\pi R_{\mathrm{C}}^2} \int_{\rho_{\min}}^{\rho_{\max}} |A_{\mathrm{I}}(\rho,\varphi_0)| \frac{N_{\mathrm{S}}}{2} \sin(\rho-\varphi_0) \exp\left(-\frac{N_{\mathrm{U}}}{2}(1-\cos(\rho-\varphi_0))\right) \mathrm{d}\rho, \tag{4.18}$$

where $|A_{\mathrm{I}}(\rho,\varphi_0)| = R_{\mathrm{C}}^2 \arccos\left(\frac{c_1}{R_{\mathrm{C}}}\right) - c_1\sqrt{(R_{\mathrm{C}}^2-c_1^2)} + R_{\mathrm{foot}}^2 \left(\frac{c_2}{R_{\mathrm{foot}}}\right) - c_2\sqrt{(R_{\mathrm{foot}}^2-c_2^2)} - \left(R_{\mathrm{C}}^2 \arccos\left(\frac{c_3}{R_{\mathrm{C}}}\right) - c_3\sqrt{(R_{\mathrm{C}}^2-c_3^2)} + R_{\mathrm{vor}}^2\left(\frac{c_4}{R_{\mathrm{vor}}}\right) - c_4\sqrt{(R_{\mathrm{vor}}^2-c_4^2)}\right)$, $c_1 = \frac{R_{\mathrm{C}}^2-R_{\mathrm{foot}}^2+y_0^2}{2y_0}$, $c_2 = \frac{R_{\mathrm{foot}}^2-R_{\mathrm{C}}^2+y_0^2}{2y_0}$, $c_3 = \frac{R_{\mathrm{C}}^2-R_{\mathrm{vor}}^2+y_0^2}{2y_0}$, *and* $c_4 = \frac{R_{\mathrm{vor}}^2-R_{\mathrm{C}}^2+y_0^2}{2y_0}$.

Proof

Please refer to Appendix C.2.3.

Lemma 4.2.7 *Conditioned on the location of reference UAV U_0, which is defined by the ECZ angle φ_0, the CDF and PDF of the distance distribution between S_0 and interfering UAVs located within A_{foot} are given by*

$$F_{z_0}(z) = \frac{1}{|A_{\text{I}}(\rho_0|\varphi_0)|}\left(R_{\text{C}}^2 \arccos\left(\frac{b_1}{R_{\text{C}}^2}\right) - b_1\sqrt{\left(R_{\text{C}}^2 - b_1^2\right)} + z^2 \arccos\left(\frac{b_2}{z}\right) - b_2\sqrt{\left(z^2 - b_2^2\right)}\right.$$
$$\left. - \left(R_{\text{C}}^2 \arccos\left(\frac{b_3}{R_{\text{C}}^2}\right) - b_3\sqrt{\left(R_{\text{C}}^2 - b_3^2\right)} + R_{\text{vor}}^2 \arccos\left(\frac{b_4}{R_{\text{vor}}}\right) - b_4\sqrt{\left(R_{\text{vor}}^2 - b_4^2\right)}\right)\right) \tag{4.19}$$

and

$$f_{z_0}(z) = \frac{\mathrm{d}}{\mathrm{d}z}F_{z_0}(z), \tag{4.20}$$

respectively, where $b_1 = \frac{R_{\text{C}}^2 - z^2 + y_0^2}{2y_0}$, $b_2 = \frac{z^2 - R_{\text{C}}^2 + y_0^2}{2y_0}$, $b_3 = \frac{R_{\text{C}}^2 - R_{\text{vor}}^2 + y_0^2}{2y_0}$, $b_4 = \frac{R_{\text{vor}}^2 - R_{\text{C}}^2 + y_0^2}{2y_0}$, and $|A_{\text{I}}(\rho_0|\varphi_0)|$ is given in Lemma 4.2.6.

Proof

Please refer to Appendix C.2.4.

Lemma 4.2.8 *Conditioned on the location of U_0, which is defined by the ECZ angle φ_0 and the location of S_0 defined by ρ_0, the Laplace transform of aggregate interference I_{U} at s, denoted by $\mathcal{L}_{I_{\text{U}}}(s|\rho_0, \varphi_0)$ is given by*

$$\mathcal{L}_{I_{\text{U}}}(s|\rho_0, \varphi_0) = \left[\int_{R_{\text{vor}}}^{R_{\text{foot}}} \left(\frac{m_{\text{S}}}{m_{\text{S}} + sP_{\text{T,U}}\eta_{\text{S}}\left(z^2 + H_{\text{Sat}}^2\right)^{-\frac{\alpha_{\text{S}}}{2}}}\right)^{m_{\text{S}}} f_{z_0}(z)\mathrm{d}z\right]^{N_{\text{U,int}}}, \tag{4.21}$$

where R_{foot} and R_{vor}, correspond to the footprint radius and Voronoi cell radius of S_0, respectively. $N_{\text{U,int}}$ and $f_{z_0}(z)$ are presented in Lemmas 4.2.6 and 4.2.7, respectively.

Proof

Please refer to Appendix C.2.5.

Proposition 4.3 *Conditioned on the location of U_0, which is defined by the ECZ angle φ_0, the conditional SINR coverage probability of U_0 at its tagged satellite S_0, given that the previous MU-to-UAV communication phase was successful and U_0 is*

uniquely associated with S_0, is defined as the probability that the SINR of U_0 at S_0 exceeds a given threshold Θ_{S}, denoted by $P_{\mathrm{SINR}}^{\mathrm{SAT}}(\varphi_0|P_{\mathrm{SINR}}^{\mathrm{MU}} \cap P_{\mathrm{Tag}})$. It is given by

$$P_{\mathrm{SINR}}^{\mathrm{SAT}}(\varphi_0|P_{\mathrm{SINR}}^{\mathrm{MU}} \cap P_{\mathrm{Tag}}) = \int_{\rho_{\min}}^{\rho_{\max}} \sum_{j=1}^{m_{\mathrm{S}}} \binom{m_{\mathrm{S}}}{j} (-1)^{j+1} \exp\left(-sj\sigma_S^2\right) \mathcal{L}_{I_{\mathrm{U}}}\left(sj|\rho,\varphi_0\right) \frac{N_{\mathrm{S}}}{2} \sin\left(\rho-\varphi_0\right) \exp\left(-\frac{N_{\mathrm{S}}}{2}\left(1-\cos\left(\rho-\varphi_0\right)\right)\right) \mathrm{d}\rho, \tag{4.22}$$

where $s = \frac{\Theta_{\mathrm{S}}\varepsilon_S}{P_{\mathrm{T,U}}\eta_{\mathrm{S}} d_0^{-\alpha_{\mathrm{S}}}}$, $\varepsilon_S = m_{\mathrm{S}}\left(m_{\mathrm{S}}!\right)^{-\frac{1}{m_{\mathrm{S}}}}$, $d_0 = \sqrt{((R_{\mathrm{E}}+H_{\mathrm{Sat}})^2 - 2R_{\mathrm{E}}(R_{\mathrm{E}}+H_{\mathrm{Sat}})\cos\left(\rho-\varphi_0\right))}$, $\rho_{\min} = \varphi_0$, and $\rho_{\max} = \varphi_0 + \theta_{\max}$, and $\mathcal{L}_{I_{\mathrm{U}}}\left(sj|\rho,\varphi_0\right)$ is obtained using Lemma 4.2.8.

Proof

Please refer to Appendix C.2.6.

Next, we define the success probability of the UAV-to-SAT communication phase in Definition 4.4.

Definition 4.4 *The conditional success probability of U_0 at S_0 given that the previous MU-to-UAV communication phase was successful, denoted by $P_{\mathrm{SUCC}}^{\mathrm{SAT}}(\varphi_0|P_{\mathrm{SINR}}^{\mathrm{MU}})$, is the conditional joint probability that U_0 is associated with its closest satellite S_0, denoted by $P_{\mathrm{Tag}}(\varphi_0|P_{\mathrm{SINR}}^{\mathrm{MU}})$, and the SINR of U_0 at S_0 exceeds a given threshold Θ_{S}, denoted by $P_{\mathrm{SINR}}^{\mathrm{SAT}}(U_0|P_{\mathrm{SINR}}^{\mathrm{MU}} \cap P_{\mathrm{Tag}})$. It is given by*

$$P_{\mathrm{SUCC}}^{\mathrm{SAT}}\left(\varphi_0|P_{\mathrm{SINR}}^{\mathrm{MU}}\right) = P_{\mathrm{Tag}}\left(\varphi_0|P_{\mathrm{SINR}}^{\mathrm{MU}}\right) P_{\mathrm{SINR}}^{\mathrm{SAT}}\left(U_0|P_{\mathrm{SINR}}^{\mathrm{MU}} \cap P_{\mathrm{Tag}}\right), \tag{4.23}$$

where $P_{\mathrm{Tag}}\left(\varphi_0|P_{\mathrm{SINR}}^{\mathrm{MU}}\right)$ and $P_{\mathrm{SINR}}^{\mathrm{SAT}}\left(\varphi_0|P_{\mathrm{SINR}}^{\mathrm{MU}} \cap P_{\mathrm{Tag}}\right)$ are given in Propositions 4.2 and 4.3, respectively.

Finally, we present the following theorem to characterize the overall performance of both the MU-to-UAV and UAV-to-satellite communication phases in Theorem 4.1, as illustrated in Fig. 4.2.

Theorem 4.1 *According to Definition 4.1, conditioned on the location of U_0, defined by the ECZ angle $\varphi_0 = \frac{x_0}{R_{\mathrm{E}}}$, the success probability, denoted by $P_{\mathrm{SUCC}}(\varphi_0)$, is defined as the probability that the transmission to U_0 from its closest MU M_0 is*

Table 4.1: Parameter values for numerical and simulation results.

Parameter	Symbol	Value	Parameter	Symbol	Value
Maritime disk radius	R_{C}	1000 km	Earth radius	R_{E}	6378 km
UAV altitude	H_U	125 m	Satellite altitude	H_{Sat}	550 km
MU transmit power	$P_{\mathrm{T,M}}$	10 mW	UAV transmit power	$P_{\mathrm{T,U}}$	1 W
MU-UAV path loss coefficient	η_{m}	1	UAV-Satellite path loss coefficient	η_S	1
MU-UAV path loss exponent	α_{m}	2	UAV-Satellite path loss exponent	α_{S}	2
MU-UAV noise power	σ_M^2	-100 dBm	UAV-Satellite noise power	σ_S^2	-100 dBm
MU-UAV Rician fading	k_{M}	10	UAV-Satellite Nakagami-m fading parameter	m_{S}	5
MU-UAV threshold	Θ_{M}	0 dB	UAV-Satellite threshold	Θ_{S}	0 dB
UAV beamwidth	ψ_U	2π	Satellite beamwidth	ψ_S	$\frac{\pi}{2}$

successfully relayed to its closest satellite S_0, which is given by

$$P_{\mathrm{SUCC}}(\varphi_0) = P_{\mathrm{SINR}}^{\mathrm{MU}}(\varphi_0 R_{\mathrm{E}}) P_{\mathrm{SUCC}}^{\mathrm{SAT}}(\varphi_0 | P_{\mathrm{SINR}}^{\mathrm{MU}}), \tag{4.24}$$

where $\varphi_0 = \frac{\delta R_{\mathrm{C}}}{R_{\mathrm{E}}}$ with $\delta \in (0,1)$, $P_{\mathrm{SINR}}^{\mathrm{MU}}(\varphi_0 R_{\mathrm{E}})$ and $P_{\mathrm{SUCC}}^{\mathrm{SAT}}(\varphi_0 | P_{\mathrm{SINR}}^{\mathrm{MU}})$ are given in Proposition 4.1 and Definition 4.4, respectively.

4.3 Numerical Results

In this section, we evaluate the performance of the proposed UAV-assisted maritime-satellite communication network. For validating models and assessing the impact of important parameters on the performance, we examine the MU-to-UAV and the UAV-to-satellite communication phases separately. This rationale for doing so is two-fold: (i) Many parameters exert independent effects on the two phases and (ii) The performance of each communication phase significantly contributes to the overall system performance. We also evaluate the overall performance.

The analytical results are obtained using (4.13) for the MU-to-UAV communication phase, (4.15) and (4.22) for the UAV-to-satellite communication phase, and (4.24) for the overall performance. The simulation results are obtained using system level Matlab simulations where we average 10^5 Monte Carlo simulation runs. The values of the parameters used for the results are summerized in Table 4.1, which are consistent with other relevant studies in the literature [97, 157, 158]. For results generation, we assume that both the MU-to-UAV and the UAV-to-satellite communication channels are always LoS.

4.3.1 MU-to-UAV Communication: Model Validation

We first present model validation results in Fig. 4.3 for the MU-to-UAV communication phase using the SINR probability $P_{\text{SINR}}^{\text{MU}}$ at the reference UAV U_0 as a function of distance of U_0, which is related to $\delta = \frac{x_0}{R_{\text{C}}}$ and defined as the ratio between the horizontal distance of U_0 from $\acute{O}$, denoted by x_0, and the radius of maritime disk region $\mathcal{C}_{\text{M}}$, denoted by R_{C}.

Fig. 4.3 plots the SINR coverage probability $P_{\text{SINR}}^{\text{MU}}$ at U_0 as a function of its distance from the origin δ, for a given number of UAV relays N_{U} in $\mathcal{C}_{\text{U}}$. The results are presented for $N_{\text{U}} = 10, 20, 30$ UAVs with $\delta = 0.1, \cdots, 0.9$, where $\delta = 0.1$ means that U_0 is located closer to $\acute{O}$, and $\delta = 0.9$ means that U_0 is located closer to $\mathcal{C}_{\text{U}}$ boundary. First, we observe that $P_{\text{SINR}}^{\text{MU}}$ increases when δ increases for a given N_{U}. This is because that this work considers a realistic deployment of MUs and UAVs, where MUs and UAVs are distributed in a finite ocean area as opposed to a homogeneous distribution around the surface of the Earth. As a result, when the distance of U_0 from $\acute{O}$ increases, the overall distance from interfering MUs to U_0 increases, leading to decreased aggregate interference at U_0. Here, we note that the aggregate interference is higher when U_0 is closer to $\acute{O}$, but lower when it is closer to $\mathcal{C}_{\text{U}}$ boundary. Second, we observe that both analytical and simulation results present the same trends as δ increases for $N_{\text{U}} = 10, 20, 30$. We further observe that the gap between simulation and analytical results decreases as N_{U} increases. This is because that in the analytical framework, we assume the interfering MUs at U_0 being located beyond the circular Voronoi region, instead of being located further than the closest MU M_0 from U_0. As a result, the aggregate interference in our analysis is slightly lower compared to that in our simulation. The impact of this assumption becomes negligible as N_{U} increases. Thus, in the following subsection, we only present numerical results using the proposed analytical framwork for the MU-to-UAV communication phase.

4.3.2 MU-to-UAV Communication: Impact of Parameters

Fig. 4.4(a) plots $P_{\text{SINR}}^{\text{MU}}$ versus the number of UAVs, N_{U}, at different locations of U_0, $\delta = 0.1, 0.5, 0.9$. We see that for a given N_{U}, $P_{\text{SINR}}^{\text{MU}}$ is higher at larger δ, as expected. For a given δ, $P_{\text{SINR}}^{\text{MU}}$ decreases as N_{U} increases. This is because that more

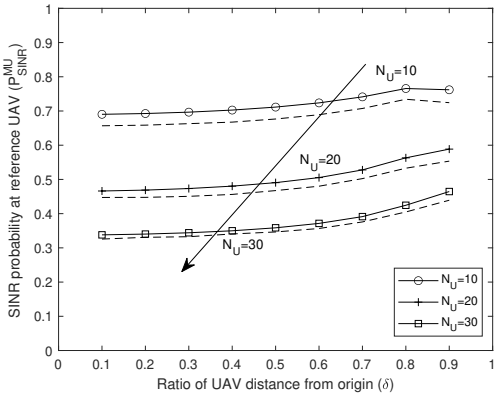

Figure 4.3: $P^{\mathrm{MU}}_{\mathrm{SINR}}$ vs. δ for different N_{U} for MU-to-UAV communication phase. The distance x_0 of U_0 from $\acute{O}$ is related to δ, where $\delta = 0$ and $\delta = 1$ correspond to center and boundary of A_{M}, respectively. The simulation results are plotted by dashed lines and analytical results are plotted by markers.

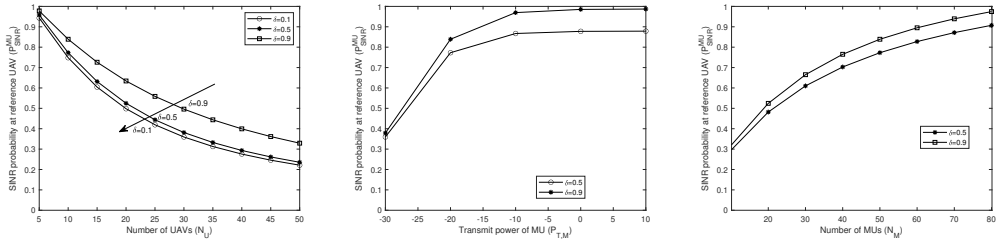

(a) $P^{\mathrm{MU}}_{\mathrm{SINR}}$ vs. N_{U} for different δ.

(b) $P^{\mathrm{MU}}_{\mathrm{SINR}}$ vs. $P_{\mathrm{T,M}}$ for different δ.

(c) $P^{\mathrm{MU}}_{\mathrm{SINR}}$ vs. N_{M} for different δ.

Figure 4.4: Impact of number of UAVs, N_{U}, transmit power of MUs, $P_{\mathrm{T,M}}$, and the number of MUs, N_{M}, on $P^{\mathrm{MU}}_{\mathrm{SINR}}$ of the MU-to-UAV communication phase.

MUs can transmit in $\mathcal{C}_{\mathrm{M}}$ when more UAVs are available. Thus, there is more severe interference at U_0, which decreases SINR and $P^{\mathrm{MU}}_{\mathrm{SINR}}$. We note that the values of $P^{\mathrm{MU}}_{\mathrm{SINR}}$ at $\delta = 0.1$ and 0.5 are similar to each other, as the area region of interference, depicted in Fig. C.1(b), is similar in both cases. Thus, we only present the results at $\delta = 0.5, 0.9$ in Figs. 4.4(b) and 4.4(c).

Fig. 4.4(b) shows the impact of transmit power of MUs, $P_{\mathrm{T,M}}$, on $P^{\mathrm{MU}}_{\mathrm{SINR}}$ for two arbitrary locations of U_0, $\delta = 0.5, 0.9$. We see that for a given $P_{\mathrm{T,M}}$, $P^{\mathrm{MU}}_{\mathrm{SINR}}$ is higher at $\delta = 0.9$, i.e., $\mathcal{C}_{\mathrm{U}}$ boundary, compared to that at $\delta = 0.5$, i.e., closer to $\acute{O}$, which is due to the lack of aggregate interference near the boundary. For a given

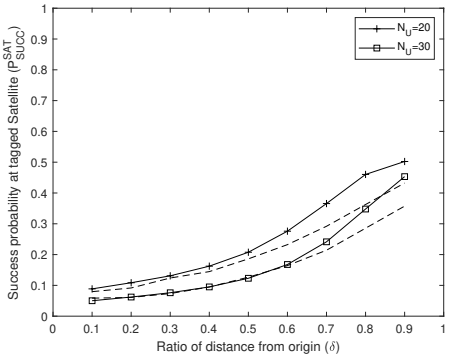

(a) $P^{\mathrm{SAT}}_{\mathrm{SUCC}}$ vs. δ for different N_{U}.

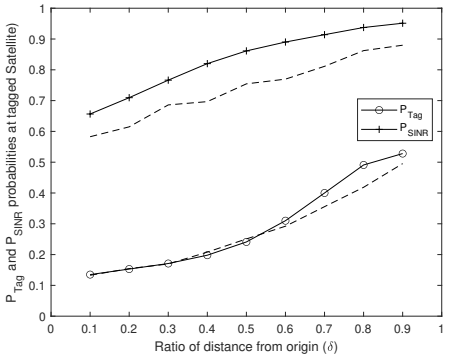

(b) $P^{\mathrm{SAT}}_{\mathrm{SINR}}$ and P_{Tag}, vs. δ for $N_{\mathrm{U}} = 20$.

Figure 4.5: Analytical and simulation results for $P^{\mathrm{SAT}}_{\mathrm{SUCC}}$, $P^{\mathrm{SAT}}_{\mathrm{SINR}}$, and P_{Tag} vs. δ for different N_{U}. The simulation results are plotted by dashed lines and analytical results are plotted by markers.

δ, $P^{\mathrm{MU}}_{\mathrm{SINR}}$ increases at low $P_{\mathrm{T,M}}$, and then becomes steady at higher $P_{\mathrm{T,M}}$. This is because that at low $P_{\mathrm{T,M}}$, increasing $P_{\mathrm{T,M}}$ increases the quality of the desired link, which in turn improves SINR. However, at high $P_{\mathrm{T,M}}$, when $P_{\mathrm{T,M}}$ increases, the interference power also increases, as there is no uplink power control. Hence, when $P_{\mathrm{T,M}}$ is very high, the interference dominates and stabilizes the SINR at U_0.

Fig. 4.4(c) plots $P^{\mathrm{MU}}_{\mathrm{SINR}}$ versus N_{M}, at different $\delta = 0.5, 0.9$. For a given δ, when N_{M} increases, the number of MUs within the Voronoi cell of U_0 increases, the contact distance decreases, and the path loss for the desired link at U_0 decreases. Since N_{U} is unchanged, the number of interfering MUs at U_0 remains unchanged. Thus, the SINR at U_0 increases as N_{M} increases.

4.3.3 UAV-to-Satellite Communication: Model Validation

We first present model validation results in Figs. 4.5(a) and 4.5(b) using $P^{\mathrm{SAT}}_{\mathrm{SUCC}}$, P_{Tag}, and $P^{\mathrm{SAT}}_{\mathrm{SINR}}$ at a reference UAV U_0 as a function of the ECZ angle of U_0, which is related to $\delta = \frac{\varphi_0 R_{\mathrm{E}}}{R_{\mathrm{C}}}$, as defined in Section 4.3.1.

Fig. 4.5(a) plots the success probability, $P^{\mathrm{SAT}}_{\mathrm{SUCC}}$, at U_0 as a function of its location δ for $N_{\mathrm{U}} = 20, 30$. We observe that both analytical and simulation results present a similar trend as δ increases. Analytical results are generally higher than simulation results, but the gap decreases when N_{U} increases and when U_0 is located

closer to the origin. Due to the approximation made in analysis, when N_{U} is low, the number of interfering UAVs is also low. Therefore, for lower N_{U}, even a small gap in the number of interfering UAVs can cause a large gap in $P_{\mathrm{SUCC}}^{\mathrm{SAT}}$. Similarly, the number of interfering UAVs is lower at higher δ, leading to a gap between analytical and simulation results near the boundary.

To further examine this gap, we plot P_{Tag} and $P_{\mathrm{SINR}}^{\mathrm{SAT}}$ for $N_{\mathrm{U}} = 20$ in Fig. 4.5(b). We observe that both P_{Tag} and $P_{\mathrm{SINR}}^{\mathrm{SAT}}$ contribute to the gap in $P_{\mathrm{SUCC}}^{\mathrm{SAT}}$. Particularly, the gap in P_{Tag} is very small, and both analytical and simulation results follow a similar trend for all values of δ. The small gap in P_{Tag} can be attributed to the following approximations made in the analysis when deriving P_{Tag}: (i) We approximate the shape and area of the Voronoi cell of S_0 using a disk of radius R_{vor} and (ii) when calculating the number of potentially associated UAVs at S_0, we approximate the footprint and Voronoi cell areas of S_0 as flat disks. Although these approximations make our analytical framework tractable, the areas of A_{vor} and A_{foot} in reality must be modeled as curved surfaces of two cones while accounting for curvature of the Earth.

As depicted in Fig. 4.5(b), the noticeable gap in $P_{\mathrm{SUCC}}^{\mathrm{SAT}}$ comes mainly from $P_{\mathrm{SINR}}^{\mathrm{SAT}}$. For all values of δ, the simulation results are lower than the analytical results. This can be attributed to assumptions and approximations made when calculating the number of interfering UAVs at S_0 in $P_{\mathrm{SINR}}^{\mathrm{SAT}}$. In the analytical framework, we use P_{Tag} to compute the probabilistic number of transmitting UAVs in $\mathcal{C}_{\mathrm{U}}$, and then assume that transmitting UAVs are uniformly distributed in $\mathcal{C}_{\mathrm{U}}$ to allow analytical tractability. However, in reality, P_{Tag} is distance-dependent and the intensity of transmitting UAVs is lower near $\acute{O}$ but higher near the boundary. Thus, the analytical framework computes an average number of interfering UAVs at S_0, leadinbg to the gap in numerical results. Despite so, the analytical results in Fig. 4.5(a) match reasonably well with simulation results. In the following subsection, we only present numerical results using the proposed analytical framework, due to its reasonable accuracy.

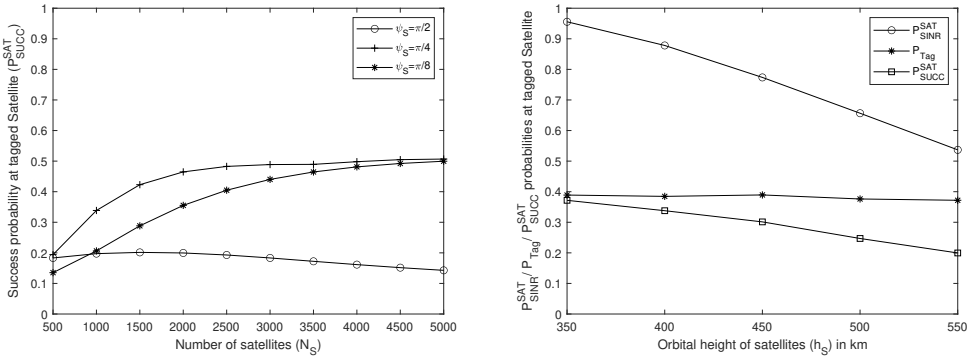

(a) $P^{\text{SAT}}_{\text{SUCC}}$ vs. N_{S} for different $\psi_{Eff} = \frac{\pi}{2}, \frac{\pi}{4}, \frac{\pi}{8}$.

(b) $P^{\text{SAT}}_{\text{SINR}}$ and P_{Tag}, vs. H_{Sat}.

Figure 4.6: Impact of effective beamwidth, ψ_{Eff}, the number of satellite, N_{S}, and satellite orbital height, H_{Sat}, on $P^{\text{SAT}}_{\text{SUCC}}$, $P^{\text{SAT}}_{\text{SINR}}$, and P_{Tag} of the UAV-to-satellite communication phase.

4.3.4 UAV-to-Satellite Communication: Impact of Parameters

Fig. 4.6(a) examines the impact of the number of satellites, N_{S}, and effective beamwidth, ψ_{Eff}, on $P^{\text{SAT}}_{\text{SUCC}}$. Specifically, we plot $P^{\text{SAT}}_{\text{SUCC}}$ as a function of N_{S} for $\psi_{Eff} = \frac{\pi}{2}, \frac{\pi}{4}, \frac{\pi}{8}$ with $N_{\text{U}} = 20$ at $\delta = 0.5$. At larger ψ_{Eff}, e.g., $\psi_{Eff} = \frac{\pi}{2}$, we see that $P^{\text{SAT}}_{\text{SUCC}}$ increases slightly at low $N_{\text{S}} = 500$, and starts to decline slightly thereafter. This is because that $A_{\text{foot}} < A_{\text{vor}}$ at $N_{\text{S}} = 500$. In the analysis, we consider that interfering UAVs at S_0 are located within the intersecting area of interference given by $A_{\text{foot}} \bigcap \overline{(A_{\text{vor}})}$ within $\mathcal{C}_{\text{U}}$. When $A_{\text{foot}} < A_{\text{vor}}$, the interference at S_0 is minimum. Thus, $P^{\text{SAT}}_{\text{SUCC}}$ at $N_{\text{S}} = 500$ is slightly higher compared to that of $N_{\text{S}} > 500$. At $\psi_{Eff} = \frac{\pi}{4}$, we see that $P^{\text{SAT}}_{\text{SUCC}}$ increases up to approximately $N_{\text{S}} = 3500$ and stabilizes thereafter. This is because $A_{\text{foot}} < A_{\text{vor}}$ up to $N_{\text{S}} = 3500$; thus, P_{Tag} remains almost the same. Although the intersecting area of interference remains minimum, when N_{S} increases, the contact angle between U_0 and S_0 decreases, which in turn increases $P^{\text{SAT}}_{\text{SINR}}$ and causes $P^{\text{SAT}}_{\text{SUCC}}$ to increase. For $N_{\text{S}} > 3500$, $A_{\text{foot}} > A_{\text{vor}}$ and the intersecting area of interference at S_0 begins to increase. This also decreases the contact angle and decreases the path loss of the desired link. Due to the interplay between decreased path loss and increased interference, $P^{\text{SAT}}_{\text{SINR}}$

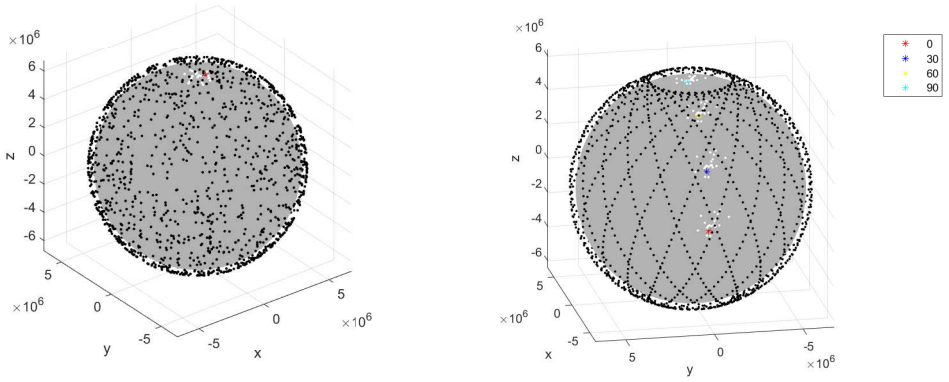

(a) HPPP constellation model.

(b) Starlink constellation with different locations of $\mathcal{C}_{\mathrm{U}}$ characterized by the latitude of $\acute{O}$.

Figure 4.7: Geometric modeling of HPPP constellation in Fig. 4.7(a) and Starlink constellation modeled using the Walker-Delta constellation model in Fig. 4.7(b). The location of U_0 at $\delta = 0.5$ is represented by asterisk in both figures, while the distribution of rest of the UAVs distributed in $\mathcal{C}_{\mathrm{U}}$ at different latitudes are represented by white dots.

decreases slightly, causing $P_{\mathrm{SUCC}}^{\mathrm{SAT}}$ to stabilize at higher N_{S}. At lower ψ_{Eff}, e.g., $\psi_{Eff} = \frac{\pi}{8}$, $A_{\mathrm{vor}} > A_{\mathrm{foot}}$ for all N_{S}. Thus, both P_{Tag} and $P_{\mathrm{SINR}}^{\mathrm{SAT}}$ increase when N_{S} increases, causing $P_{\mathrm{SUCC}}^{\mathrm{SAT}}$ to increase.

Fig. 4.6(b) plots P_{Tag}, $P_{\mathrm{SINR}}^{\mathrm{SAT}}$, and $P_{\mathrm{SUCC}}^{\mathrm{SAT}}$ versus the satellite orbital height, H_{Sat}, at $\delta = 0.5$ for $N_{\mathrm{U}} = 20$ and $N_{\mathrm{S}} = 2000$. We see that P_{Tag} is unaffected by H_{Sat} for a fixed number of satellites and UAVs. However, $P_{\mathrm{SINR}}^{\mathrm{SAT}}$ decreases as H_{Sat} increases. This can be attributed to several factors. First, as H_{Sat} increases, path loss increases and the SINR at S_0 decreases. Second, for a given ψ_{Eff}, when H_{Sat} increases, the footprint area increases and the interference at S_0 increases, causing $P_{\mathrm{SINR}}^{\mathrm{SAT}}$ to decrease. Thus, $P_{\mathrm{SUCC}}^{\mathrm{SAT}}$ decreases as H_{Sat} decreases.

4.3.5 Overall performance

We now examine the overall location-dependent performance for MU-to-UAV-to-satellite communication. Specifically, we consider different locations of $\mathcal{C}_{\mathrm{U}}$, characterized by the latitude of the center of $\mathcal{C}_{\mathrm{U}}$, denoted by $\acute{O}$. The MU and UAV

Table 4.2: P_{SUCC} at $\delta = 0.5, 0.9$ for HPPP and Starlink satellite constellation models for different locations of $\mathcal{C}_{\mathrm{U}}$ specified by latitudes.

HPPP: Latitude	**Analytical results with $\delta = 0.5$**	**Analytical results with $\delta = 0.9$**
0, 30, 60, 90	0.1589	0.3425
Starlink: Latitude	**Simulation results with $\delta = 0.5$**	**Simulation results with $\delta = 0.9$**
0	0.0542	0.0928
30	0.1776	0.2829
60	0.1597	0.4123
90	0	0

deployment locations are characterized by the latitude of $\acute{O}$, which is the center of $\mathcal{C}_{\mathrm{U}}$. For analytical results, the HPPP satellite constellation is modeled using $N_{\mathrm{S}} = 2000$. We also compare the analytical results, obtained using P_{SUCC} in Theorem 4.1, with simulation results for a practical (deterministic) satellite constellation modeled using the Walker delta constellation with inclination of 70 deg, $N_{\mathrm{S}} = 2000$, distributed in 20 planes. For both constellations, we consider $H_{\mathrm{Sat}} = 350$ km, $N_{\mathrm{U}} = 20$, and rest of relevant parameters values are consistent with Table 4.1. The geometric models of HPPP and Starlink constellations are shown in Fig. 4.7(a) and Fig. 4.7(b), respectively.

Table 4.2 presents the overall performance results for 0 (i.e., corresponding to the Equator), 30, 60, and 90 (i.e., corresponding to the North pole) latitudes for $\delta = 0.5$ and 0.9. For analytical results, since satellites are homogeneously distributed on the surface of a sphere for a HPPP constellation model, P_{SUCC} is the same for all latitudes. As expected, we see that the performance of practical constellation is latitude-dependent [112]. Specifically, P_{SUCC} reaches the highest value at latitude= 60, due to the higher availability of satellites, whereas P_{SUCC} reduces to zero at the North pole due to the absence of satellites. For both constellations, P_{SUCC} is higher at $\delta = 0.9$ than at $\delta = 0.5$, as expected. We see that for $\delta = 0.5$, the analytical results match very well with the simulation results for latitudes 30 and 60. For $\delta = 0.9$, the analytical results are an average of the results for latitudes 30 and 60.

4.4 Summary

In this work, we considered a UAV-assisted maritime-satellite communication network, where low-end MUs distributed in a finite ocean region communicate with LEO satellites via a swarm of UAV relays hovering in a finite aerial region. We proposed a two-phase communication scheme where a reference UAV located at an arbitrary location is served by its closest MU in the MU-to-UAV communication phase, and the received data is relayed to its closest satellite in the UAV-to-satellite communication phase. We created a UAV-centric location dependent performance analytical framework using the finite area stochastic geometry by adopting success probability as the performance metric. The results show that for a given set of satellite constellation parameters, there is an interplay between path loss and interference, which impacts the success probability. The results also provided theoretical guidance for deploying and planning integrated maritime-aerial-satellite networks in remote ocean regions.

Chapter 5

Conclusions and Future Research Directions

In this chapter, we present the broad conclusions derived from this thesis. Additionally, we identify several prospective avenues for future research that have emerged from our findings.

5.1 Conclusions

In Chapter 2, we focused on the coexistence of an AUE with a paired TUE in a cellular network. We assumed that the AUE flies in a given trajectory path and transmits to the BS periodically. To facilitate the concurrent uplink transmissions of the AUE and the TUE, we used an aerial-terrestrial NOMA scheme with SIC at the BS. We formulated an analytical framework that evaluates the rate coverage probability of each user and the system, at each transmission point on the trajectory. The numerical results showed that, for the spiral trajectory, the rate coverage probabilities decrease as the target data rate of the AUE increases and the AUE moves away from the BS. We also found the minimum height of AUE at each trajectory point in order to meet a QoS of 90% for different built-up environments. In the spiral trajectory, it was observed that the minimum height increases as the environmental parameters become more severe and when AUE moves towards the cell edge. For the trajectory model adopted from the 3GPP study, it was observed

that the minimum height increases and decreases depending on the distance of AUE from the BS.

In Chapter 3, we proposed a novel adaptive transmission scheme for a UAV-assisted IoT-based environmental monitoring network where IoT devices transmit heterogeneous traffic under specific reliability and latency requirements. We employed MUSA-based GF-NOMA and short packet transmission to enable high-reliability and low-latency IoT-UAV transmission. To establish the proposed adaptive transmission scheme, we formulated an optimization problem to maximize the SINR coverage probability by optimizing the number of time slots in a transmission frame, subject to the short packet error constraint. Our results showed that, compared to benchmarks, the proposed scheme achieves superior reliability and stability at moderate to high average traffic rates while meeting the stringent low-latency constraints.

In Chapter 4, we considered a UAV-assisted maritime-satellite communication network, where low-end MUs, distributed in a finite ocean region, communicate with LEO satellites via a swarm of UAV relays hovering in a finite aerial region. We considered a two-phase communication scheme where a reference UAV located at an arbitrary location is served by its closest MU in the MU-to-UAV communication phase, and the received data is relayed to its closest satellite in the UAV-to-satellite communication phase. We proposed a UAV-centric location-dependent performance analytical framework using the finite area stochastic geometry, where the success probability was adopted as the performance metric. The results showed that for a given set of satellite constellation parameters, there is an interplay between path loss and interference, which impacts the success probability. The results also provided theoretical guidance for deploying and planning integrated maritime-aerial-satellite networks in remote ocean regions.

5.2 Future Works

This section highlights potential research trajectories, inspired by the findings of each research work presented in this thesis, which may serve as focal points for future research endeavors.

5.2.1 Research Work 1:

Future work may consider challenging extensions such as a general case of multi-cell scenarios involving multiple UAVs per cell and non-orthogonal resource block allocation, taking inter-cell interference [35,159,160], practical base station antenna patterns and beamforming models into account [161]. In particular, with practical down-tilted antenna patterns at terrestrial BSs, the uplink signal from AUEs in neighboring cells might become non-negligible. In this case, it is beneficial to pair an active TUE of the serving cell with an AUE from a neighboring cell. It is important to note that our proposed methodology is still applicable in this case. With regards to the multiple AUE scenario, the AUEs may be orthogonally paired with TUEs in the cell, while accounting for orthogonal resource allocation for TUEs and orthogonal AUE-TUE pairing protocols. While our proposed methodology is still applicable in this case, the derivation of the location of the paired TUE of a given AUE must account for the resource allocation and pairing protocols, and the corresponding performance analysis may be considered in future work.

5.2.2 Research Work 2:

In the proposed scheme, all the devices transmit with fixed transmit power. According to Fig. 3.5(b), it is evident, that incorporating power diversity to the proposed scheme would improve the performance of the proposed scheme for low average traffic. Thus, future work may consider maximizing the SINR coverage probability of active devices under stringent reliability and latency constraints in EoI by jointly optimizing the transmission slot duration and transmit power of active devices within the transmission frame.

5.2.3 Research Work 3:

Unlike terrestrial environments, the atmosphere above sea level exhibits uneven distribution due to seawater evaporation. As a result, the maritime-aerial and maritime-satellite channels are impacted by tidal waves, temperature, humidity and wind speed [89]. Furthermore, when accounting for high-end maritime users such as powerful ships with realistic antenna patterns, antenna parameters such as

height and angle may change with the fluctuating sea level. Thus, future work may consider conducting performance analysis under these channel conditions. However, it should be noted that due to the complexity of these channel models, it may be challenging to conduct tractable performance analysis. In RW3, we considered a scenario which is limited to low-end MUs such as buoys. Future work may consider a consider a heterogeneous maritime network where low-end MUs coexist with high-end MUs such as powerful ships, and conduct performance analysis on the scenario where high-end MUs transmit directly to the satellites, while low-end MUs indirectly transmit to satellites using UAV relays. Performance analysis using finite area stochastic geometry could be conducted by modeling the mobility or shipping routes of high-end MUs using suitable stochastic processes, employing NOMA techniques to enhance spectral efficiency and suitable multiuser detection techniques at the satellites for signal decoding.

Appendix A

This appendix contains the proofs needed in Chapter 2.

A.1 Proof of Lemma 2.3.1

The horizontal distance r_{T} between the active TUE and BS at the time of transmission follows an uniform distribution due to the fact that x_{T} and y_{T} are uniformly distributed in the circular cell. Thus, the pdf of r_{T} is $f_{r_{\mathrm{T}}}(r) = \frac{2r}{R^2}$. The 3D distance d_{T} between the BS and TUE is given by $d_{\mathrm{T}} = \sqrt{h_{\mathrm{BS}}^2 + R^2}$. Therefore, the pdf of d_{T} is derived as

$$f_{d_{\mathrm{T}}}(z) = \frac{dr}{dz} f_{r_{\mathrm{T}}}(r) = \frac{d(\sqrt{z^2 - h_{\mathrm{BS}}^2})}{dz} f_{r_{\mathrm{T}}}(\sqrt{z^2 - h_{\mathrm{BS}}^2}) = \frac{z}{\sqrt{z^2 - h_{\mathrm{BS}}^2}} \frac{2\sqrt{z^2 - h_{\mathrm{BS}}^2}}{R^2} = \frac{2z}{R^2}. \tag{A.1}$$

A.2 Proofs of Lemmas 2.3.2 and 2.3.3

In this appendix, we provide proofs of Lemmas 2.3.2 and 2.3.3.

A.2.1 Proof of Lemma 2.3.2

The CDF of ψ_{T} can be written as

$$F_{\psi_{\mathrm{T}}}(x) = \mathbb{P}_{d_{\mathrm{T}}, H_{\mathrm{T}}} \left(P_{\mathrm{T}} d_{\mathrm{T}}^{-\alpha_{\mathrm{T}}} H_{\mathrm{T}} G_{\mathrm{T}} < x \right) = \mathbb{E}_{d_{\mathrm{T}}} \left[\mathbb{P} \left(H_{\mathrm{T}} < \frac{x}{P_{\mathrm{T}} d_{\mathrm{T}}^{-\alpha_{\mathrm{T}}} G_{\mathrm{T}}} \right) \right]$$

$$= \mathbb{E}_{d_{\mathrm{T}}}\left[1 - \exp\left(\frac{x}{P_{\mathrm{T}} d_{\mathrm{T}}^{-\alpha_{\mathrm{T}}} G_{\mathrm{T}}}\right)\right] \tag{A.2a}$$

$$= 1 - \int_{h_{\mathrm{BS}}}^{\sqrt{{h_{\mathrm{BS}}}^2 + R^2}} \exp\left(\frac{-x}{\rho_{\mathrm{T}} z^{\alpha_{\mathrm{T}}} z^{-\alpha_{\mathrm{T}}} G_{\mathrm{T}}}\right)\left(\frac{2z}{R^2}\right) dz = 1 - \exp\left(\frac{-x}{\rho_{\mathrm{T}} G_{\mathrm{T}}}\right), \tag{A.2b}$$

where (A.2a) comes from the fact that H_{T} follows an exponential distribution. (A.2b) is the expectation with respect to d_{T}, where $P_{\mathrm{T}} = \rho_{\mathrm{T}} z^{-\alpha_{\mathrm{T}}}$ and $f_{d_{\mathrm{T}}}(z) = \frac{2z}{R^2}$. Taking the derivative of $F_{\psi_{\mathrm{T}}}(x)$ with respect to x we obtain its PDF.

A.2.2 Proof of Lemma 2.3.3

The CDF of ψ_{A} can be expressed as

$$F_{\psi_{\mathrm{A}}}(x) = \mathbb{P}_{H_{\mathrm{A}}, d_{\mathrm{A}}}\left(P_{\mathrm{A}}\zeta_{\mathrm{A}}\ H_{\mathrm{A}} G_{\mathrm{A}} < x\right) = \mathbb{E}_{d_{\mathrm{A}}}\left[\mathbb{P}\left(H_{\mathrm{A}} < \frac{x}{P_{\mathrm{A}}\zeta_{\mathrm{A}} G_{\mathrm{A}}}\right)\right]$$

$$= \mathbb{E}_{d_{\mathrm{A}}}\Bigg[1 - \mathbb{P}_{\mathrm{LoS}} \sum_{i=0}^{m_{\mathrm{L}}-1} \left(\frac{m_{\mathrm{L}} x}{P_{\mathrm{A}}\eta_{\mathrm{L}} {d_{\mathrm{A}}}^{-\alpha_{\mathrm{L}}} G_{\mathrm{A}}}\right)^i \frac{1}{i!} \exp\left(\frac{-m_{\mathrm{L}} x}{P_{\mathrm{A}}\eta_{\mathrm{L}} {d_{\mathrm{A}}}^{-\alpha_{\mathrm{L}}} G_{\mathrm{A}}}\right) \tag{A.3a}$$

$$- (1 - \mathbb{P}_{\mathrm{LoS}}) \sum_{j=0}^{m_{\mathrm{N}}-1} \left(\frac{m_{\mathrm{N}} x}{P_{\mathrm{A}}\eta_{\mathrm{N}} {d_{\mathrm{A}}}^{-\alpha_{\mathrm{N}}} G_{\mathrm{A}}}\right)^j \frac{1}{j!} \exp\left(\frac{-m_{\mathrm{N}} x}{P_{\mathrm{A}}\eta_{\mathrm{N}} {d_{\mathrm{A}}}^{-\alpha_{\mathrm{N}}} G_{\mathrm{A}}}\right)\Bigg]$$

$$= 1 - \mathbb{P}_{\mathrm{LoS}} \sum_{i=0}^{m_{\mathrm{L}}-1} \frac{(\beta_{\mathrm{L}} x)^i}{i!} \exp(-\beta_{\mathrm{L}} x) - (1 - \mathbb{P}_{\mathrm{LoS}}) \sum_{j=0}^{m_{\mathrm{N}}-1} \frac{(\beta_{\mathrm{N}} x)^j}{j!} \exp(-\beta_{\mathrm{N}} x), \tag{A.3b}$$

where (A.3a) comes from the fact that H_{A} follows a Gamma distribution with parameters m_{L} and m_{N} for LoS and NLoS A2C channel link respectively. Also, note that the expectation in (A.3a) is a constant due to the fact that d_{A} is a deterministic variable. $f_{\psi_{\mathrm{A}}}(x)$ can be derived by taking the derivative of $F_{\psi_{\mathrm{A}}}(x)$ with respect to x.

A.3 Proofs of Propositions 2.1 and 2.2

In this appendix, we provide the proofs of Propositions 2.1 and 2.2.

A.3.1 Proof of Proposition 2.1

The rate coverage probability P_1 can be expressed as

$$
\begin{aligned}
P_1 &= \mathbb{P}_{\psi_\mathrm{A},\psi_\mathrm{T}}\left(\frac{\psi_\mathrm{T}}{\sigma^2} \geq \theta_\mathrm{T}, \frac{\psi_\mathrm{A}}{\psi_\mathrm{T}+\sigma^2} \geq \theta_\mathrm{A}\right) \\
&= \mathbb{E}_{\psi_\mathrm{T}}\left[\mathbb{P}_{\psi_\mathrm{A}}\left(t \geq \theta_\mathrm{T}\sigma^2, \psi_\mathrm{A} \geq \theta_\mathrm{A}(t+\sigma^2)\right)\right] && \text{(A.4a)} \\
&= \int_{\theta_\mathrm{T}\sigma^2}^{\infty} \mathbb{P}_{\psi_\mathrm{A}}\left(\psi_\mathrm{A} \geq \theta_\mathrm{A}(t+\sigma^2)\right) f_{\psi_\mathrm{T}}(t)dt && \text{(A.4b)} \\
&= \int_{\theta_\mathrm{T}\sigma^2}^{\infty} \mathbb{P}\left(H_\mathrm{A} \geq \frac{\theta_\mathrm{A}(t+\sigma^2)}{P_\mathrm{A}\zeta_\mathrm{A}G_\mathrm{A}}\right) f_{\psi_\mathrm{T}}(t)dt \\
&= \int_{\theta_\mathrm{T}\sigma^2}^{\infty} \Bigg(\mathbb{P}_\mathrm{LoS} \sum_{i=0}^{m_\mathrm{L}-1} \frac{(\beta_\mathrm{L}\theta_\mathrm{A})^i}{i!}\left(t+\sigma^2\right)^i \exp\left(-\beta_\mathrm{L}\theta_\mathrm{A}(t+\sigma^2)\right) \\
&+ (1-\mathbb{P}_\mathrm{LoS}) \sum_{j=0}^{m_\mathrm{N}-1} \frac{(\beta_\mathrm{N}\theta_\mathrm{A})^j}{i!}\left(t+\sigma^2\right)^j \exp\left(-\beta_\mathrm{N}\theta_\mathrm{A}(t+\sigma^2)\right)\Bigg) f_{\psi_\mathrm{T}}(t)dt && \text{(A.4c)} \\
&= \mathbb{P}_\mathrm{LoS} \sum_{i=0}^{m_\mathrm{L}-1} \frac{(\beta_\mathrm{L}\theta_\mathrm{A})^i}{i!} \frac{1}{\rho_\mathrm{T}G_\mathrm{T}} \exp\left(\frac{\sigma^2}{\rho_\mathrm{T}G_\mathrm{T}}\right)\left(\beta_\mathrm{L}\theta_\mathrm{A} + \frac{1}{\rho_\mathrm{T}G_\mathrm{T}}\right)^{-i-1} \\
&\times \Gamma\left(i+1, \frac{(1+\theta_\mathrm{T})(1+\beta_\mathrm{L}\theta_\mathrm{A}\rho_\mathrm{T}G_\mathrm{T})\sigma^2}{\rho_\mathrm{T}G_\mathrm{T}}\right) + (1-\mathbb{P}_\mathrm{LoS}) \sum_{j=0}^{m_\mathrm{N}-1} \frac{(\beta_\mathrm{N}\theta_\mathrm{A})^j}{j!} \frac{1}{\rho_\mathrm{T}G_\mathrm{T}} \exp\left(\frac{\sigma^2}{\rho_\mathrm{T}G_\mathrm{T}}\right) \\
&\times \left(\beta_\mathrm{N}\theta_\mathrm{A} + \frac{1}{\rho_\mathrm{T}G_\mathrm{T}}\right)^{-j-1} \Gamma\left(j+1, \frac{(1+\theta_\mathrm{T})(1+\beta_\mathrm{N}\theta_\mathrm{A}\rho_\mathrm{T}G_\mathrm{T})\sigma^2}{\rho_\mathrm{T}G_\mathrm{T}}\right). && \text{(A.4d)}
\end{aligned}
$$

In (A.4a) we consider that t denotes a random variable with distribution $f_{\psi_\mathrm{T}}(t)$ and it is a constant with respect to the random variable ψ_A. Expectation with respect to t, and lower and upper boundaries of t are applied in (A.4b). (A.4c) comes from the fact that the fading of AUE has a Gamma distribution and, (A.4d) is obtained by integrating (A.4c) with respect to t. Finally, (2.12) can be derived by substituting $\mu = \rho_\mathrm{T}G_\mathrm{T}$ into (A.4d).

A.3.2 Proof of Proposition 2.2

The rate coverage probability P_2 can be expressed as

$$
\begin{aligned}
P_2 &= \mathbb{P}_{\psi_{\mathrm{A}},\psi_{\mathrm{T}}}\left(\frac{\psi_{\mathrm{T}}}{\sigma^2} < \theta_{\mathrm{T}}, \frac{\psi_{\mathrm{A}}}{\psi_{\mathrm{T}}+\sigma^2} \geq \theta_{\mathrm{A}}\right) = \mathbb{E}_{\psi_{\mathrm{T}}}\left[\mathbb{P}_{\psi_{\mathrm{A}}}\left(t < \theta_{\mathrm{T}}\sigma^2, \psi_{\mathrm{A}} \geq \theta_{\mathrm{A}}(t+\sigma^2)\right)\right] \\
&= \int_0^{\theta_{\mathrm{T}}\sigma^2} \mathbb{P}_{\psi_{\mathrm{A}}}\left(\psi_{\mathrm{A}} \geq \theta_{\mathrm{A}}(t+\sigma^2)\right) f_{\psi_{\mathrm{T}}}(t)dt \\
&= \int_0^{\theta_{\mathrm{T}}\sigma^2} \Bigg(\mathbb{P}_{\mathrm{LoS}} \sum_{i=0}^{m_{\mathrm{L}}-1} \frac{(\beta_{\mathrm{L}}\theta_{\mathrm{A}})^i}{i!}\left(t+\sigma^2\right)^i \exp\left(-\beta_{\mathrm{L}}\theta_{\mathrm{A}}(t+\sigma^2)\right) \qquad \text{(A.5a)} \\
&\quad + (1-\mathbb{P}_{\mathrm{LoS}}) \sum_{j=0}^{m_{\mathrm{N}}-1} \frac{(\beta_{\mathrm{N}}\theta_{\mathrm{A}})^j}{i!}\left(t+\sigma^2\right)^j \exp\left(-\beta_{\mathrm{N}}\theta_{\mathrm{A}}(t+\sigma^2)\right) \Bigg) f_{\psi_{\mathrm{T}}}(t)dt, \qquad \text{(A.5b)}
\end{aligned}
$$

where the derivation of $P_{\psi_{\mathrm{A}}}(\theta_{\mathrm{A}}(t+\sigma^2))$ in (A.5a) is same as that in (A.4). (2.13) can be obtained by integrating (A.5b) with respect to t.

Appendix B

This appendix contains the proofs needed in Chapter 3.

B.1 Proof of Lemma 3.3.4

The Laplace transform of I_{s} can be written as

$$\mathcal{L}_{I_{\mathrm{s}}}(s) = \mathbb{E}_{I_{\mathrm{s}}}\left[\exp(-sI_{\mathrm{s}})\right] = \mathbb{E}_{r,h}\left[\exp\left(-s\sum_{i\in\phi_s}\overline{\mathrm{P}}\eta(r_i^2+H_{\mathrm{U}}^2)^{-\frac{\alpha}{2}}h_i\right)\right] \tag{B.1a}$$

$$= \mathbb{E}_{\phi_s}\left[\prod_{i\in\phi_s}\mathbb{E}_h\left[\exp(-s\overline{\mathrm{P}}\eta(r_i^2+H_{\mathrm{U}}^2)^{-\frac{\alpha}{2}}h_i)\right]\right]$$

$$= \mathbb{E}_{\phi_s}\left[\prod_{i\in\phi_s}\left(\frac{1}{1+s\overline{\mathrm{P}}\eta(r^2+H_{\mathrm{U}}^2)^{-\frac{\alpha}{2}}}\right)\right] \tag{B.1b}$$

$$= \exp\left(-2\pi\varphi_s\int_{\widehat{r}}^{R_U}\left(1-\left(\frac{1}{1+s\overline{\mathrm{P}}\eta(r^2+H_{\mathrm{U}}^2)^{-\frac{\alpha}{2}}}\right)\right)rdr\right). \tag{B.1c}$$

Here, (B.1a) is obtained by considering that the singleton devices in a given time slot follow a thinned PPP distribution ϕ_s with intensity $\varphi_s = \varphi P_{\mathrm{cf}}$, where φ is the intensity of the original PPP distribution and P_{cf} is given in (3.9). Moreover, (B.1b) is obtained by applying the moment generating function (MGF) of h which follows an exponential distribution with a unit mean. Furthermore, (B.1c) is obtained under the assumption that the collective interference experienced by the kth strongest device, which is located at a horizontal distance $\widehat{r}$ from the UAV, is generated by the singleton devices located within the annulus with inner and outer

radius of $\widehat{r}$ and R_U. Therefore, (3.14) is obtained by applying Campbell's theorem to (B.1b) and setting the lower and upper limits of integration of (B.1b) to $\widehat{r}$ and R, respectively.

B.2 Proof of Theorem 3.2

The Lagrangian function for (3.21) is given by

$$\mathfrak{L}(n_{\mathrm{s}}, \Delta_i) = -P_{\mathrm{sc}} + \Delta_1(n_{\mathrm{s}} - N_{\mathrm{A}}\lambda + \delta(\lambda)) + \Delta_2(\lambda - n_{\mathrm{s}}) + \Delta_3\Big(\mathbb{Q}\Big[\sqrt{\frac{Bt_{\mathrm{f}}}{Vn_{\mathrm{s}}}}\Big(\log_2(1+\gamma) - \frac{Dn_{\mathrm{s}}}{Bt_{\mathrm{f}}}\Big)\Big] - \epsilon\Big) + \Delta_4(\lambda_{\min} - \lambda) + \Delta_5(\lambda - \lambda_{\max}) + \Delta_6(r_{\min} - R_U),$$

where $\Delta_i, \forall i = 1, \cdots, 6$, corresponds to the Lagrangian multiplier associated with the C_ith constraint in (3.21). The KKT conditions for (3.21) are written as

$$n_{\mathrm{s}} - (N_{\mathrm{A}}\lambda + \delta(\lambda)) \leq 0, \tag{B.3a}$$

$$\lambda - n_{\mathrm{s}} \leq 0, \tag{B.3b}$$

$$\mathbb{Q}\left[\sqrt{\frac{Bt_{\mathrm{f}}}{Vn_{\mathrm{s}}}}\left(\log_2(1+\gamma) - \frac{Dn_{\mathrm{s}}}{Bt_{\mathrm{f}}}\right)\right] - \epsilon \leq 0, \tag{B.3c}$$

$$\lambda_{\min} - \lambda \leq 0, \lambda - \lambda_{\max} \leq 0, R_{\min} - R_U \leq 0, \tag{B.3d}$$

$$\Delta_1 \geq 0, \Delta_2 \geq 0, \Delta_3 \geq 0, \Delta_4 \geq 0, \Delta_5 \geq 0, \Delta_6 \geq 0, \tag{B.3e}$$

$$\Delta_1(n_{\mathrm{s}} - N_{\mathrm{A}}\lambda + \delta(\lambda)) = 0, \tag{B.3f}$$

$$\Delta_2(\lambda - n_{\mathrm{s}}) = 0, \tag{B.3g}$$

$$\Delta_3\left(\mathbb{Q}\left[\sqrt{\frac{Bt_{\mathrm{f}}}{Vn_{\mathrm{s}}}}\left(\log_2(1+\gamma) - \frac{Dn_{\mathrm{s}}}{Bt_{\mathrm{f}}}\right)\right] - \epsilon\right) = 0, \tag{B.3h}$$

$$\Delta_4(\lambda_{\min} - \lambda) = 0, \Delta_5(\lambda - \lambda_{\max}) = 0, \Delta_6(r_{\min} - R_U) = 0, \tag{B.3i}$$

$$\frac{\partial}{d\partial}(\mathfrak{L}(n_{\mathrm{s}}, \Delta_i)) = 0, \tag{B.3j}$$

where (B.3a), (B.3b), (B.3c), and (B.3d) correspond to the primal feasibility conditions associated with constraints $C_1 - C_6$ in (3.21), (B.3e) corresponds to the dual feasibility conditions associated with the Lagrangian multipliers in (B.2), (B.3f), (B.3g), (B.3h), and (B.3i) are the complementary slackness conditions applied to

the constraints in (3.21) and (B.3j) is the stationary condition. The first derivative of the Lagrangian associated with aforementioned stationary condition is given by

$$\frac{\partial}{\partial n_{\mathrm{s}}}(\mathfrak{L}(n_{\mathrm{s}},\Delta_i)) = -\frac{\partial}{\partial n_{\mathrm{s}}}(P_{\mathrm{sc}})+\Delta_1-\Delta_2+\Delta_3\left(-\frac{D\log(2)}{2\sqrt{Bt_{\mathrm{f}}}}n_{\mathrm{s}}^{-\frac{1}{2}}+\frac{\log(1+\gamma)\sqrt{Bt_{\mathrm{f}}}}{2}n_{\mathrm{s}}^{-\frac{3}{2}}\right), \tag{B.4}$$

where $\frac{\partial}{\partial n_{\mathrm{s}}}P_{\mathrm{sc}}$ is given by

$$\begin{aligned}\frac{\partial}{\partial n_{\mathrm{s}}}P_{\mathrm{sc}} =& \frac{1}{N_{\mathrm{A}}\lambda}\left(\sum_{j=1}^{L_s}\left(\prod_{k=1}^{j}\frac{3^{L_s-k}}{4^{L_s-1}}\frac{L_s!}{(L_s-k)!(k-1)!}\frac{1}{\mathrm{G}[1+j]}\mathrm{i}^{j(3+j)}3^{-\frac{1}{2}j(1+j-2L_s)}4^{(1-L_s)j}\right.\right.\\
&\times\Lambda\left(1-\frac{1}{4}jn_{\mathrm{s}}\pi R_U^2\tau\left(4\left(\frac{\theta_{\mathrm{T}}}{1+\theta_{\mathrm{T}}}\right)(1-y-xz)+3\left(\frac{\kappa\theta_{\mathrm{T}}}{1+\kappa\theta_{\mathrm{T}}}\right)\right)\right)\\
&+\Lambda n_{\mathrm{s}}\mathrm{G}[1-L_s]^{-1+j}\mathrm{G}[1+j-L_s](\mathrm{G}[2-L_s]\Gamma(L_s))^{-j}\left(j\left(1+\frac{1}{L_s}-2\coth^{-1}(7)\right)\right)\\
&\left.\left.+(-j+L_s)(\mathrm{H}_{j-L_s}-\mathrm{H}_{-L_s})N_{\mathrm{A}}\tau(y-zx)\right)\right),\end{aligned} \tag{B.5}$$

with $x=P_\lambda$, $y=P_{\mathrm{cf}}$, $\kappa=\left(\frac{H_{\mathrm{U}}^2+\frac{R_U^2}{4}}{H_{\mathrm{U}}^2+\frac{9R_U^2}{16}}\right)^{\frac{\alpha}{2}}$, and $\mathrm{G}[\cdot]$, $\mathrm{H}_{[\cdot]}$, and $\gimel$ denoting the Barnes-G function, Harmonic function, and the Euler's constant, respectively. Λ and τ are given by

$$\Lambda=\exp\left(\frac{1}{4}j\left(-\frac{4\left(H_{\mathrm{U}}^2+\frac{R_U^2}{4}\right)^{\frac{\alpha}{2}}\theta_{\mathrm{T}}\sigma^2}{\overline{\mathrm{P}}\eta}-4L_Ax(1-y)\left(\frac{\theta_{\mathrm{T}}}{1+\theta_{\mathrm{T}}}\right)\varphi_c-3N_{\mathrm{A}}xy\left(\frac{\kappa\theta_{\mathrm{T}}}{1+\kappa\theta_{\mathrm{T}}}\right)\right)\right) \tag{B.6}$$

and

$$\tau=-\frac{1}{n_{\mathrm{s}}^2}\exp(-\lambda)\sum_{L=1}^{n_{\mathrm{s}}-1}\frac{L\lambda^L}{L!}+\exp(-\lambda)\sum_{L=n_{\mathrm{s}}}^{\lambda+L_{lim}}\frac{\lambda^L}{\Gamma(1+L)}\left(\gimel-\mathrm{H}_L+\log(\lambda)\right), \tag{B.7}$$

respectively. From the complementary slackness condition, we know that either Δ_i is zero or the associated constraint function is zero for any given i. We consider one of the possible cases Δ_1 is not slack, i.e., Δ_1 exists and Δ_2, Δ_3 do not exist. Note that we ignore $\Delta_4, \Delta_5, \Delta_6$ as the corresponding constraints are not functions

of n_{s}. Thus, substituting $\Delta_1 \neq 0$, and Δ_2 ,$\Delta_3 = 0$ to the stationary condition, we obtain

$$-\frac{\partial}{\partial n_{\mathrm{s}}} P_{\mathrm{sc}} + \Delta_1 = 0. \tag{B.8}$$

Considering the complimentary slackness condition (B.3f), we obtain $\widetilde{n}_s = N_{\mathrm{A}}\lambda + \delta(\lambda)$. Substituting $\widetilde{n}_s$ to (B.8), we derive Δ_1 as

$$\Delta_1 = \frac{\partial}{\partial n_{\mathrm{s}}} P_{\mathrm{sc}}|_{n_{\mathrm{s}}=\widetilde{n}_s}. \tag{B.9}$$

It can be shown that the dual feasibility condition associated with Δ_1 is satisfied as $\Delta_1 \geq 0$. Also, $\widetilde{n}_s$ satisfy the primal feasibility conditions. Therefore, $\widetilde{n}_s$ and Δ_1 satisfy all the KKT conditions and it can be shown that $\widetilde{n}_s$ is the optimal solution to the **OP** in (3.21) when all the constraints in **OP** are slack, except for the first constraint.

Thus, the optimal solution to the **OP** is given as $n_{\mathrm{s}}^* = \min\left(N_{\mathrm{A}}\lambda + \delta(\lambda), n_\epsilon\right)$ where n_ϵ is the solution to $\mathbb{Q}\left[\sqrt{\frac{Bt_{\mathrm{f}}}{n_\epsilon}}\left(\log\left(1+\gamma\right) - \frac{D}{Bt_{\mathrm{f}}}\log(2)n_\epsilon\right)\right] - \epsilon = 0$. Therefore, $\widetilde{n_{\mathrm{s}}} = \lfloor n_{\mathrm{s}}^* \rfloor$. Note that this is the only solution to the **OP** in (3.21) as all the other possible cases of Δ_i violate one or more KKT conditions.

Appendix C

This appendix contains the proofs needed in Chapter 4.

C.1 Proofs of Section 4.2.1

C.1.1 Proof of Lemma 4.2.2

We obtain $f_{t_0,j}(t|x_0)$, where $j = 1, 2$, from the PDF of the first-order statistics of the sequence of i.i.d. random variables $\{W_i\}_{i=1}^{N_\mathrm{M}}$ with the sampling PDF $f_{W_i}(w, x_0)$. $f_{W_i}(w, x_0)$ can be obtained by taking the first derivative of $F_{W_i}(w, x_0)$ in (4.7) with respect to W_i.

C.1.2 Proof of Lemma 4.2.3

For U_0 located at x_0 with the contact distance t_0, the interference only comes from MUs located within the intersecting areas $\mathcal{C}_\mathrm{M} \bigcap \mathbb{B}(t_0, x_0)$. The CDF $F_V(v|t_0, x_0)$ is given as $\frac{|\mathcal{C}_\mathrm{M} \bigcap \mathbb{B}(v,x_0)|}{|\mathcal{C}_\mathrm{M} \bigcap \mathbb{B}(t_0,x_0)|}$. By taking the first derivative of this CDF, we obtain (4.11). The relevant cases in (4.11) are illustrated in Fig. C.1(b) and C.1(c), respectively.

C.1.3 Proof of Lemma 4.2.4

The aggregate interference at U_0 is given by $I_\mathrm{M} = \sum_{j=1}^{N_\mathrm{U}-1} P_{\mathrm{T,M}} \eta_\mathrm{m} \left(v_j^2 + H_U^2\right)^{-\frac{\alpha_\mathrm{m}}{2}} h_j$, where $N_\mathrm{M} \gg N_\mathrm{U}$, and v_j and h_j correspond to the distance between the interfering MU and U_0 and small-scale path loss power gain with Nakagami-m parameter m_M. The Laplace transform of I_M, conditioned on the contact distance t_0 and location

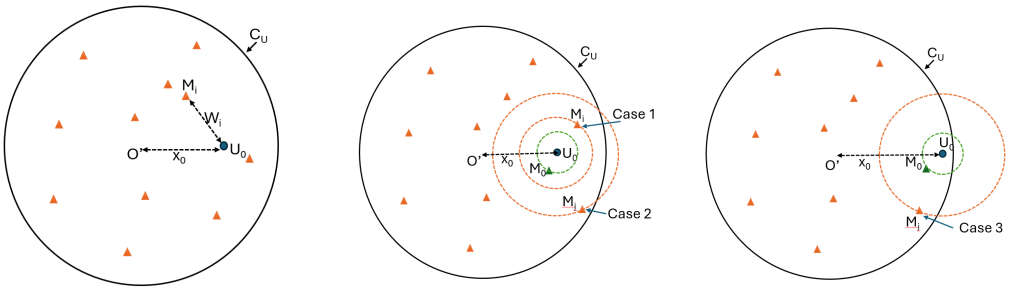

(a) Depiction of U_0 and M_i in Lemma 4.2.1.

(b) Intersecting areas corresponding to cases 1 and 2 in Lemma 4.2.3.

(c) Intersecting area corresponding to case 3 in Lemma 4.2.3.

Figure C.1: Depiction of parameters of Lemmas 4.2.1 and 4.2.3.

x_0 of U_0, as a function of s is derived as

$$\mathcal{L}_{I_{\mathrm{M}}}(s|t_0,x_0) = \mathbb{E}_{I_{\mathrm{M}}}\left[\exp\left(-sI_{\mathrm{M}}\right)\right] = \mathbb{E}_{I_{\mathrm{M}}}\left[\exp\left(-s\sum_{j=1}^{N_{\mathrm{U}}-1} P_{\mathrm{T,M}}\eta_{\mathrm{m}}\left(v_j^2+H_U^2\right)^{-\frac{\alpha_{\mathrm{m}}}{2}} h_i\right)\right]$$

$$= \mathbb{E}_{h,V}\left[\prod_{j=1}^{N_{\mathrm{U}}-1}\exp\left(-s\eta_{\mathrm{m}}\left(v_j^2+H_U^2\right)^{-\frac{\alpha_{\mathrm{m}}}{2}} h_j\right)\right]$$

$$= \mathbb{E}_V\left[\prod_{j=1}^{N_{\mathrm{U}}}\mathbb{E}_h\left[\exp\left(-sP_{\mathrm{T,M}}\eta_{\mathrm{m}}\left(v_j^2+H_U^2\right)\right)\right]\right]$$

$$= \left(\mathbb{E}_V\left[\left(\frac{m_{\mathrm{M}}}{m_{\mathrm{M}}+s\eta_{\mathrm{m}}\left(v_j^2+H_U^2\right)^{-\frac{\alpha_{\mathrm{m}}}{2}}}\right)^{m_{\mathrm{M}}}\right]\right)^{N_{\mathrm{U}}-1} \tag{C.1a}$$

$$= \left[\int \vartheta_M(v,s) f_V(v|t_0,x_0)\mathrm{d}v\right]^{N_{\mathrm{U}}-1}, \tag{C.1b}$$

where $\vartheta_M(v,s) = \left(\frac{m_{\mathrm{M}}}{m_{\mathrm{M}}+s\eta_{\mathrm{m}}P_{\mathrm{T,M}}\left(v^2+H_U^2\right)^{-\frac{\alpha_{\mathrm{m}}}{2}}}\right)^{m_{\mathrm{M}}}$, (C.1a) is the moment generating function of the Gamma function for Nakagami-m fading with fading parameter m_{M}, and $f_V(v|t_0,x_0)$ in C.1b is given in Lemma 4.2.3.

C.1.4 Proof of Proposition 4.1

The SINR of M_0 at U_0 located at x_0, is given as $\mathrm{SINR}(x_0) = \frac{P_{\mathrm{T,M}}\eta_{\mathrm{m}}\left(t_0^2+H_U^2\right)^{-\frac{\alpha_{\mathrm{m}}}{2}}h_0}{I_{\mathrm{M}}+\sigma_M^2}$.

$$P_{\mathrm{SINR}}^{\mathrm{MU}}(x_0) = \mathbb{E}_{t_0}\left[\Pr\left(\mathrm{SINR} \geq \Theta_{\mathrm{M}}|t_0\right)\right] = \mathbb{E}_{t_0}\left[\Pr\left(\frac{P_{\mathrm{T,M}}\eta_{\mathrm{m}}\left(t_0^2+H_U^2\right)^{-\frac{\alpha_{\mathrm{m}}}{2}}h_0}{I_{\mathrm{M}}+\sigma_M^2} \geq \Theta_{\mathrm{M}}|t_0\right)\right]$$

$$= \mathbb{E}_{t_0}\left[\mathbb{E}_{I_{\mathrm{M}}}\left[\Pr\left(h_0 \geq \frac{\Theta_{\mathrm{M}}(I_{\mathrm{M}}+\sigma_M^2)}{P_{\mathrm{T,M}}\eta_{\mathrm{m}}\left(t_0^2+H_U^2\right)^{-\frac{\alpha_{\mathrm{m}}}{2}}}|t_0\right)\right]\right]$$

$$\geq \mathbb{E}_{t_0}\left[1-\mathbb{E}_{I_{\mathrm{M}}}\left[\left(1-\exp\left(-\frac{\Theta_{\mathrm{M}}(I_{\mathrm{M}}+\sigma_M^2)}{P_{\mathrm{T,M}}\eta_{\mathrm{m}}\left(t_0^2+H_U^2\right)^{-\frac{\alpha_{\mathrm{m}}}{2}}}\varepsilon_M\right)\right)^{m_{\mathrm{M}}}|t_0\right]\right] \tag{C.2a}$$

$$= \int_0^{R_{\mathrm{C}}+x_0}\left(1-\mathbb{E}_{I_{\mathrm{M}}}\left[\left(1-\exp\left(\frac{\Theta_{\mathrm{M}}(I_{\mathrm{M}}+\sigma_M^2)}{P_{\mathrm{T,M}}\eta_{\mathrm{m}}\left(t^2+H_U^2\right)^{-\frac{\alpha_{\mathrm{m}}}{2}}\varepsilon_M}\right)\right)^{m_{\mathrm{M}}}\right]\right)f_{t_0}(t|x_0)\mathrm{d}t$$

$$= \int_0^{R_{\mathrm{C}}+x_0}\left(1-\mathbb{E}_{I_{\mathrm{M}}}\left[\sum_{k=0}^{m_{\mathrm{M}}}\binom{m_{\mathrm{M}}}{k}(-1)^k\left(\exp\left(-s(I_{\mathrm{M}}+\sigma_M^2)\right)\right)^k\right]\right)f_{t_0}(t|x_0)\mathrm{d}t \tag{C.2b}$$

$$= \int_0^{R_{\mathrm{C}}+x_0}\left(1-\mathbb{E}_{I_{\mathrm{M}}}\left[\sum_{k=0}^{m_{\mathrm{M}}}\binom{m_{\mathrm{M}}}{k}(-1)^k\exp\left(-sk(I_{\mathrm{M}}+\sigma_M^2)\right)\right]\right)f_{t_0}(t|x_0)\mathrm{d}t$$

$$= \int_0^{R_{\mathrm{C}}+x_0}\sum_{k=1}^{m_{\mathrm{M}}}\binom{m_{\mathrm{M}}}{k}(-1)^k\exp\left(-sk\sigma_M^2\right)\mathcal{L}_{I_{\mathrm{M}}}(sk|t,x_0)f_{t_0}(t|x_0)\mathrm{d}t,$$

where (C.2a) depends on a tight upper bound on the normalized Gamma variable m_{M}, which is $\mathbb{P}[m_{\mathrm{M}} < \chi] \geq \left(1-\exp\left(-m_{\mathrm{M}}(m_{\mathrm{M}}!)^{-\frac{1}{m_{\mathrm{M}}}}\chi\right)\right)^{m_{\mathrm{M}}}$, and $\varepsilon_M = m_{\mathrm{M}}(m_{\mathrm{M}}!)^{-\frac{1}{m_{\mathrm{M}}}}$ [156], and s in (C.2b) is given by $s = \frac{\Theta_{\mathrm{M}}\varepsilon_M}{P_{\mathrm{T,M}}\eta_{\mathrm{m}}(t^2+H_U^2)^{-\frac{\alpha_{\mathrm{m}}}{2}}}$.

C.2 Proofs of Section 4.2.2

C.2.1 Proof of Lemma 4.2.5

We consider that U_0 with an arbitrary ECZ angle φ_0 is always associated with its closest satellite S_0. The satellite associated with U_0 is named as the tagged satellite S_0. Note that in the UAV-to-satellite communication phase, we define the locations of transmitters and receivers in terms of their ECZ angles by taking the curvature of Earth into account. Thus, the location of a MU or UAV located on the MSL is

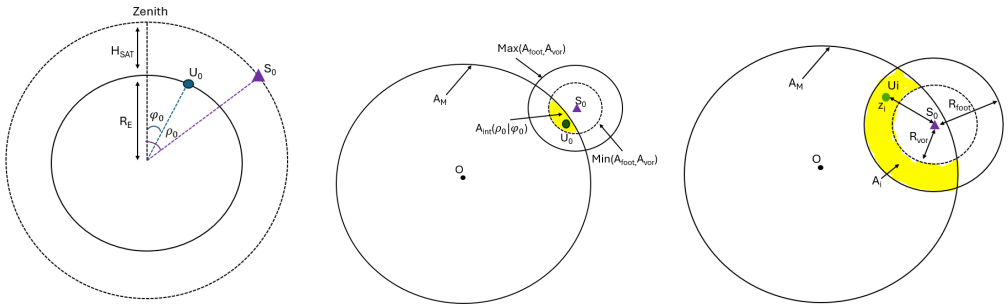

(a) φ_0 and ρ_0 in Lemma 4.2.5. (b) $|A_{\text{int}}(\rho_0|\varphi_0)|$ in Proposition 4.2. (c) $|A_{\text{I}}(\rho|\varphi_0)|$ in Lemmas 4.2.6 and 4.2.7.

Figure C.2: Parameters of Lemma 4.2.5 are depicted in Fig. C.2(a). Intersecting area in Proposition 4.2 is presented in Fig. C.2(b). Intersecting area in Lemmas 4.2.6 and 4.2.7 is depicted in Fig. C.2(c)

given as the ratio between horizontal distance from origin (i.e., O or $\acute{O}$) and radius of Earth[1]. The contact angle of U_0, which is defined as the ECZ angle between U_0 and its closest satellite S_0, is denoted by θ_0. The PDF of θ_0 conditioned on the location of U_0 is given in [103] as

$$f_{\theta_0}(\theta|\varphi_0) = \frac{N_{\text{S}}}{2}\sin(\theta)\exp\left(-\frac{N_{\text{S}}}{2}(1-\cos(\theta))\right), \tag{C.3}$$

where N_{S} is the number of satellites in the constellation.

We consider that the UAV's field of view is bounded by $\acute{\theta_0} \in \left(0, \frac{\pi}{2}\right)$. θ_0 between U_0 and S_0 can be reexpressed as a function of $\acute{\theta_0}$ [103] as

$$\theta_0 = \cot^{-1}\left(\frac{\cot\left(\acute{\theta_0} + \sqrt{\beta^2\left(1-\cot^2\acute{\theta_0}-\beta^2\right)}\right)}{1-\beta^2}\right), \tag{C.4}$$

where $\beta = \frac{R_{\text{E}}}{H_{\text{Sat}}+R_{\text{E}}}$. By substituting $\acute{\theta_0} = \frac{\pi}{2}$, we derive the upper bound on θ_0 as $\theta_{max} = \cot^{-1}\left(\frac{\beta}{\sqrt{1-\beta}}\right)$. Thus, U_0 can be potentially associated with any satellite located within the satellite dome region centred at U_0 with Earth-centred dome edge angle θ_{max}. Conditioned on φ_0, the ECZ of dome edge which corresponds to

[1]Note that the altitude of UAV from the MSL is ignored in the UAV-to-satellite communication phase, as $H_U \ll H_{\text{Sat}}$ from the perspective of satellite constellation.

the upperbound of ρ_0 is given as $\theta_{max} + \varphi_0$.

Conditioned on the location φ_0 of U_0, the PDF of ρ_0 of S_0 can be derived as

$$\begin{aligned} f_{\rho_0}(\rho|\varphi_0) &= \frac{\mathrm{d}\theta}{\mathrm{d}\rho} f_{\theta_0}(\theta|U_0) = \frac{\mathrm{d}(\rho-\varphi_0)}{\mathrm{d}\rho} f_{\theta_0}\left(\rho-\varphi_0\right) \\ &= \frac{\mathrm{d}(\rho-\varphi_0)}{\mathrm{d}\rho}\left(\frac{N_\mathrm{S}}{2}\sin\left(\rho-\varphi_0\right)\exp\left(-\frac{N_\mathrm{S}}{2}\left(1-\cos\left(\rho-\varphi_0\right)\right)\right)\right) \\ &= \frac{N_\mathrm{S}}{2}\sin\left(\rho-\varphi_0\right)\exp\left(-\frac{N_\mathrm{S}}{2}\left(1-\cos\left(\rho-\varphi_0\right)\right)\right), \end{aligned}$$

where $\rho_0 \in [\varphi_0, \varphi_0 + \theta_{max}]$.

C.2.2 Proof of Proposition 4.2

We consider that U_0 located at φ_0 is associated with its closest satellite S_0 if the following conditions are satisfied: (i) There is at least one satellite located within the spherical dome $\mathcal{A}_\mathrm{VIS}$ bounded centred at φ_0 bounded by θ_max and (ii) U_0 is located within the footprint area A_foot of S_0 which is located within $\mathcal{A}_\mathrm{VIS}$, and S_0 uniquely chooses U_0 as its associated UAV.

We define the probability associated with condition (i), denoted by P_vis, as the probability that the there is at least one satellite located within the spherical dome $\mathcal{A}_\mathrm{VIS}$ of U_0 which is centred at φ_0 and bounded by θ_max. The area of $\mathcal{A}_\mathrm{VIS}$ is given by $|\mathcal{A}_\mathrm{VIS}| = 2\pi(R_\mathrm{E} + H_\mathrm{Sat})H_\mathrm{Sat}$ [103]. Since the satellites are distributed according to a 3D PPP on the surface of a sphere $\mathcal{A}$ with radius $R_\mathrm{E} + H_\mathrm{Sat}$, the probability that there are k number of satellites in a spherical region $\mathcal{A}_\mathrm{VIS}$ is given by

$$\mathbb{P}(X=k) = \frac{1}{k!}\left(\lambda_S|\mathcal{A}_\mathrm{VIS}|\right)^k \exp\left(-\lambda_S|\mathcal{A}_\mathrm{VIS}|\right), \tag{C.5}$$

where $\lambda_S = \frac{N_\mathrm{S}}{4\pi(R_\mathrm{E}+H_\mathrm{Sat})^2}$ is the density of satellites in $\mathcal{A}_\mathrm{VIS}$.

Using (C.5), the probability that there is no satellite in $\mathcal{A}_\mathrm{VIS}$ is given as $\exp(-\lambda_S|\mathcal{A}_\mathrm{VIS}|)$. Thus, P_vis is given by

$$P_\mathrm{vis} = 1 - \exp(-\lambda_S 2\pi(R_\mathrm{E} + H_\mathrm{Sat})H_\mathrm{Sat}). \tag{C.6}$$

We define the probability associated with conditions (ii) as the probability that S_0 uniquely chooses U_0 as its associated UAV, given U_0 is located within the foot-

print of $\mathcal{S}_0$, denoted by P_{uniq}. We consider that U_0 can be potentially associated with S_0 in $\mathcal{A}_{\text{VIS}}$, if U_0 is located within the footprint of S_0, and U_0 is located within the Voronoi cell of S_0.

To derive P_{uniq}, we first compute the intersecting area of three regions: (i) maritime disk with radius R_{C}, denoted by A_{M}, (ii) footprint region of S_0, denoted by A_{foot}, and (iii) Voronoi cell of S_0, denoted by A_{vor}. The areas of A_{M} and A_{foot} are given by $|A_{\text{M}}| = \pi R_{\text{C}}^2$, and $|A_{\text{foot}}| = \pi(R_{\text{E}}\varphi_f)^2$, respectively.

To compute $|A_{\text{vor}}|$, we assume that the distribution of the number of UAVs in the typical Voronoi cell centred at the Earth zenith, is same as the distribution of the number of UAVs inside a disk $\mathbf{B}(\acute{O}, R_{\text{vor}})$ centred at the Earth zenith with radius R_{vor}, such that the area of the disk is equal to that of a typical Voronoi cell, i.e., $|A_{\text{vor}}| = \pi R_{\text{vor}}^2$. This assumption is well motivated and utilized in the literature for analytical tractability [162–164]. We approximate $|A_{\text{vor}}|$ using Expectation, where $\mathbb{E}[|A_{\text{vor}}|] = \frac{1}{\lambda_S} = \pi R_{\text{vor}}$. Thus, $R_{\text{vor}} = \sqrt{\frac{1}{\pi\lambda_S}}$. Conditioned on φ_0 the ρ_0-dependent area of intersection A_{int} of A_{M}, A_{foot}, and A_{vor}, and is given in (4.16).

The UAVs are distributed in A_{M} according to a BPP. Therefore, conditioned on φ_0, the ρ_0 dependent binomial probability of UAV distribution in $A_{\text{int}}(\rho_0|\varphi_0)$ is $P_{\text{I}}(\rho_0|\varphi_0) = \frac{|A_{\text{int}}(\rho_0|\varphi_0)|}{|A_{\text{M}}|}$, where $|A_{\text{M}}| = \pi R_{\text{E}}^2\left(1 - \cos\left(\frac{R_{\text{C}}}{R_{\text{E}}}\right)\right)$. Conditioned on φ_0 and ρ_0, the probability mass function (PMF) that there are k UAVs located within $A_{\text{int}}(\rho_0|\varphi_0)$ is

$$\mathbb{P}(N_{\text{U}} = k|\rho_0, \varphi_0) = \binom{N_{\text{U}}}{k} P_{\text{I}}(\rho_0|\varphi_0)^k \left(1 - P_{\text{I}}(\rho_0|\varphi_0)^{N_{\text{U}}-k}\right). \tag{C.7}$$

By using (4.14) and taking the expectation with respect to the number of UAVs within $A_{\text{int}}(\rho_0|\varphi_0)$, the U_0 location dependent $P_{\text{uniq}}(\varphi_0)$ is derived as

$$\begin{aligned} P_{\text{uniq}}(\varphi_0) &= \mathbb{E}_{\rho_0}\left[\sum_{k=1}^{N_{\text{U}}} \frac{1}{k}\binom{N_{\text{U}}}{k}(P_{\text{I}})^k(1-P_{\text{I}})^{N_{\text{U}}-k}\right] \\ &= \int_{\rho_{\max}}^{\rho_{\min}} \sum_{k=1}^{N_{\text{U}}} \frac{1}{k}\binom{N_{\text{U}}}{k}\left(\frac{A_{\text{int}}(\rho|\varphi_0)}{A_{\text{M}}}\right)^k \left(1 - \frac{A_{\text{int}}(\rho|\varphi_0)}{A_{\text{M}}}\right)^{N_{\text{U}}-k} f_{\rho_0}(\rho|\varphi_0)\mathrm{d}\rho, \end{aligned} \tag{C.8}$$

where $\rho_{\max} = \varphi_0 + \theta_{\max}$, $\rho_{\min} = \varphi_0$, and $f_{\rho_0}(\rho|\varphi_0)$ is given in Lemma 4.2.5. By

multiplying P_{vis} and P_{uniq} in (C.6) and (C.8), we obtain (4.15).

C.2.3 Proof of Lemma 4.2.6

We note that the interference at S_0 is produced by the other transmitting UAVs that are located within region A_{I}, which is the intersecting area of A_{M}, and annulus bounded by R_{foot} and R_{vor}, centred the at ECZ angle ρ_0, as depicted in Figure C.2(c). To calculate the number of interfering UAVs at S_0, we first calculate $A_{\text{I}}(\rho_0, \varphi_0)$ as follows.

$$\begin{aligned}
|A_{\text{I}}(\rho_0,\varphi_0)| &= |\mathbb{B}(O,R_{\text{C}}) \cap \mathbb{B}(y_0,R_{\text{foot}}) \cap \mathbb{B}^{'}(y_0,R_{\text{vor}})| \\
&= |\mathbb{B}(O,R_{\text{C}}) \cap \mathbb{B}(y_0,R_{\text{foot}})| - |\mathbb{B}(O,R_{\text{C}}) \cap \mathbb{B}(y_0,R_{\text{vor}})| \\
&= |A_{\text{M}} \cap A_{\text{foot}}| - |A_{\text{M}} \cap A_{\text{vor}}| \\
&= R_{\text{C}}^2 \arccos\left(\frac{c_1}{R_{\text{C}}}\right) - c_1\sqrt{(R_{\text{C}}^2 - c_1^2)} + R_{\text{foot}}^2 \left(\frac{c_2}{R_{\text{foot}}}\right) - c_2\sqrt{(R_{\text{foot}}^2 - c_2^2)} \\
&- \left(R_{\text{C}}^2 \arccos\left(\frac{c_3}{R_{\text{C}}}\right) - c_3\sqrt{(R_{\text{C}}^2 - c_3^2)} + R_{\text{vor}}^2 \left(\frac{c_4}{R_{\text{vor}}}\right) - c_4\sqrt{(R_{\text{vor}}^2 - c_4^2)}\right).
\end{aligned} \tag{C.9}$$

where c_1, c_2, c_3, and c_4 are defined in Lemma 4.2.6. Thus, the area of interfering UAVs of S_0 is given by

$$|A_{\text{I}}(\varphi_0)| = \int_{\rho_{\min}}^{\rho_{\max}} |A_{\text{I}}(R_{\text{E}}\rho,\varphi_0)| \frac{N_{\text{S}}}{2} \sin(\rho-\varphi_0) \exp\left(-\frac{N_{\text{U}}}{2}(1-\cos(\rho-\varphi_0))\right) \mathrm{d}\rho. \tag{C.10}$$

To compute the number of interfering UAVs within A_{I}, we assume that the interfering UAVs are uniformly distributed within A_{I}. Thus, the number of interfering UAVs at S_0 is equivalent to $\lambda_{U,Act}|A_{\text{I}}|$, where $\lambda_{U,Act}$ is the average intensity of active UAVs within A_{M}. To calculate $\lambda_{U,Act}$, we approximate the number of active UAVs within A_{M} by sorting the UAVs based on their ECZ angles in an ascending order, and calculate the average probability P_{act}^k that the kth closest UAV to $\acute{O}$ has a tagged satellite. Accordingly, P_{act^k} is given by

$$P_{\text{act}^k} = \mathbb{E}_{x_0}\left[P_{\text{Tag}}(x)\right] = \int_0^{R_{\text{C}}} P_{\text{Tag}}(x) f_{x_0}^k(x) \mathrm{d}x \tag{C.11}$$

$$= \int_0^{R_\mathrm{C}} P_\mathrm{Tag}(x) \frac{N_\mathrm{U}!}{(k-1)!(N_\mathrm{U}-k)!} \frac{2x}{R_\mathrm{C}^2} \left(\frac{x^2}{R_\mathrm{C}^2}\right)^{k-1} \left(\frac{x^2}{R_\mathrm{C}^2}\right)^{N_\mathrm{U}-k} \mathrm{d}x,$$

where $x_0 = R_\mathrm{E}\varphi_0$, $f_{x_0}(x)$ is the PDF of distance distribution of kth closest UAV to the origin and $f_{x_0}^k(x) = \frac{N_\mathrm{U}!}{(k-1)!(N_\mathrm{U}-k)!} \frac{2x}{R_\mathrm{C}^2} \left(\frac{x^2}{R_\mathrm{C}^2}\right)^{k-1} \left(\frac{x^2}{R_\mathrm{C}^2}\right)^{N_\mathrm{U}-k}$. The average number of UAVs with a tagged satellite within A_M is given by $\sum_{k=1}^{N_\mathrm{U}} P_\mathrm{act}^k$, and the average density of active UAVs within A_M is given by $\lambda_{U,Act} = \frac{\sum_{k=1}^{N_\mathrm{U}} P_\mathrm{act}^k}{\pi R_\mathrm{C}^2}$. Then, the number of interfering UAVs $N_\mathrm{U,int}$ at S_0 within A_I, conditioned on φ_0 is given by

$$N_\mathrm{U,int}(\varphi_0) = |A_\mathrm{I}(\varphi_0)| \lambda_{U,Act}. \tag{C.12}$$

By substituting P_act^k in (C.11) and $|A_\mathrm{I}(\varphi_0)|$ in (C.10) to (C.12), we obtain (4.18).

C.2.4 Proof of Lemma 4.2.7

We assume that the interfering UAVs are distributed according to a BPP within A_I, centred at S_0 location. Thus, the conditional CDF of distance z_0 between S_0 and an interfering UAV located within A_I is derived as

$$\begin{aligned} F_{z_0}(z) &= \frac{|A_\mathrm{M} \cap \mathbb{B}(\rho_0, z) \cap \mathbb{B}^{'}(\rho_0, z)|}{A_\mathrm{M} \cap A_\mathrm{foot} \cap A'_\mathrm{vor}} \\ &= \left(R_\mathrm{C}^2 \arccos\left(\frac{b_1}{R_\mathrm{C}^2}\right) - b_1 \sqrt{\left(R_\mathrm{C}^2 - b_1^2\right)} + z^2 \arccos\left(\frac{b_2}{z}\right) - b_2 \sqrt{\left(z^2 - b_2^2\right)} \right. \\ &\quad \left. - \left(R_\mathrm{C}^2 \arccos\left(\frac{b_3}{R_\mathrm{C}^2}\right) - b_3 \sqrt{\left(R_\mathrm{C}^2 - b_3^2\right)} + R_\mathrm{vor}^2 \arccos\left(\frac{b_4}{R_\mathrm{vor}}\right) - b_4 \sqrt{\left(R_\mathrm{vor}^2 - b_4^2\right)} \right) \right) \frac{1}{A_\mathrm{I}(\rho_0|\varphi_0)}, \end{aligned} \tag{C.13}$$

where $b_1 = \frac{R_\mathrm{C}^2 - z^2 + y_0^2}{2y_0}$, $b_2 = \frac{z^2 - R_\mathrm{C}^2 + y_0^2}{2y_0}$, $b_3 = \frac{R_\mathrm{C}^2 - R_\mathrm{vor}^2 + y_0^2}{2y_0}$, $b_4 = \frac{R_\mathrm{vor}^2 - R_\mathrm{C}^2 + y_0^2}{2y_0}$, and $|A_\mathrm{I}(\rho_0|\varphi_0)|$ is given in Lemma 4.2.6. Then, $f_{z_0}(z)$ is derived by taking the first derivative of $F_{z_0}(z)$ in (C.13) with respect to z.

C.2.5 Proof of Lemma 4.2.8

The aggregate interference at S_0 is given by $I_\mathrm{U} = \sum_{i=1}^{N_\mathrm{U,int}} P_\mathrm{T,U} \eta_\mathrm{S} d_i^{-\alpha_\mathrm{S}} h_i$, where $d_i = \sqrt{z_i^2 + H_\mathrm{Sat}^2}$, is the Euclidean distance between ith interfering UAV and S_0, and h_i is the small-scale fading gain. The Laplace transform of I_U as a function of

s, conditioned on location ρ_0 of S_0 is derived as

$$\begin{aligned}\mathcal{L}_{I_{\mathrm{U}}}(s|\rho_0,\varphi_0) = \mathbb{E}\left[\exp(-sI_{\mathrm{U}})\right] = \mathbb{E}\left[\exp\left(-s\sum_{i=1}^{N_{\mathrm{U,int}}} P_{\mathrm{T,U}}\eta_{\mathrm{S}} d_i^{-\alpha_{\mathrm{S}}} h_i\right)\right]\\ =\mathbb{E}\left[\prod_{i=1}^{N_{\mathrm{U,int}}} \exp\left(-sP_{\mathrm{T,U}}\eta_{\mathrm{S}} d_i^{-\alpha_{\mathrm{S}}} h_i\right)\right]\\ =\left(\mathbb{E}_{z_0}\left[\left(\frac{m_{\mathrm{S}}}{m_{\mathrm{S}} + sP_{\mathrm{T,U}}\eta_{\mathrm{S}}(z^2+H_{\mathrm{Sat}}^2)^{-\frac{\alpha_{\mathrm{S}}}{2}}}\right)^{m_{\mathrm{S}}}\right]\right)^{N_{\mathrm{U,int}}} \quad \text{(C.14a)}\\ =\left(\int_{R_{\mathrm{vor}}}^{R_{\mathrm{foot}}}\left(\frac{m_{\mathrm{S}}}{m_{\mathrm{S}} + sP_{\mathrm{T,U}}\eta_{\mathrm{S}}(z^2+H_{\mathrm{Sat}}^2)^{-\frac{\alpha_{\mathrm{S}}}{2}}}\right)^{m_{\mathrm{S}}} f_{z_0}(z)\mathrm{d}z\right)^{N_{\mathrm{U,int}}}. \quad \text{(C.14b)}\end{aligned}$$

where (C.14a) is the moment generating function of the Gamma function for Nakagami-m fading with fading parameter m_{S}, and (C.14b) is the Expectation of distance between S_0 and any interfering UAV where $f_{z_0}(z)$ is given in Lemma 4.2.7.

C.2.6 Proof of Proposition 4.3

The SINR of U_0 located at the ECZ angle φ_0 at its closest satellite S_0 is given as $\mathrm{SINR}(\varphi_0) = \frac{P_{\mathrm{T,U}}\eta_{\mathrm{S}} d_0^{-\alpha_{\mathrm{S}}} h_0}{I_{\mathrm{U}}+\sigma_S^2}$, where h_0 is the small-scale fading gain with Nakagami-m parameter m_{S} and d_0 is the contact distance between U_0 and S_0, given by $d_0(\rho_0) = \sqrt{((R_{\mathrm{E}}+H_{\mathrm{Sat}})^2 - 2R_{\mathrm{E}}(R_{\mathrm{E}}+H_{\mathrm{Sat}})\cos(\rho_0-\varphi_0))}$. I_{U} is the aggregate interference at S_0 and given by $\sum_{i=1}^{N_{\mathrm{U,int}}} P_{\mathrm{T,U}}\eta_{\mathrm{S}} d_i^{-\alpha_{\mathrm{S}}} h_i$. Based on these expressions, the SINR probability $P_{\mathrm{SINR}}(\varphi_0)$, of U_0 at S_0 is derived as

$$\begin{aligned}P_{\mathrm{SINR}}^{\mathrm{SAT}}(\varphi_0) = \Pr\left(\mathrm{SINR}(\varphi_0) \geq \Theta_{\mathrm{S}}\right) = \Pr\left(\frac{P_{\mathrm{T,U}}\eta_{\mathrm{S}} d_0(\rho_0)^{-\alpha_{\mathrm{S}}} h_0}{I_{\mathrm{U}}+\sigma_S^2} \geq \Theta_{\mathrm{S}}\right)\\ =\mathbb{E}_{\rho_0}\left[\mathbb{E}_{I_{\mathrm{U}}}\left[\Pr\left(h_0 \geq \frac{\Theta_{\mathrm{S}}\left(I_{\mathrm{U}}+\sigma_S^2\right)}{P_{\mathrm{T,U}}\eta_{\mathrm{S}} d_0(\rho_0)^{-\alpha_{\mathrm{S}}}}\right)\right]\right]\\ \geq\mathbb{E}_{\rho_0}\left[1-\mathbb{E}_{I_{\mathrm{U}}}\left[\left(1-\exp\left(\frac{\Theta_{\mathrm{S}}\left(I_{\mathrm{U}}+\sigma_S^2\right)}{P_{\mathrm{T,U}}\eta_{\mathrm{S}} d_0(\rho_0)^{-\alpha_{\mathrm{S}}}}\varepsilon_S\right)\right)^{m_{\mathrm{S}}}\right]\right] \quad \text{(C.15a)}\\ =\mathbb{E}_{\rho_0}\left[1-\mathbb{E}_{I_{\mathrm{U}}}\left[\sum_{j=0}^{m_{\mathrm{S}}}\binom{j}{m_{\mathrm{S}}}(-1)^j\exp\left(-s\left(I_{\mathrm{U}}+\sigma_S^2\right)\right)^j\right]\right] \quad \text{(C.15b)}\end{aligned}$$

$$
\begin{aligned}
&= \mathbb{E}_{\rho_0}\left[1 - \sum_{j=0}^{m_{\mathrm{S}}} \binom{j}{m_{\mathrm{S}}} (-1)^j \exp\left(-sj\sigma_S^2\right) \mathbb{E}_{I_{\mathrm{U}}}\left[\exp\left(-sjI_{\mathrm{U}}\right)\right]\right] \\
&= \mathbb{E}_{\rho_0}\left[1 - \sum_{j=0}^{m_{\mathrm{S}}} \binom{j}{m_{\mathrm{S}}} (-1)^j \exp\left(-sj\sigma_S^2\right) \mathcal{L}_{I_{\mathrm{U}}}\left(sj|\rho_0, \varphi_0\right)\right] \\
&= \int_{\rho_{\min}}^{\rho_{\max}} \sum_{j=1}^{m_{\mathrm{S}}} \binom{j}{m_{\mathrm{S}}} (-1)^{j+1} \exp\left(-sj\sigma_S^2\right) \mathcal{L}_{I_{\mathrm{U}}}\left(sj|\rho_0, \varphi_0\right) f_{\rho_0}(\rho) \mathrm{d}\rho \qquad \text{(C.15c)}
\end{aligned}
$$

where (C.15a) depends on thr tight upper bound on the normalized Gamma variable m_{S}, which is $\mathbb{P}[m_{\mathrm{S}} < \chi] \geq \left(1 - \exp(-m_{\mathrm{S}}(m_{\mathrm{S}}!)^{-\frac{1}{m_{\mathrm{S}}}}\chi)\right)^{m_{\mathrm{S}}}$. $\epsilon_{\mathrm{S}} = m_{\mathrm{S}}(m_{\mathrm{S}}!)^{-\frac{1}{m_{\mathrm{S}}}}$, and s in (C.15b) is given by $s = \frac{\Theta_{\mathrm{S}}\varepsilon_S}{P_{\mathrm{T,U}}\eta_{\mathrm{S}}} d_0(\rho_0)^{-\alpha_{\mathrm{S}}}$ $f_{\rho_0(\rho)}$ is given in Lemma 4.2.5.

Bibliography

[1] W. Jiang, B. Han, M. A. Habibi, and H. D. Schotten, "The road towards 6g: A comprehensive survey," *IEEE Open Journal of the Communications Society*, vol. 2, pp. 334–366, 2021.

[2] M. Alsabah, M. A. Naser, B. M. Mahmmod, S. H. Abdulhussain, M. R. Eissa, A. Al-Baidhani, N. K. Noordin, S. M. Sait, K. A. Al-Utaibi, and F. Hashim, "6g wireless communications networks: A comprehensive survey," *IEEE Access*, vol. 9, pp. 148 191–148 243, 2021.

[3] Y. Zeng, Q. Wu, and R. Zhang, "Accessing from the sky: A tutorial on UAV communications for 5G and beyond," *Proc. IEEE*, vol. 107, no. 12, pp. 2327–2375, 2019.

[4] G. Geraci, A. Garcia-Rodriguez, and X. Lin, "Preparing the ground for drone communications," Jun. 2019. [Online]. Available: https://www.comsoc.org/publications/ctn/preparing-ground-drone-communications

[5] A. S. Abdalla and V. Marojevic, "Communications standards for unmanned aircraft systems: The 3gpp perspective and research drivers," *IEEE Communications Standards Magazine*, vol. 5, no. 1, pp. 70–77, 2021.

[6] S. Mohsan, N. Othman, Y. Li, M. Alsharif, and M. Khan, "Unmanned aerial vehicles (UAVs): practical aspects, applications, open challenges, security issues, and future trends." in *Intel Serv Robotics*, 2023, pp. 109–137.

[7] 3GPP, "3GPP TR 22.829: enhancement for unmaned aerial vehicles (uavs) (Release 16)," 2019.

[8] ——, "3GPP TR 23.754: study on supporting unmanned aerial systems (UAS) connectivity, identification and tracking (Release 17)," 2020.

[9] ——, "3GPP: Rp-230783 WI on enhanced lte support for UAV (Release 18)," Mar. 2023.

[10] A. Fotouhi, H. Qiang, M. Ding, M. Hassan, L. G. Giordano, A. Garcia-Rodriguez, and J. Yuan, "Survey on uav cellular communications: Practical aspects, standardization advancements, regulation, and security challenges," *IEEE Commun. Surveys Tuts.*, vol. 21, no. 4, pp. 3417–3442, Fourthquarter 2019.

[11] H. Määttänen, *3GPP Standardization for Cellular-Supported UAVs*, 2021, pp. 163–180.

[12] M. Mozaffari, W. Saad, M. Bennis, Y. Nam, and M. Debbah, "A tutorial on UAVs for wireless networks: Applications, challenges, and open problems," *IEEE Commun. Surveys Tuts.*, vol. 21, no. 3, pp. 2334–2360, Mar. 2019.

[13] M. K. Banafaa, m. Pepeoğlu, I. Shayea, A. Alhammadi, Z. A. Shamsan, M. A. Razaz, M. Alsagabi, and S. Al-Sowayan, "A comprehensive survey on 5G-and-beyond networks with UAVs: Applications, emerging technologies, regulatory aspects, research trends and challenges," *IEEE Access*, vol. 12, pp. 7786–7826, 2024.

[14] X. Lin, V. Yajnanarayana, S. D. Muruganathan, S. Gao, H. Asplund, H. Maattanen, M. Bergstrom, S. Euler, and Y. . E. Wang, "The sky is not the limit: LTE for unmanned aerial vehicles," *IEEE Commun. Mag.*, vol. 56, no. 4, pp. 204–210, Apr. 2018.

[15] Y. Zeng, J. Lyu, and R. Zhang, "Cellular-connected UAV: potential, challenges, and promising technologies," *IEEE Wireless Commun.*, vol. 26, no. 1, pp. 120–127, Feb. 2019.

[16] The Department of Infrastructure, Transport, Regional Development, Communications and the Arts, Australian Government, "Drones in australia." [Online]. Available: https://www.drones.gov.au/about

[17] M. Wiedemann, A. Vij, R. Banerjee, A. O'Connor, D. Soetanto, A. Ardeshiri, A. V., G. Wittwer, and N. Sheard, "Validating the benefits of increased drone uptake for australia: Geographic, demographic and social insights," Mar. 2023.

[18] R. D. Department of Infrastructure and Communications, "Economic benefit analysis of drones in australia, final report," Oct. 2020.

[19] Y. Zeng, R. Zhang, and T. J. Lim, "Wireless communications with unmanned aerial vehicles: opportunities and challenges," *IEEE Communications Magazine*, vol. 54, no. 5, pp. 36–42, May 2016.

[20] R. Rolly., P. Malarvezhi, and T. Lagkas, "Unmanned aerial vehicles: Applications, techniques, and challenges as aerial base stations." *International Journal of Distributed Sensor Networks*, 2022.

[21] J. G. Andrews, A. K. Gupta, and H. S. Dhillon, "A Primer on Cellular Network Analysis Using Stochastic Geometry," *arXiv e-prints*, p. arXiv:1604.03183, Apr. 2016.

[22] Nokia, "F-Cell technology from nokia bell labs revolutionizes small cell deployment by cutting wires, costs and time," Oct. 2016. [Online]. Available: https://www.nokia.com/about-us/news/releases/2016/10/03/f-cell-technology-from-nokia-bell-labs-revolutionizes-small-cell-deployment-by-cutting-wires-costs-and-time/

[23] Huawei, "Digital sky initiative," Nov. 2017. [Online]. Available: https://www.huawei.com/en/industry-insights/outlook/mobile-broadband/xlabs/industry-views/digital-sky-initiative

[24] R. Amer, W. Saad, H. ElSawy, M. M. Butt, and N. Marchetti, "Caching to the sky: Performance analysis of cache-assisted CoMP for cellular-connected uavs," in *IEEE WCNC*, Apr. 2019.

[25] L. Dai, B. Wang, Z. Ding, Z. Wang, S. Chen, and L. Hanzo, "A survey of non-orthogonal multiple access for 5G," *IEEE Commun. Surveys Tuts.*, vol. 20, no. 3, pp. 2294–2323, May 2018.

[26] M. Liaqat, K. A. Noordin, T. A. Latef, and K. Dimyati, "Power-domain non orthogonal multiple access (PD-NOMA) in cooperative networks: an overview," *Wirel. Netw.*, pp. 1–23, Jul. 2018.

[27] X. Su, A. Castiglione, C. Esposito, and C. Choi, "Power domain NOMA to support group communication in public safety networks," *Futur. Gener. Comp. Sy.*, vol. 84, pp. 228–238, Jul. 2018.

[28] Y. Liu, Z. Qin, Y. Cai, Y. Gao, G. Y. Li, and A. Nallanathan, "UAV communications based on non-orthogonal multiple access," *IEEE Wirel. Commun.*, vol. 26, no. 1, pp. 52–57, Feb. 2019.

[29] N. Rupasinghe, Y. Yapıcı, I. Güvenç, and Y. Kakishima, "Non-orthogonal multiple access for mmwave drone networks with limited feedback," *IEEE Trans. Commun.*, vol. 67, no. 1, pp. 762–777, Jan. 2019.

[30] R. Duan, J. Wang, C. Jiang, H. Yao, Y. Ren, and Y. Qian, "Resource allocation for multi-UAV aided IoT NOMA uplink transmission systems," *IEEE Internet Things J.*, vol. 6, no. 4, pp. 7025–7037, Aug. 2019.

[31] N. Zhao, X. Pang, Z. Li, Y. Chen, F. Li, Z. Ding, and M. Alouini, "Joint trajectory and precoding optimization for UAV-Assisted NOMA networks," *IEEE Trans. Commun.*, vol. 67, no. 5, pp. 3723–3735, May 2019.

[32] J. Sun, Z. Wang, and Q. Huang, "Cyclical NOMA based UAV-enabled wireless network," *IEEE Access*, vol. 7, pp. 4248–4259, Dec. 2019.

[33] T. Hou, Y. Liu, Z. Song, X. Sun, and Y. Chen, "Exploiting noma for uav communications in large-scale cellular networks," *IEEE Trans. Commun.*, vol. 67, no. 10, pp. 6897–6911, Jul. 2019.

[34] L. Liu, S. Zhang, and R. Zhang, "Exploiting NOMA for multi-beam UAV communication in cellular uplink," in *Proc. IEEE ICC*, May 2019.

[35] W. Mei and R. Zhang, "Uplink cooperative NOMA for cellular-connected UAV," *IEEE J. Sel. Topics Signal Process.*, vol. 13, no. 3, pp. 644–656, Jun. 2019.

[36] A. Rahmati, Y. Yapici, N. Rupasinghe, I. Guvenc, H. Dai, and A. Bhuyan, "Energy efficiency of RSMA and NOMA in cellular-connected mmWave UAV networks," in *Proc. IEEE ICC Workshops*, May 2019.

[37] T. Hou, Y. Liu, Z. Song, X. Sun, and Y. Chen, "NOMA-enhanced terrestrial and aerial IoT networks with partial CSI," *IEEE Internet Things J.*, vol. 7, no. 4, pp. 3254–3266, Jan. 2020.

[38] J. Lyu, Y. Zeng, R. Zhang, and T. J. Lim, "Placement optimization of UAV-Mounted mobile base stations," *IEEE Commun. Lett.*, vol. 21, no. 3, pp. 604–607, Mar. 2017.

[39] M. Alzenad, A. El-Keyi, and H. Yanikomeroglu, "3-D placement of an unmanned aerial vehicle base station for maximum coverage of users with different QoS requirements," *IEEE Wireless Commun. Lett.*, vol. 7, no. 1, pp. 38–41, Feb. 2018.

[40] M. M. U. Chowdhury, E. Bulut, and I. Guvenc, "Trajectory optimization in UAV-assisted cellular networks under mission duration constraint," in *Proc. IEEE RWS*, Jan. 2019, pp. 1–4.

[41] Y. Huang, W. Mei, J. Xu, L. Qiu, and R. Zhang, "Cognitive uav communication via joint maneuver and power control," *IEEE Trans. Commun.*, Nov. 2019.

[42] D. Yang, Q. Wu, Y. Zeng, and R. Zhang, "Energy tradeoff in ground-to-UAV communication via trajectory design," *IEEE Trans. Veh. Technol.*, vol. 67, no. 7, pp. 6721–6726, Jul. 2018.

[43] C. Zhang and W. Zhang, "Spectrum sharing for drone networks," *IEEE J. Sel. Areas Commun.*, vol. 35, no. 1, pp. 136–144, Jan. 2017.

[44] V. V. Chetlur and H. S. Dhillon, "Downlink coverage analysis for a finite 3-D wireless network of unmanned aerial vehicles," *IEEE Trans. Commun.*, vol. 65, no. 10, pp. 4543–4558, Oct. 2017.

[45] A. Al-Hourani, S. Kandeepan, and S. Lardner, "Optimal LAP altitude for maximum coverage," *IEEE Wireless Commun. Lett.*, vol. 3, no. 6, pp. 569–572, Dec. 2014.

[46] Y. Zhang, P. Ren, L. Sun, Q. Du, and Y. Wang, "Antenna tilt assignment for three-dimensional beamforming in multiuser systems," in *Proc. IEEE GLOBECOM*, Dec. 2015, pp. 1–6.

[47] D. López-Pérez, M. Ding, H. Li, L. G. Giordano, G. Geraci, A. Garcia-Rodriguez, Z. Lin, and M. Hassan, "On the downlink performance of UAV communications in dense cellular networks," in *Proc. IEEE GLOBECOM*, Dec. 2018.

[48] S. Enayati, H. Saeedi, H. Pishro-Nik, and H. Yanikomeroglu, "Moving aerial base station networks: A stochastic geometry analysis and design perspective," *IEEE Trans. Wireless Commun.*, vol. 18, no. 6, pp. 2977–2988, Jun. 2019.

[49] 3GPP, "3GPP TR 36.777: Study on enhanced LTE support for aerial vehicles (Release 15)," 2017.

[50] M. Banagar and H. S. Dhillon, "3GPP-inspired stochastic geometry-based mobility model for a drone cellular network," in *Proc. IEEE GLOBECOM*, Dec. 2019.

[51] P. K. Sharma and D. I. Kim, "Coverage probability of 3-D mobile UAV networks," *IEEE Wireless Commun. Lett.*, vol. 8, no. 1, pp. 97–100, Feb. 2019.

[52] CRED, "2021 disasters in numbers," Centre for Research on the Epidemiology of Disasters, Tech. Rep., 2022.

[53] M. Lefebvre and J. Reinhard, "The cost of extreme weather," The McKell Institute, Tech. Rep., Sep. 2022.

[54] M. Yebra, et. al., "Towards an integrated hi-tech solution to detect small fires," *Australian Journal of Emergency Management*, vol. 37, no. 4, pp. 44–47, Oct. 2022.

[55] S. Awadallah, D. Moure, and P. Torres-González, "An Internet of Things (IoT) application on volcano monitoring," *Sensors*, vol. 19, no. 21, pp. 46–51, Oct. 2019.

[56] N. F. Raun, "Smart environment using internet of things(IoTs) - a review," in *Proc. IEEE IEMCON*, 2016, pp. 1–6.

[57] N. Nikaein, M. Laner, K. Zhou, P. Svoboda, D. Drajic, M. Popovic, and S. Krco, "Simple traffic modeling framework for machine type communication," in *Proc. ISWCS*, 2013, pp. 1–5.

[58] A. Bulashenko, S. Piltyay, A. Polishchuk, and O. Bulashenko, "New traffic model of M2M technology in 5G wireless sensor networks," in *Proc. IEEE ATIT*, 2020, pp. 125–131.

[59] O. M. Bushnaq, A. Celik, H. Elsawy, M. Alouini, and T. Y. Al-Naffouri, "Aeronautical data aggregation and field estimation in IoT networks: Hovering and traveling time dilemma of UAVs," *IEEE Trans. Wireless Commun.*, vol. 18, no. 10, pp. 4620–4635, Oct. 2019.

[60] H. Dai, H. Zhang, C. Li, and B. Wang, "Efficient deployment of multiple UAVs for IoT communication in dynamic environment," *China Commun.*, vol. 17, no. 1, pp. 89–103, Jan. 2020.

[61] M. Mozaffari, W. Saad, M. Bennis, and M. Debbah, "Mobile unmanned aerial vehicles (UAVs) for energy-efficient internet of things communications," *IEEE Trans. Wireless Commun.*, vol. 16, no. 11, pp. 7574–7589, Nov. 2017.

[62] Z. Sun, Z. Wei, N. Yang, and X. Zhou, "Two-tier communication for UAV-enabled massive IoT systems: Performance analysis and joint design of trajectory and resource allocation," *IEEE J. Sel. Areas Commun.*, vol. 39, no. 4, pp. 1132–1146, Apr. 2021.

[63] Q. Wu, J. Xu, Y. Zeng, D. W. K. Ng, N. Al-Dhahir, R. Schober, and A. L. Swindlehurst, "A comprehensive overview on 5G-and-beyond networks with UAVs : From communications to sensing and intelligence," *IEEE J. Sel. Areas Commun.*, vol. 39, no. 10, pp. 2912–2945, Oct. 2021.

[64] L. Yuan, N. Yang, F. Fang, and Z. Ding, "Performance analysis of UAV-assisted short-packet cooperative communications," *IEEE Trans. Veh. Technol.*, vol. 71, no. 4, pp. 4471–4476, Apr. 2022.

[65] M. B. Shahab, R. Abbas, M. Shirvanimoghaddam, and S. J. Johnson, "Grant-free non-orthogonal multiple access for IoT: A survey," *IEEE Commun. Surveys Tuts.*, vol. 22, no. 3, pp. 1805–1838, thirdquater 2020.

[66] Z. Wang, T. Lv, Z. Lin, J. Zeng, and P. T. Mathiopoulos, "Outage performance of URLLC NOMA systems with wireless power transfer," *IEEE Wirel. Commun. Lett.*, vol. 9, no. 3, pp. 380–384, Mar. 2020.

[67] B. Di, L. Song, Y. Li, and G. Y. Li, "NOMA-based low-latency and high-reliable broadcast communications for 5G V2X services," in *Proc. IEEE GLOBECOM*, 2017, pp. 1–6.

[68] C. Zhang, Y. Liu, and Z. Ding, "Semi-grant-free NOMA: A stochastic geometry model," *IEEE Trans. Wireless Commun.*, vol. 21, no. 2, pp. 1197–1213, Feb. 2022.

[69] Z. Yuan, G. Yu, W. Li, Y. Yuan, X. Wang, and J. Xu, "Multi-user shared access for Internet of Things," in *Proc. IEEE VTC Spring*, 2016, pp. 1–5.

[70] ZTE, "Physical layer abstraction method for MMSE-SIC type receiver, R1-1608954," 2016.

[71] E. M. Eid, M. M. Fouda, A. S. Tag Eldien, and M. M. Tantawy, "Performance analysis of MUSA with different spreading codes using ordered SIC methods," in *Proc. ICCES*, 2017, pp. 101–106.

[72] C. Sun, C. She, C. Yang, T. Q. S. Quek, Y. Li, and B. Vucetic, "Optimizing resource allocation in the short blocklength regime for ultra-reliable and low-latency communications," *IEEE Trans. Wireless Commun.*, vol. 18, no. 1, pp. 402–415, Jan. 2019.

[73] M. Serror, C. Dombrowski, K. Wehrle, and J. Gross, "Channel coding versus cooperative ARQ: Reducing outage probability in ultra-low latency wireless communications," in *Proc. IEEE GLOBECOM Wkshps*, 2015, pp. 1–6.

[74] K. Chen, Y. Wang, J. Zhao, X. Wang, and Z. Fei, "URLLC-oriented joint power control and resource allocation in UAV-assisted networks," *IEEE Internet Things J.*, vol. 8, no. 12, pp. 10 103–10 116, Jun. 2021.

[75] X. Sun, S. Yan, N. Yang, Z. Ding, C. Shen, and Z. Zhong, "Short-packet downlink transmission with non-orthogonal multiple access," *IEEE Trans. Wirel. Commun.*, vol. 17, no. 7, pp. 4550–4564, Jul. 2018.

[76] S. Han, X. Xu, Z. Liu, P. Xiao, K. Moessner, X. Tao, and P. Zhang, "Energy-efficient short packet communications for uplink NOMA-based massive MTC networks," *IEEE Trans. Veh Technol.*, vol. 68, no. 12, pp. 12 066–12 078, Dec. 2019.

[77] H. Hu, Y. Huang, G. Cheng, Q. Kang, H. Zhang, and Y. Pan, "Optimization of energy efficiency in UAV-enabled cognitive IoT with short packet communication," *IEEE Sensors J.*, vol. 22, no. 12, pp. 12 357–12 368, Jun. 2022.

[78] B. Yu, X. Guan, and Y. Cai, "Joint blocklength and power optimization for half duplex unmanned aerial vehicle relay system with short packet communications," in *Proc. WCSP*, 2020, pp. 981–986.

[79] J. Pei, Z. Li, P. Jiang, S. Li, and F. Renhai, "A joint blocklength and location optimization scheme for UAV-assisted smart port communication," in *Proc. IEEE ICICN*, 2021, pp. 124–129.

[80] C. Pan, H. Ren, Y. Deng, M. Elkashlan, and A. Nallanathan, "Joint blocklength and location optimization for URLLC-enabled UAV relay systems," *IEEE Commun. Lett.*, vol. 23, no. 3, pp. 498–501, Mar. 2019.

[81] K. Chen, Y. Wang, Z. Fei, and X. Wang, "Power limited ultra-reliable and low-latency communication in UAV-enabled IoT networks," in *Proc. IEEE WCNC*, 2020, pp. 1–6.

[82] K. Wang, C. Pan, H. Ren, W. Xu, L. Zhang, and A. Nallanathan, "Packet error probability and effective throughput for ultra-reliable and low-latency UAV communications," *IEEE Trans. Commun.*, vol. 69, no. 1, pp. 73–84, Jan. 2021.

[83] C. Zhang, Z. Qin, Y. Liu, and K. K. Chai, "Semi-grant-free uplink NOMA with contention control: A stochastic geometry model," in *Proc. IEEE ICC Workshops*, 2020, pp. 1–6.

[84] Q. Wang, X. Li, S. Bhatia, Y. Liu, L. T. Alex, S. A. Khowaja, and V. G. Menon, "UAV-enabled non-orthogonal multiple access networks for ground-air-ground communications," *IEEE Trans. Green Commun. Netw.*, vol. 6, no. 3, pp. 1340–1354, Sep. 2022.

[85] G. Sreya, S. Saigadha, P. D. Mankar, G. Das, and H. S. Dhillon, "Adaptive rate NOMA for cellular IoT networks," *IEEE Wirel. Commun. Lett.*, vol. 11, no. 3, pp. 478–482, Mar. 2022.

[86] J. Liu, G. Wu, X. Zhang, S. Fang, and S. Li, "Modeling, analysis, and optimization of grant-free NOMA in massive MTC via stochastic geometry," *IEEE Internet Things J.*, vol. 8, no. 6, pp. 4389–4402, Mar. 2021.

[87] R. Fu, Q. Qi, C. Zhong, X. Chen, and Z. Zhang, "Block error rate analysis of short-packet NOMA communications with imperfect SIC," in *Proc. IEEE ICCC*, 2020, pp. 68–73.

[88] R. Abbas, M. Shirvanimoghaddam, Y. Li, and B. Vucetic, "On the performance of massive grant-free NOMA," in *Proc. IEEE PIMRC*, 2017, pp. 1–6.

[89] T. Wei, W. Feng, Y. Chen, C.-X. Wang, N. Ge, and J. Lu, "Hybrid satellite-terrestrial communication networks for the maritime Internet of Things: key technologies, opportunities, and challenges," *IEEE Internet Things J.*, vol. 8, no. 11, Jun. 2021.

[90] W. Feng, Y. Wang, Y. Chen, N. Ge, and C.-X. Wang, "Structured satellite-UAV-terrestrial networks for 6G Internet of Things," *IEEE Netw.(Early Access)*, pp. 1–1, 2024.

[91] H. Zeng, Z. Su, Q. Xu, and R. Li, "Security and privacy in space-air-ocean integrated unmanned surface vehicle networks," *IEEE Netw. (Early Access)*, pp. 1–1, 2024.

[92] N. Nomikos, P. K. Gkonis, P. S. Bithas, and P. Trakadas, "A survey on UAV-aided maritime communications: Deployment considerations, applications, and future challenges," *IEEE OJ-COMS*, vol. 4, pp. 56–78, 2023.

[93] F. S. Alqurashi, A. Trichili, N. Saeed, B. S. Ooi, and M.-S. Alouini, "Maritime communications: A survey on enabling technologies, opportunities, and challenges," *IEEE Internet Things J.*, vol. 10, no. 4, pp. 3525–3547, Feb. 2023.

[94] S. S. Hassan, D. H. Kim, Y. K. Tun, N. H. Tran, W. Saad, and C. S. Hong, "Seamless and energy-efficient maritime coverage in coordinated 6G space–air–sea non-terrestrial networks," *IEEE Internet Things J.*, vol. 10, no. 6, pp. 4749–4769, Mar. 2023.

[95] Y. Wang, W. Feng, J. Wang, and T. Q. S. Quek, "Hybrid satellite-UAV-terrestrial networks for 6G ubiquitous coverage: A maritime communications perspective," *IEEE J. Sel. Areas Commun.*, vol. 39, no. 11, pp. 3475–3490, Nov. 2021.

[96] J. Xu, M. A. Kishk, and M.-S. Alouini, "Space-air-ground-sea integrated networks: Modeling and coverage analysis," *IEEE Trans. Wireless Commun.*, vol. 22, no. 9, pp. 6298–6313, Sep. 2023.

[97] X. Hu, B. Lin, P. Wang, X. Lu, H. Wei, and S. Qi, "Modeling and analysis of end-to-end LEO satellite-aided shore-to-ship communications," in *Proc. IEEE ICCC*, 2023, pp. 1–6.

[98] Q. Wang, H.-N. Dai, Q. Wang, M. K. Shukla, W. Zhang, and C. G. Soares, "On connectivity of UAV-assisted data acquisition for underwater Internet of Things," *IEEE Internet Things J.*, vol. 7, no. 6, pp. 5371–5385, Jun. 2020.

[99] A. Yastrebova, I. Angervuori, N. Okati, M. Vehkaperä, M. Höyhtyä, R. Wichman, and T. Riihonen, "Theoretical and simulation-based analysis of terrestrial interference to LEO satellite uplinks," in *Proc. IEEE GLOBECOM*, 2020, pp. 1–6.

[100] N. Okati, T. Riihonen, D. Korpi, I. Angervuori, and R. Wichman, "Downlink coverage and rate analysis of low earth orbit satellite constellations using

stochastic geometry," *IEEE Trans. Commun.*, vol. 68, no. 8, pp. 5120–5134, Aug. 2020.

[101] N. Okati and T. Riihonen, "Stochastic analysis of satellite broadband by mega-constellations with inclined LEOs," in *Proc. IEEE PMIRC*, 2020, pp. 1–6.

[102] ——, "Modeling and analysis of LEO mega-constellations as nonhomogeneous Poisson point processes," in *Proc. IEEE VTC-Spring*, 2021, pp. 1–5.

[103] A. Al-Hourani, "An analytic approach for modeling the coverage performance of dense satellite networks," *IEEE Wireless Commun. Lett.*, vol. 10, no. 4, pp. 897–901, Apr. 2021.

[104] B. A. Homssi and A. Al-Hourani, "Modeling uplink coverage performance in hybrid satellite-terrestrial networks," *IEEE Commun. Lett.*, vol. 25, no. 10, pp. 3239–3243, Oct. 2021.

[105] H. Lin, C. Zhang, Y. Huang, R. Zhao, and L. Yang, "Fine-grained analysis on downlink LEO satellite-terrestrial mmWave relay networks," *IEEE Wireless Commun. Lett.*, vol. 10, no. 9, pp. 1871–1875, Sep. 2021.

[106] A. Talgat, M. A. Kishk, and M.-S. Alouini, "Stochastic geometry-based analysis of LEO satellite communication systems," *IEEE Commun. Lett.*, vol. 25, no. 8, pp. 2458–2462, Aug. 2021.

[107] N. Okati and T. Riihonen, "Nonhomogeneous stochastic geometry analysis of massive LEO communication constellations," *IEEE Trans. Commun.*, vol. 70, no. 3, pp. 1848–1860, Mar. 2022.

[108] C. C. Chan, B. Al Homssi, and A. Al-Hourani, "A stochastic geometry approach for analyzing uplink performance for IoT-over-satellite," in *Proc. IEEE ICC*, 2022, pp. 2363–2368.

[109] B. Manzoor, A. Al-Hourani, and B. A. Homssi, "Improving IoT-over-satellite connectivity using frame repetition technique," *IEEE Wireless Commun. Lett.*, vol. 11, no. 4, pp. 736–740, 2022.

[110] B. Al Homssi and A. Al-Hourani, "Optimal beamwidth and altitude for maximal uplink coverage in satellite networks," *IEEE Wireless Commun. Lett.*, vol. 11, no. 4, pp. 771–775, Apr. 2022.

[111] D.-H. Jung, J.-G. Ryu, W.-J. Byun, and J. Choi, "Performance analysis of satellite communication system under the shadowed-rician fading: A stochastic geometry approach," *IEEE Trans. Commun.*, vol. 70, no. 4, pp. 2707–2721, Apr. 2022.

[112] C.-S. Choi, "Modeling and analysis of downlink communications in a heterogeneous LEO satellite network," *IEEE Trans. Wireless Commun.*, pp. 1–1, Jan. 2024.

[113] M. Afshang and H. S. Dhillon, "Fundamentals of modeling finite wireless networks using Binomial point process," *IEEE Trans. Wireless Commun.*, vol. 16, no. 5, pp. 3355–3370, May 2017.

[114] ——, "k-coverage probability in a finite wireless network," in *Proc. IEEE WCNC*, 2017, pp. 1–6.

[115] X. Shi and N. Deng, "Coverage probability of UAV-enabled millimeter wave communications in finite areas," in *Proc. IEEE WCNC*, 2021, pp. 1–6.

[116] B. Al Homssi, A. Al-Hourani, K. Wang, P. Conder, S. Kandeepan, J. Choi, B. Allen, and B. Moores, "Next generation mega satellite networks for access equality: Opportunities, challenges, and performance," *IEEE Commun. Maga.*, vol. 60, no. 4, pp. 18–24, Apr. 2022.

[117] N. Senadhira, S. Durrani, X. Zhou, N. Yang, and M. Ding, "Uplink NOMA for cellular-connected UAV: Impact of UAV trajectories and altitude," *IEEE Trans. Commun.*, vol. 68, no. 8, pp. 5242–5258, Aug. 2020.

[118] N. Senadhira, S. Durrani, X. Zhou, N. Yang, and M. Ding, "Impact of UAV trajectory on NOMA-assisted cellular-connected UAV networks," in *Proc. IEEE ICC*, Jun. 2020.

[119] N. Senadhira, S. A. Alvi, N. Yang, X. Zhou, and S. Durrani, "Adaptive multiuser access for UAV-assisted IoT monitoring networks under bursty traffic," in *Proc. ICC Workshops*, 2023, pp. 1075–1081.

[120] N. Senadhira, S. Durrani, S. Alvi, N. Yang, and X. Zhou, "UAV-assisted IoT monitoring network: Adaptive multiuser access for low-latency and high-reliability under bursty traffic," *(submitted to) IEEE Trans. Commun.*, May 2024. [Online]. Available: https://arxiv.org/abs/2304.12684

[121] N. Senadhira, S. Durrani, J. Guo, N. Yang, and X. Zhou, "Design and performance analysis of UAV-assisted maritime-LEO satellite communication networks," *(submitted to) IEEE Open J. Commun. Soc.*, Oct. 2024.

[122] 3GPP, "3GPP TS 38.211: NR; physical channels and modulation (Release 15)," 2019.

[123] C. Kosta, B. Hunt, A. U. Quddus, and R. Tafazolli, "On interference avoidance through inter-cell interference coordination (ICIC) based on OFDMA mobile systems," *IEEE Commun. Surveys Tuts.*, vol. 15, no. 3, pp. 973–995, Third 2013.

[124] A. S. Hamza, S. S. Khalifa, H. S. Hamza, and K. Elsayed, "A survey on inter-cell interference coordination techniques in OFDMA-based cellular networks," *IEEE Commun. Surveys Tuts.*, vol. 15, no. 4, pp. 1642–1670, Fourth 2013.

[125] A. A. Khuwaja, Y. Chen, N. Zhao, M. Alouini, and P. Dobbins, "A survey of channel modeling for UAV communications," *IEEE Commun. Surveys Tuts.*, vol. 20, no. 4, pp. 2804–2821, Jul. 2018.

[126] X. Zhou, S. Durrani, J. Guo, and H. Yanikomeroglu, "Underlay drone cell for temporary events: Impact of drone height and aerial channel environments," *IEEE Internet Things J.*, vol. 6, no. 2, pp. 1704–1718, Apr. 2019.

[127] H. ElSawy and E. Hossain, "On stochastic geometry modeling of cellular uplink transmission with truncated channel inversion power control," *IEEE Trans. Wireless Commun.*, vol. 13, no. 8, pp. 4454–4469, Aug. 2014.

[128] H. Tabassum, E. Hossain, and J. Hossain, "Modeling and analysis of uplink non-orthogonal multiple access in large-scale cellular networks using Poisson cluster processes," *IEEE Trans. Commun.*, vol. 65, no. 8, pp. 3555–3570, Aug. 2017.

[129] M. Salehi, H. Tabassum, and E. Hossain, "Accuracy of distance-based ranking of users in the analysis of NOMA systems," *IEEE Trans. Communications*, vol. 67, no. 7, pp. 5069–5083, Oct. 2019.

[130] J. Wang, B. Xia, K. Xiao, Y. Gao, and S. Ma, "Outage performance analysis for wireless non-orthogonal multiple access systems," *IEEE Access*, vol. 6, pp. 3611–3618, Jan. 2018.

[131] H. Sun, B. Xie, R. Q. Hu, and G. Wu, "Non-orthogonal multiple access with SIC error propagation in downlink wireless MIMO networks," in *Proc. VTC-Fall*, Sep. 2016.

[132] B. Xia, J. Wang, K. Xiao, Y. Gao, Y. Yao, and S. Ma, "Outage performance analysis for the advanced SIC receiver in wireless NOMA systems," *IEEE Trans. Veh. Technol.*, vol. 67, no. 7, pp. 6711–6715, Jul. 2018.

[133] G. Yang, X. Lin, Y. Li, H. Cui, M. Xu, D. Wu, H. Ryden, and S. B. Redhwan, "A telecom perspective on the internet of drones: From LTE-Advanced to 5G," *CoRR*, vol. abs/1803.11048, Mar. 2018. [Online]. Available: http://arxiv.org/abs/1803.11048

[134] ITU, "Recommendation p.1410-5: Propagation data and prediction methods required for the design of terrestrial broadband radio access systems operating in a frequency range from 3 to 60 GHz," *Tech, Rep*, Feb. 2012.

[135] N. Cherif, M. Alzenad, H. Yanikomeroglu, and A. Yongacoglu, "Downlink Coverage and Rate Analysis of an Aerial User in Integrated Aerial and Terrestrial Networks," *arXiv:1905.11934*, May 2019.

[136] J. Holis and P. Pechac, "Elevation dependent shadowing model for mobile communications via high altitude platforms in built-up areas," *IEEE Trans. Antennas Propag*, vol. 56, no. 4, pp. 1078–1084, Apr. 2008.

[137] Y. Zeng and R. Zhang, "Energy-efficient UAV communication with trajectory optimization," *IEEE Trans. Wirel Commun.*, vol. 16, no. 6, pp. 3747–3760, Jun. 2017.

[138] Q. Wu, Y. Zeng, and R. Zhang, "Joint trajectory and communication design for multi-UAV enabled wireless networks," *IEEE Trans. Wirel. Commun.*, vol. 17, no. 3, pp. 2109–2121, Mar. 2018.

[139] Y. Zeng, J. Xu, and R. Zhang, "Energy minimization for wireless communication with rotary-wing UAV," *IEEE Transs Wireless Commun.*, vol. 18, no. 4, pp. 2329–2345, Apr. 2019.

[140] M. Haenggi, *Stochastic geometry for wireless networks.* Cambridge Univ. Press, 2012.

[141] D. López-Pérez, M. Ding, H. Li, L. G. Giordano, G. Geraci, A. Garcia-Rodriguez, Z. Lin, and M. Hassan, "On the downlink performance of UAV communications in dense cellular networks," in *Proc. IEEE GLOBECOM*, 2018, pp. 1–7.

[142] A. M. Hayajneh, S. A. R. Zaidi, D. C. McLernon, and M. Ghogho, "Drone empowered small cellular disaster recovery networks for resilient smart cities," in *Proc. IEEE SECON Workshops*, Jun. 2016, pp. 1–6.

[143] R. Arshad, L. Lampe, H. ElSawy, and M. J. Hossain, "Integrating UAVs into existing wireless networks: A stochastic geometry approach," in *Proc. IEEE GLOBECOM Wkshps*, 2018, pp. 1–6.

[144] M. Banagar and H. S. Dhillon, "3GPP-inspired stochastic geometry-based mobility model for a drone cellular network," in *Proc. IEEE GLOBECOM*, 2019, pp. 1–6.

[145] M. M. Azari, F. Rosas, A. Chiumento, and S. Pollin, "Coexistence of terrestrial and aerial users in cellular networks," in *Proc. IEEE Globecom Workshops*, Dec. 2017, pp. 1–6.

[146] B. Wang, K. Wang, Z. Lu, T. Xie, and J. Quan, "Comparison study of non-orthogonal multiple access schemes for 5G," in *Proc. IEEE BMSB*, 2015, pp. 1–5.

[147] W. B. Ameur, P. Mary, M. Dumay, J.-F. Hélard, and J. Schwoerer, "Power allocation for BER minimization in an uplink MUSA scenario," in *Proc. IEEE VTC Spring*, 2020, pp. 1–5.

[148] O. O. Oyerinde, "Comparative study of overloaded and underloaded NOMA schemes with two multiuser detectors," in *Proc. IEEE WAC*, 2019, pp. 1–5.

[149] ZTE, "Receiver implementation for MUSA, R1-164270," 2016.

[150] Z. Yuan, Y. Hu, W. Li, and J. Dai, "Blind multi-user detection for autonomous grant-free high-overloading MA without reference signal," 2017.

[151] S. Boyd and L. Vandenberghe, *Convex optimization*. Cambridge University Press, 2004.

[152] H. Ren, C. Pan, K. Wang, W. Xu, M. Elkashlan, and A. Nallanathan, "Joint transmit power and placement optimization for URLLC-enabled UAV relay systems," *IEEE Trans. Veh. Technol.*, vol. 69, no. 7, pp. 8003–8007, Jul. 2020.

[153] C. She, C. Liu, T. Q. S. Quek, C. Yang, and Y. Li, "Ultra-reliable and low-latency communications in unmanned aerial vehicle communication systems," *IEEE Trans. Commun.*, vol. 67, no. 5, pp. 3768–3781, May 2019.

[154] 3GPP, "Study on enhanced LTE support for aerial vehicles (Release 15)," 2018.

[155] S. Enayati, H. Saeedi, H. Pishro-Nik, and H. Yanikomeroglu, "Moving aerial base station networks: A stochastic geometry analysis and design perspective," *IEEE Trans. Wireless Commun.*, vol. 18, no. 6, pp. 2977–2988, Jun. 2019.

[156] X. Shi and N. Deng, "Modeling and analysis of mmWave UAV swarm networks: A stochastic geometry approach," *IEEE Trans. Wireless Commun.*, vol. 21, no. 11, pp. 9447–9459, Apr. 2022.

[157] X. Li, W. Feng, J. Wang, Y. Chen, N. Ge, and C.-X. Wang, "Enabling 5G on the ocean: A hybrid satellite-UAV-terrestrial network solution," *IEEE Wireless Commun.*, vol. 27, no. 6, pp. 116–121, Dec. 2020.

[158] Y. Tian, G. Pan, M. A. Kishk, and M.-S. Alouini, "Stochastic analysis of cooperative satellite-UAV communications," *IEEE Transa. Wireless Commun.*, vol. 21, no. 6, pp. 3570–3586, Jun. 2022.

[159] W. Mei, Q. Wu, and R. Zhang, "Cellular-connected UAV: Uplink association, power control and interference coordination," *IEEE Trans. Wireless Commun.*, vol. 18, no. 11, pp. 5380–5393, Nov. 2019.

[160] W. Mei and R. Zhang, "UAV-sensing-assisted cellular interference coordination: A cognitive radio approach," *IEEE Wireless Commun. Lett.*, pp. 1–1, Jan. 2020.

[161] R. Amer, W. Saad, B. Galkin, and N. Marchetti, "Performance Analysis of Mobile Cellular-Connected Drones under Practical Antenna Configurations," *arXiv e-prints*, p. arXiv:2002.00294, Feb. 2020.

[162] V. V. Chetlur and H. S. Dhillon, "On the load distribution of vehicular users modeled by a Poisson line cox process," 2020.

[163] G. Ghatak, A. De Domenico, and M. Coupechoux, "Accurate characterization of dynamic cell load in noise-limited random cellular networks," in *Proc. IEEE VTC-Fall*, 2018, pp. 1–5.

[164] C. Saha, P. D. Mankar, and H. S. Dhillon, "Rate coverage of a cellular network with users distributed as Poisson cluster process," in *Proc. IEEE ACSSC*, 2020, pp. 1193–1199.